www.uhasselt.be

Universiteit Hasselt | Campus Diepenbeek
Agoralaan | Gebouw D | BE-3590 Diepenbeek | België
Tel.: +32(0)11 26 81 11

Hexagonal Boron Nitride Nanowalls: Physical Vapour Deposition, Structural and Optical Properties Boumédiène BENMOUSSA

DOCTORAATSPROEFSCHRIFT

2011 | Faculteit Wetenschappen

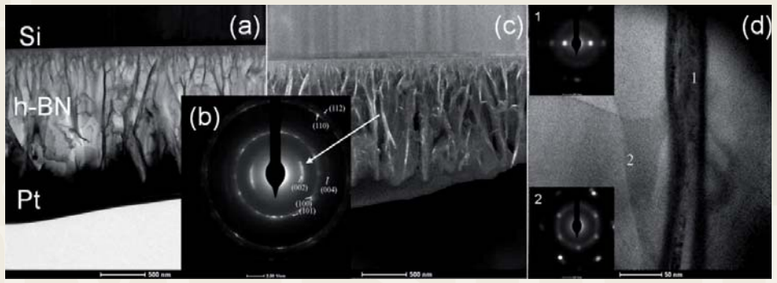

Hexagonal Boron Nitride Nanowalls: Physical Vapour Deposition, Structural and Optical Properties

Proefschrift voorgelegd tot het behalen van de graad van
Doctor in de Wetenschappen, Fysica, te verdedigen door:

Boumédiène BENMOUSSA

Promotor: prof. dr. Ken Haenen
Copromotoren: prof. dr. Hans-Gerd Boyen
prof. dr. Marc D'Olieslaeger

universiteit hasselt

DOCTORAATSPROEFSCHRIFT

2011 | Faculteit Wetenschappen

Hexagonal Boron Nitride Nanowalls: Physical Vapour Deposition, Structural and Optical Properties

Proefschrift voorgelegd tot het behalen van de graad van
Doctor in de Wetenschappen, Fysica, te verdedigen door:

Boumédiène BENMOUSSA

Promotor: prof. dr. Ken Haenen
Copromotoren: prof. dr. Hans-Gerd Boyen
prof. dr. Marc D'Olieslaeger

D/2011/2451/55

universiteit hasselt

Jury

Chairman	Prof. dr. Carlo Vanderzande	UHasselt, Belgium
Promoter	Prof. dr. Ken Haenen	UHasselt & IMEC vzw, Belgium
Co-promoter	Prof. dr. Hans-Gerd Boyen	UHasselt, Belgium
Co-promoter	Prof. dr. Marc D'Olieslaeger	UHasselt & IMEC vzw, Belgium
Jury members	Dr. Vincent Mortet	CNRS-LAAS, France
	Dr. Ali Soltani	CNRS-IEMN & Université Lille 1, France
	Dr. Erik Neyts	Universiteit Antwerpen, Belgium
	Prof. dr. Miloš Nesládek	UHasselt & IMEC vzw, Belgium
	Dr. Jan D'Haen	UHasselt & IMEC vzw, Belgium

Table of Contents

Acknowledgments

Accepting a PhD subject was an exciting challenge for many personal reasons. Like a colleague said, dealing with a PhD is like playing a lottery. The probability to earn is very small because the latter depends on various parameters. During these 4 years, these parameters in number of 3 have been some favorable elements to achieve this work. First, these are the quality of the PhD subject i.e. its role and impact within the scientific community. The means to achieve some paramount results which have enabled to write these few words for science. Finally, the lovely people around me who have conveyed a positive energy at work and out of work.

I would like to start the list of thanks with prof. dr. Ken Haenen, who is my supervisor. Thanks for choosing my CV from the bunch of applicants for this fellowship. I fully appreciate the independence and autonomy you granted me, this has given me the opportunity to grow and develop myself. Also, big thanks for taking the time to listen to my problems and for the fruitful suggestions and comments you made on my work.

To prof dr. Marc D'Olieslaeger, my co-promoter, I want to thank for supervising my work and for the opportunity to start my PhD under your initial supervising.

To prof. dr.Hans-Gerd Boyen, my co-promoter, I want to thanks for your relevant critical and your passions for everything related to physics and specially for physics laying on boron nitride material.

Thanks to dr. Vincent Mortet who gave me another vision of research, less idealized and more pragmatic. Your experience in material science and lithography processes were very helpful to forge for my own pragmatic approach to the science.

Thanks to dr. Ali Soltani who played a determining role in my research and provided me with his experience in material science and so on. The long hours in phone conversation and plenty of email sent, that made me to forget the importance of human contact to the benefit of remote working.

To the members of the jury, thanks for taking the time to come to Hasselt on December 14th. It must have been difficult to find a free day in your busy schedules.

Special thanks to dr. Jan D'Haen for providing me with the necessary surface and microstructural analyses presented in this thesis. My gratitude also for dr. Julien Barjon for the lovely CL analyses presented in this work.

This work was financially supported by the UHasselt BOF-project entitled "Growth and characterization of hexagonal boron nitride films by unbalanced RF magnetron sputtering", the Methusalem "NANO network", and the BELSPO (IAP-P6/42) project "Quantum Effects in Clusters and Nanowires". Dr. T. Taniguchi and K. Watanabe are warmly acknowledged for providing a high quality reference h-BN crystal. Thanks to C. Vilar for her technical assistance with the CL measurements. Dr. D. Troadec and J. Baccus are gratefully acknowledged for the respective FIB preparation and indispensable technical assistance.

I would not have managed to finish my PhD without the help of my IMO colleagues. Most of them already left our group, but some of them are still working here: Wim Deferme, Michael D., Stoffel J., Paulius P. and Yaso B. Also, the newcomers to our office: Pieter R., Wiebke J., Wim Dexters.

A special word also for colleagues from the other groups of IMO: Krishna Thalluri Venkata Visveswara alias Gopala, for coffee break and many fructuous conversations. Jean-Christophe B. for AFM measurements and your fighting spirit on each marathon. I have a lot of respect.

Lars G. for teaching to me how to use the contact angle technique and to get fluorescence data from h-BN/Si.

Mohammed Sharif M. for many fructuous scientific conversation on interest topic.

Many thanks for colleagues from chemistry department as Suleyman K. and Lydie.
For all the administrative work related to my PhD. I could always rely on the help of our institute secretaries Relinde H., Lea V. and Lisette L. and on the help of computer skillfully Erik T. Dank u wel!
Thanks to Bart R., Christel W. and Hilde P. for supplement me with all the necessary analyses and requests I had in the lab on a daily basis.

Also many thanks to my best friends, for their assistance and support: Safinne M., Rachid B., Mohamed K. and Michel T.

Finally, I convey to my family the greatest “Merci”, my Mother, brothers and sisters, brothers-in-law, sisters-in-law, nieces and nephews for their efficient support. You are a motor to my determination. Many kisses to you!!

Special thanks to my brother dr. Ali BenMoussa, who gave me a lot of advice, and he trusts me to achieve this “mission”.

Dank je wel!!
Thanks a lot!!
Merci beaucoup!!
شكرا جزيلا !!

Diden

In memory of my Father!! نسأل الله لك الرحمة

List of Acronyms and Abbreviations

A	a-BN	Amorphous boron nitride
	Ar	argon
	AFM	Atomic force microscopy
B	BN	boron nitride
C	CA	Contact angle measurement
	c-BN	Cubic boron nitride
	CFM	Confocal force microscopy
	CL	cathodoluminescence
	CNW(s)	carbon nanowall(s)
	CVD	Chemical Vapor Deposition
E	EDS	Electron deflection x-ray spectroscopy
F	FESEM	Field emission scanning electron microscopy
	FTIR	Fourier transform infrared
	FWHM	Full Width at Half Maximum
H	h-BN	Hexagonal boron nitride (polycrystalline)
	h-BNNWs	Hexagonal boron nitride nanowalls
	h-BN(NWs)	Hexagonal boron nitride (polycrystalline) + Hexagonal boron nitride nanowalls
	H_2	dihydrogen
	$\%H_2$	Percentage of dihydrogen gas added to the Ar/N_2 plasma
I	IR	Infrared
M	MS	Magnetron sputtering
	MS-PVD	Magnetron sputtering-Physical Vapor Deposition
N	N_2	Nitrogen
	$\%N_2$	Percentage of nitrogen gas within Argon discharge plasma
P	PECVD	Plasma Enhanced Chemical Vapor

		Deposition
	PVD	Physical Vapor Deposition
	PIRR	Polarized infrared in reflection mode
	PIRTo	Oblique polarized infrared in transmission mode
R	r-BN	Rhombohedric boron nitride
	RBS	Rutherford Backscattering
	RF	Radio frequency
	RF-MS	Radio frequency-Magnetron sputtering
S	SEM	Scanning electron microscopy
	Si (100)	Silicon substrate (100)
	SQUID	Superconducting Quantum Interference Device
T	t-BN	Turbostratic- boron nitride
	TEM	Transmission electron microscopy
U	UV	Ultraviolet
	UV-Vis-NIR	Ultraviolet-Visible-Near Infrared
W	w-BN	Wurtzite- boron nitride
X	XPS	X-ray photoemission spectroscopy

Abstract

Since the discovery of graphene[1], the two-dimensional (2D) honeycomb crystal receives a renewed attention with a particular focus on nanostructures due to its exceptional properties and potential application in materials science. Besides single layer graphene, a nanowall is described as a 2D nanostructure which typically has a platelet-like structure that rises upwards from the surface in a vertically uniform direction.

Like carbon nanomaterials, boron nitride (BN) has attracted overwhelming attention owing to its structural similarity. Such as carbon, BN exists in sp^2-bonded form, i.e. hexagonal BN (h-BN) or in sp^3-bonded type, namely cubic BN (c-BN). A layered h-BN structure has excellent physical properties analogous to graphite, being in-plane mechanically strong and showing high chemical and thermal stability[2-4]. Recently, h-BN has shown to be an alternative substrate for graphene deposition[5].

The objectives of this thesis are strengthening the efforts that are going on to investigate high quality h-BN thin film deposition for various applications and in particular to the growth of 2D h-BN nanowalls. In this work, the use of physical vapor deposition techniques is proposed. Although there are few reports on the synthesis of h-BN films by the CVD technique, this work is based on the easy to handle, scalable and cost effective reactive radio-frequency magnetron sputtering.

The first chapter provides primarily background information on the BN material. This chapter describes the synthesis of different BN allotropes with a focus on h-BN as a thin film and the mechanism responsible for its formation. Among several growth techniques for h-BN thin films, I will introduce the unbalanced magnetron sputtering as a physical vapor deposition technique used during these four years of investigations at the Institute for Materials Research (IMO), Hasselt University. I will discuss the influence of the deposition parameters.

In chapter 2, a homemade RF unbalanced magnetron sputtering system will be completely described (MS-PVD). Different characterization techniques will be presented in two distinct sections. The spectroscopy techniques and the microscopic imaging that enable to identify the h-BN features, will be further detailed throughout this chapter.

In chapter 3, optimized parameters to control the MS-PVD setup will be briefly introduced. I will focus on technical enhancements and deposition conditions for the growth of good quality, reproducible and homogenous h-BN films. In this chapter I will introduce as well the deposition parameters responsible for a specific structure identified as 2D h-BN "nanowalls"(h-BN NWs).

Chapter 4 deals with the optical properties of h-BN (NWs) films. I will present different methods based on infrared techniques and micro-Raman spectroscopy to assess the structural properties of these nanowalls films. The measurements using the UV-Vis-NIR spectrophotometer will allow me to evaluate the quality of my h-BN layers. The cathodoluminescence technique will be used as well in order to highlight the nature of the h-BN (NWs) excitons. Two different optical techniques will be used for measurements to confirm the porosity of h-BN (NWs) films.

Chapter 5 will describe some possible future applications of the h-BN (NWs) films. The super-repellent behavior of the h-BN (NWs) will be investigated using a contact angle measuring device. I propose a method of fabrication and characterization of h-BN (NWs) flakes in order to use them as a template for graphene and DNA-attachment. An experimental approach assessing the magnetic properties of the h-BN (NWs) will be briefly discussed.

Finally, I will end with a short overview of the main conclusions and achievements that are presented in this thesis. Some guidelines are given for the further improvements and suggestions are made for future research in this promising field.

References

1. K. S. Novoselov, A. K. Geim, S. V. Morozov, D. Jiang, Y. Zhang, S. V. Dubonos, I.V. Grigorieva, A. Firsov, *Science* **2004**, *306*, 666.

2. T. Ouyang, Y. Chen, Y. Xie, K. Yang, Zh. Bao, J. Zhong, *Nanotechnology* **2010**, *21*, 245701.

3. T. K. Pauli, P. Bhattacharya, D. N. Bose *Appl. Phys. Lett.* **1990**, *56,* 2648.

4. C. Li, Y. Bando, C. Y. Zhi, Y. Huang, D. Golberg, *Nanotechnology* **2009**, *20*, 385707.

5. C. R. Dean, A. F. Young, I. Meric, C. Lee, L. Wang, S. Sorgenfrei, K. Watanabe, T. Taniguchi, P. Kim, K. L. Shepard, J. Hone, *Nature Nanotech*. **2010**, *5*, 722.

Nederlandse samenvatting

Sinds de Nobelprijs Natuurkunde in 2010 werd toegekend voor experimenten op grafeen[1], ontvangen alle tweedimensionale (2D) honingraat-kristal nu hernieuwde aandacht dankzij zijn uitzonderlijke eigenschappen en mogelijke toepassingen in de materiaalkunde. De focus ligt nu op nanostructuren, zoals zogenaamde “nanowalls” Een “nanowall” is een 2D-nanostructuur met een plaatachtige structuur die opstijgt uit het oppervlak in een verticale uniforme richting.

Naast koolstofnanomaterialen, trok ook boornitride (BN) de aandacht vanwege zijn structurele gelijkenis. Net zoals koolstof, bestaat BN in sp^2-gebonden vorm; dat wil zeggen hexagonaal BN (h-BN), of in sp^3-gebonden vorm, namelijk kubisch BN (c-BN). Een gelaagde h-BN-structuur heeft uitstekende fysische eigenschappen, analoog aan grafiet, dat in het vlak, mechanisch sterk is, en een hoge chemische en thermische stabiliteit heeft [2-4]. Onlangs werd aangetoond dat h-BN een alternatief substraat is voor grafeendepositie[5]. In dit werk wordt het gebruik van de fysische dampdepositietechniek (PVD) voorgesteld. Hoewel er een aantal rapporten zijn over de synthese van h-BN films met behulp van de chemische dampdepositietechniek (CVD), is dit werk gebaseerd op de gemakkelijk te hanteren, schaalbare en kosteneffectieve reactieve radiofrequentie-magnetron sputtertechniek.

Het eerste hoofdstuk geeft vooral achtergrondinformatie over het BN materiaal. Dit hoofdstuk beschrijft de synthese van verschillende BN allotropen, met de focus op h-BN dunne film, en het mechanisme verantwoordelijk voor de vorming ervan. Tussen de verschillende groeitechnieken voor h-BN dunne films, zal ik de ongebalanceerde magnetron sputtertechniek introduceren als fysische dampdepositietechniek, die ik gebruikt heb tijdens de vier jaren van onderzoek aan het Instituut voor Materiaalonderzoek (IMO), Universiteit Hasselt.

In hoofdstuk 2 wordt een zelfgemaakt RF ongebalanceerde magnetron sputter-systeem volledig beschreven (MS-PVD). Films afgezet op Si (100) worden op een kwalitatieve manier onderzocht met elektronen afbuiging X-stralen spectroscopie (EDS) om C en O verontreinigingen te onderzoeken, en ook, op een kwantitatieve manier met Rutherford terugverstrooiing spectroscopie (RBS) om de structuur en stoichiometrie van de h-BN films te bevestigen.

In hoofdstuk 3 worden de geoptimaliseerde parameters om de MS-PVD-setup te regelen, kort voorgesteld. Ik zal me concentreren op technische verbeteringen en depositie-omstandigheden voor de groei van goede kwaliteit, reproduceerbare en homogene h-BN films. Ik zal H_2 als een reactief gas in het N_2/Ar mengsel introduceren tijdens het RF-sputteren, wat leidt tot 2D h-BN "nanowall" (h-BN NWS) lagen met een verminderde hoeveelheid zuurstof en koolstof onzuiverheden, onafhankelijk van het substraatmateriaal. Terwijl fluor wordt uitgesloten als een cruciaal onderdeel in de vorming van koolstof nanowalls, is de rol van waterstof noodzakelijk voor de goedgecontroleerde groei van deze 2D/3D structuren. Een optimum van 5% H_2 leidt tot stochiometrische h-BN nanowalls onafhankelijk van de depositietemperatuur. TEM beelden genomen op dwarsdoorsnedes hebben de typische h-BN plaatjesstructuur aangetoond met een dikte minder dan 50 nm, waarbij dee (002) vlakken tilt meer dan maximaal 20 ° ten opzichte van de normale richting van het gebruikte substraatmateriaal. Meer experimenten moet worden gedaan om deze resultaten te bevestigen.

Hoofdstuk 4 gaat over de optische eigenschappen van de h-BN (NWS) films. Het bewijs van de hexagonale fase en van de BN lagen werd opgemeten met Fourier Transform infrarood (FTIR) en micro-Raman spectroscopie. Gepolariseerd infrarood reflectie spectra (PIRR) werden voor het eerst op h-BN nanowalls opgemeten. De bandkloof voor films gegroeid met 5% H_2 wordt gemeten met behulp van de UV-Vis-NIR spectrofotometer en kathodoluminescentie (CL) techniek. De luminescente eigenschappen van h-BN nanowalls worden gedomineerd door een brede band luminescentie afkomstig van onzuiverheden in de buurt van 4 eV, die ook wordt waargenomen in bulk h-BN kristallen. Dit is mogelijk gerelateerd aan de C-en O onzuiverheden. De recombinatie van excitonen van h-BN nanowalls is in overeenstemming met de kenmerken van bulk h-BN in de aanwezigheid van structurele gebreken, korrelgrenzen of onzuiverheden. Door gebruik te maken van nano CL, werden ook meerdere luminescentie pieken waargenomen. Mogelijks kunnen deze te wijten zijn aan excitonen gevangen op structurele gebreken in de h-BN film.

Tot slot worden enkele richtlijnen gegeven voor de verdere verbeteringen en suggesties gedaan voor toekomstig onderzoek in dit veelbelovend gebied. Het super-waterafstotend gedrag van het/de h-BN (NWS) wordt onderzocht met behulp van contacthoekmetingen. Ik stel tevens een methode voor om h-BN (NWS) plaatjes te produceren die gebruikt kunnen worden als een substraat voor grafeendepositie of als DNA-aanhechtingssjabloon. Een experimentele benadering van de beoordeling van de magnetische eigenschappen van het/de h-BN (NWS) wordt verder kort besproken.

Chapter 1 Boron Nitride

The first chapter is dedicated to a general description of the boron nitride (BN), pointing out their specific properties, which makes it an appropriate material for a wide range of applications. This material is considered as a promising candidate for the fabrication of optoelectronic devices. After a quick overview of the classification of BN based material, hexagonal boron nitride (h-BN) structure and crystallinity will be discussed in more detail. Some applications of h-BN are listed, followed by the description and properties of h-BN nanowall structures (h-BNNWs). The following sections will describe the different techniques involved in producing semiconducting synthetic h-BN material. The similarities with 2D carbon nanomaterial (carbon nanowalls) discovered several years ago, will be the basis of the understanding of h-BN (NWs) such as the origins and mechanisms of growth.

1.1 Boron nitride

1.1.1 Classification: allotropes

Such as carbon, BN has many allotropes. It exists in the forms of sp^2-bonded hexagonal BN (h-BN) and rhombohedral (r-BN) or sp^3-bonded wurtzite (w-BN) and cubic BN (c-BN). Being a layered structure, h-BN has excellent physical properties analogous to graphite. Its properties are described in detail in the following section.

1.1.1.1 Hexagonal boron nitride (h-BN)

The hexagonal phase of BN has the crystalline ABAB plane stacking. The lattice structure of h-BN is formed by the stacking of B_3N_3 hexagons related to the c-axis orientation (0001) where each boron atom is bonded in-plane to three nitrogen atoms and reciprocally: The B planes are deduced from the A plane by a rotation of 60° (Figure 1- 1) and a movement along the [0001] direction perpendicular upon the A, B planes.

The h-BN (or alpha-BN) nominated as white graphite is a layered compound and highly anisotropic due to its crystal structure like graphite e.g. strong bonding in two dimensions (a-direction) and weak bonding in the third (c-direction). Whereas graphite is a semi-metal, h-BN is an electrical insulator due to the lack of free electrons in wide band gap material. The plane structure (in-plane) is sp^2 type what ensures the strong bonding between each atom from the same plane (covalent bond). On the other side, between two planes (out-of-plane), the bonding remains van der Waals type i.e. very weak bonds, what explains the very high compressibility and high lubricity of the structures. Moreover, π-electrons are localized around nitrogen (N) giving the partial nature of ionicity from B-N bonding, unlike graphite where the π-electrons are delocalized over its four neighbor atoms. Wherefore the latter is an electrical conductor and BN is not. Depending on the deposition condition, it should be notify that instead of h-BN, a mixture of amorphous phase with a turbostratic structure is deposited. The latter (t-BN) is characterized by a layer structure similar to h-BN with a disorder i.e. the hexagonal basal planes have slipped sideways relative to each other along the c-axis.

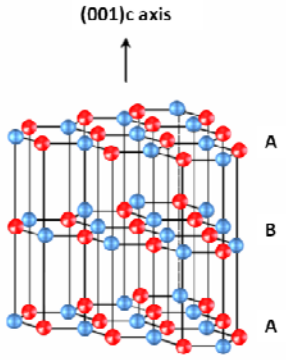

Figure 1- 1: hexagonal boron nitride (h-BN) crystalline structure

The thermal conductivity of h-BN is influenced by lattice vibrations: The thermal conductivity[1] in the plane of the atomic layers (a-direction) is an order of magnitude higher than perpendicular to the layers (c-direction) due to the difference in distance between nearest neighbors atoms.

BN has not been found in nature and is therefore produced synthetically. h-BN is obtained on industrial scales by the reaction of boron trioxide (B_2O_3) or boric acid ($B(OH)_3$) with ammonia (NH_3) or urea ($CO(NH_2)_2$) in nitrogen atmosphere[2]:

- H-BN can be fabricated inexpensively by hot-pressing with subsequent machining. The parts are made from BN powders adding boron oxide for better compressibility. Thermal conductivity of h-BN is dependent on the crystalline order, and is significantly increased by annealing under pressure to produce highly oriented hot pressed BN.

- Thin films of boron nitride can be obtained by chemical vapor deposition (CVD) from boron trichloride and nitrogen precursors[3]. Combustion of boron powder in nitrogen plasma at 5500 °C yields ultrafine BN used for lubricants and toners[4] (pyrolitic BN).

1.1.1.2 Rhombohedral boron nitride (r-BN)

Despite significant differences between crystalline structures, the electronic structure of r-BN[5] is similar with h-BN but less studied.

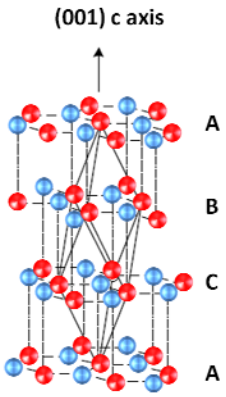

Figure 1- 2: rhombohedral boron nitride (r-BN) crystalline structure

r-BN is formed by B_3N_3 hexagons planes, such as h-BN, with a stacking along the c-axis as ABCABC where the translation vectors (a, b, c) of each planes (A→B and B→C) are movements of (1,1) along a,b axis, 1/3 along the c-axis and a rotation of 60° (Figure 1- 2). This structure is obtained as small crystals under high pressure high temperature (HPHT), or as thin films with ion beam assisted PVD techniques.

1.1.1.3 Wurtzite boron nitride (w-BN)

The wurtzite structure (w-BN or γ-BN) could be described as a stacking of B and N tetrahedrons where the bonding of each atom is sp^3-hybridization type. It contains 6 atoms of each type (Figure 1- 3).It results from deformations of the hexagonal lattice with two interpenetrating hexagonal close packed (HCP) sub lattices. The distance between each twisted hexagon planes could be reduced by compression under high pressure, leading to the switching of the hybridization from sp^2 to sp^3. At ambient conditions, the synthesized w-BN[6,7] is difficult to obtain because these wurtzite structures are thermodynamically metastable.

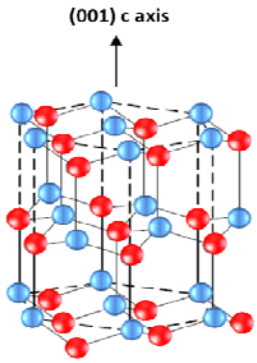

Figure 1- 3: wurtzite boron nitride (w-BN) crystalline structure

1.1.1.4 Cubic boron nitride (c-BN)

The zinc blende sp^3 synthesized structure (c-BN or β-BN) has a cubic unit cell. The position of the atoms within the unit cell is identical to the zinc blende (ZnS) crystal structure. It results from two interpenetrating face centered cubic (FCC) sublattices, offset by one quarter of the distance along a body diagonal. Each boron atom is positioned at the centre of a tetrahedron, with its four nearest neighbors (N atoms) defining the four corners of the tetrahedron, and vice versa (Figure 1- 4).

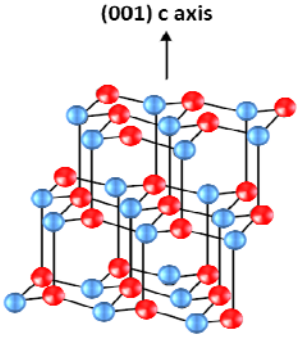

Figure 1- 4: zinc-blend or cubic boron nitride (c-BN) crystalline structure

To summarize, these four allotropes transform each other using the Pressure-Temperature (P-T) phase diagram (see Figure 1- 5). The polymorphic transformations of h-BN ->w-BN and r-BN ->c-BN[6] can proceed via a continuum structural distortion[7] (diffusion less) at room temperature and high pressure. However the phase formed at high pressure and low temperature leads also to the same result i.e. (h-BN→ c-BN) and (r-BN → w-BN) [7].

1.1.2 Crystallographic structure and properties

BN is a binary compound formed by the first elements of the column III_B and V_B from the periodic table, framing carbon. BN is isoelectronic with the carbon atom i.e. B^- and N^+ are two ions having the same number of electrons like carbon, and BN is the most lightweight compound of III-V group. BN, with the same electronic configurations, tends to have similar chemical and physical properties as carbon c-BN and diamond have similar crystal structure, lattice constant and physical properties such as extreme hardness, wide energy bandgaps and high thermal conductivities far away from silicon carbide (SiC) and even more far from silicon (Si), zinc sulfide (ZnS) and indium phosphide (InP). h-BN and graphite have similar crystal structure, lattice constant and physical properties such as thermal conductivity and mechanical strength (see Table 1- 1 and Table 1-2).Briefly, B-N and B=N bonds have chemical properties similar and sometimes better than carbon structures, i.e. C-C and C=C respectively. However, there are significant differences in chemical bonding: BN has mixed covalent-ionic bonding, while bonding in carbon is completely covalent i.e. small bonding length and very low ionicity. Due to its lower hardness, the ionicity of BN is higher than carbon (see Table 1-2). Both types of BN (h-(r-) and c-(w-)) are more resistant to oxidation than their carbon analogues due to the formation

of the nonvolatile boron oxide. c-BN and h-BN thin film growth is not yet well controlled such as graphite and diamond respectively. Graphite is thermodynamically stable under ambient condition of temperature and pressure, whereas diamond is metastable. This behavior leads to the same conclusion concerning BN phases. Many applications using different allotropes of BN have motivated various researches in order to synthesize them.

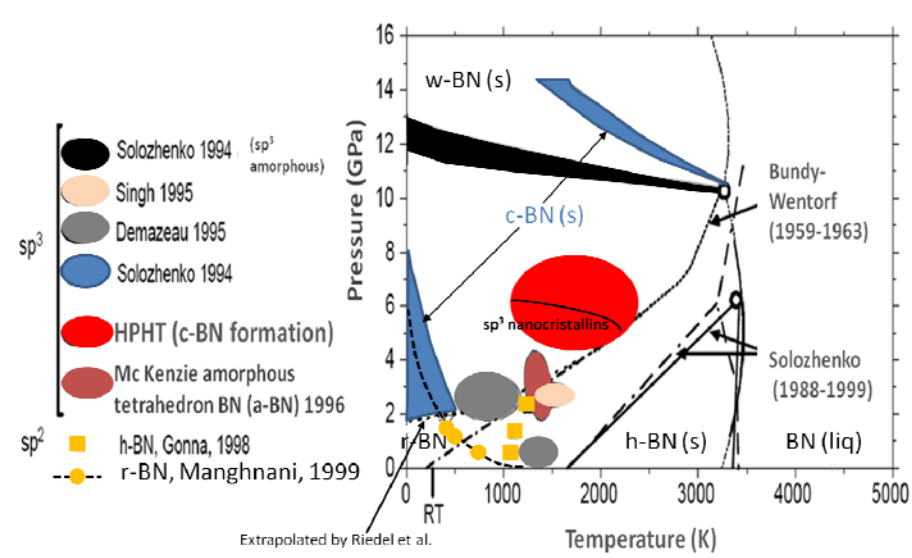

Figure 1- 5: Bundy-Wentorf's phase diagram for BN[1] and experimental h-BN↔c-BN boundaries.

As shown in Figure 1- 5, cubic phases of boron nitride, like diamond are generally produced at high temperatures (T>1800K) and high pressure (p>4GPa). On the other side, h-BN and graphite are produced at high temperature but at lower pressure (p≤100 kPa).

According to the phase diagram of BN, the hexagonal phase is thermodynamically stable at ambient temperature and pressure, whereas c-BN is stable only within the high pressure zone (Bendy-Wentorf line). In this zone, c-BN would be spontaneously formed. However, Solozhenko et al[8] have questioned this representation after new experiments and suggest that the equilibrium curve should be shifted into lower pressures, leading in this case to the stable phase of c-BN at ambient temperature and pressure.

In summary, like carbon, BN has two hybridization states which could be classified into two sub-categories in accordance with hardness properties[9]:

- Soft phase of BN with low density corresponds to the sp^2 bonding. h-BN like graphite, together with r-BN, belong to this category. One can note the presence of turbostratic BN (t-BN) and amorphous boron nitride (a-BN) depending on the crystal defects.

- Hard phase of BN formed by sp^3 bonding constitutes the dense structure of BN. These structures could be described as a stacking of tetrahedrons whose bonds between each atom are sp^3 type. w-BN described sparsely in literature, together with zinc-blend or c-BN, which is known to be similar to zinc blende (ZnS), falls into this category.

		a (nm)	c (nm)	The point group	Atomic positions
Soft phases	h-BN	0.2504	0.6789	$P6_3/mmc$	B : (0,0,0), (2/3,1/3,1/2) N : (2/3,1/3,0), (0,0,1/2)
	r-BN	0.2507	1	R3m	B : (0,0,0),(2/3,1/3,1/3),(1/2,2/3,2/3) N : (2/3,1/3,0), (1/3,2/3,1/3), (0,0,2/3)
Hard phases	w-BN	0.2556	0.4175	$P6_3mc$	B : (0,0,0), (1/3,2/3,1/2) N : (0,0,3/8),(1/3,2/3,7/8)
	c-BN	0.3615	0.3605	F3m	B:(0,0,0),(1/2,1/2,0),(0,1/2,1/2),(1/2,0,1/2) N:(1/4,1/4,1/4),(3/4,3/4,1/4),(1/4,3/4,3/4), (3/4,1/4,3/4)
C based	graphite	0.246	0.6709	$P6_3/mmc$	C: (1/3,2/3,1/4),(2/3,1/3,3/4)
	diamond	0.3567	0.3567	Fd3m	C: (0,0,0),(1/4,1/4,1/4)

Table 1- 1: lattice parameter of hexagonal, rhombohedral, wurtzite and cubic boron nitride[9, 10]. Comparison is made with graphite and diamond.

1.1.3 Main properties

The most important boron nitride properties are summarized in a Table 1-2, together with a comparison with graphite, also with diamond.

		a- BN	h -BN	w -BN	c -BN	graphite	Diamond
Crystalline structure		amorphous	hexagonal	wurtzite	cubic		
Physical-chemical properties							
Lattice parameter a (Å) / c (Å)		-	2.494/6.66	2.536/4.199	3.615	2.461/6.709	3.567
Inter-atomic distance (Å)		-	a=1.446 c=3.33	-	1.57	1.42	1.54
Density (g/cm^3)		2.03	2.271	3.485	3.45	2.09-2.23	3.52
Ionicity		-	0.25	-	0.25		0
Chemical stability		-	Inertness	-	Inertness	Inertness	Inertness
Optical properties							
Transparency		opaque	UV-Vis-IR	-	UV-Vis-IR	opaque	-
Refractive index (589.3 nm)		1.7	2.13/1.65	-	2-2.12	1.93-2.07	2.4
Band gap	**Transition**	-	Direct/Ind.	Indirect	Indirect	-	Indirect
	Gap (eV)	5.05	3.2-5.98	4.5-5.5	6.1-6.6		5.45-5.5
Mechanical properties							
Acoustic velocity (x10^3 m.s^{-1})		-	~ 3-6	-	~ 4-15	-	~ 11-18
Hardness (kg.mm^{-2})		-	1000	-	4000-5000	2800	9000
Young modulus (GPa)		-	34$\parallel$; 87$^{\perp}$	-	712	4.8	1140
Thermal properties ($\parallel$ and $^{\perp}$ to pressing direction)							
Thermal Conductivity (W.cm^{-1}.K^{-1})		0.03	0.625$\parallel$; 0.017 $^{\perp}$	0.6$^{\perp}$	7.4	0.24	6-20
Thermal expansion (x10^{-6} /°C)		-	-2.7$\parallel$; 38$^{\perp}$	2.7	1.2-4.8	1.2-8.2	0.8
Melting point (K)		-	2800	-	> 2975	3820	3800
Stability to oxidation (°C)		-	> 1000		1200	-	600
Graphitization (°C)		-			≥ 1500	-	1400
Electrical properties							
Resistivity at 20°C (Ω.cm)		10^5-10^6	10^{17}	-	10^{10}	10^{-6}	10^{16}
Dielectric constant (at 1MHz)		4-8	2.7-7.7	-	5.6-7	10-15	-
Breakdown voltage (x10^6 V.cm^{-1})		8-15	5-7	-	1	-	-
SC dopants	**n**	-	-	-	Si,S,K,C	-	-
	p				Be,Mg	-	P,B

$\parallel$ to pressing direction= direction "a"; $^{\perp}$ to pressing direction=direction "c"

Table 1-2: Summary of the important physical boron nitride (BN) properties[9].

1.1.3.1 Potential and effective applications of h-BN

The physical-chemical properties of h-BN in terms of mechanical, thermal, optical and electrical behavior show that this material appears as an interesting candidate for many industrial applications.

Being a layered structure, h-BN has many excellent physical properties analogous to graphite. It shows high chemical and thermal stability[11-14]. It has a wide band gap of up to 5.9 eV[15], which has important applications for its possible use as a deep-ultraviolet-light emitter and detector[16,17]. Because of the structural similarity to graphite, h-BN has even recently shown to be a competitive and alternative substrate candidate for graphene devices[18]. Whereas many authors have reported the synthesis of h-BN thin films by chemical vapor deposition (CVD), using various source gases such as B_2H_6[19], BCl_3[20], BBr_3[21], and BH_3NH $(CH_3)_2$[22], the use of physical vapor deposition (PVD) techniques is less studied.

H-BN known as a soft colorless ceramic , and an electrical insulator with low density. Its high thermal conductivity, high chemical inertness, high melting point (up to 1000 °C in air, 1400 °C in vacuum, and 2800 °C in an inert atmosphere), low dielectric constant and high resistance to oxidation[10] belong to the main qualities of h-BN. Because of its excellent thermal and chemical stability, BN ceramics are traditionally used as parts of high-temperature equipment. For instance, any heating elements covered by h-BN avoid oxidization at temperatures lower than 1200°C. This ceramic with low mechanical strength has a two-dimensional crystal structure, giving it some high thermal lubricant applications like graphite[23]. It is a good lubricant at both low and high temperatures (up to 900 °C, even in an oxidizing atmosphere). Another important application concerns the micro fabrication technique as a mask for UV photolithography that could be used for chemical etching. It can also be used as a diffusion source of boron atoms to realize p-n junctions on n doped silicon. Some studies show the possibility to get cold emitting electrons cathodes by doping the material with carbon[24].

h-BN is known as a wide band gap III-V semiconductor, giving it a high insulator quality with a high resistivity ($10^{17}\Omega$.cm) at room temperature and around $10^{14}\Omega$.cm at 200°C. h-BN could be used as a grid insulator for metal-insulator-semiconductor field effect transistor (MISFET) applications[25]. Its large band gap allows development of photodetectors from deep-ultraviolet (DUV) to the far ultraviolet (FUV) regions. For this purpose, different semiconductors as silicium[26] (Si), gallium arsenide[27] (GaAs) or Indium phosphide[28] (InP) were used as substrate. H-BN thin films have been used in metal-insulator-metal (MIM) tunneling structures and for the realization of capacitances[29].

BN films are also used for the manufacturing of planar diode, protective layers and as insulator for power transformers[30]. One of the most important applications implies h-BN powders used as high thermal crucibles and evaporators in the semiconductor industry. H-BN is used for a lot of mercantile applications as a protective coating. Also, with its high thermal conductivity properties, it could be used as radiators in microelectronics devices.

H-BN is partially transparent to infrared and microwave radiation. Its properties allow to be used for the production of radar and infrared windows. It is used as material fitting pieces, binder for organic polymers or as resin. Such materials are suitable for construction of e.g. bearings and in steelmaking[31].

1.1.4 Aim of this investigation

The recent work of Watanabe et al.[16,32,33] has shown remarkable opto-electronic properties of pure h-BN single crystal deposited under high pressure and high temperature (HPHT) method. Consequently, h-BN became an overwhelming material.

In Figure 1- 6, intense UV luminescence is observed at 5.765 eV (215.0 nm). The shoulder structures around the energy of 4 eV (300 nm), which are probably assigned to vacancies or residual impurities such as oxygen and carbon 14, are 100 times smaller than the single peak in the UV region. The contrast between the weak defect-related band and the intense UV band near the band edge means that the h-BN sample has low defect density.

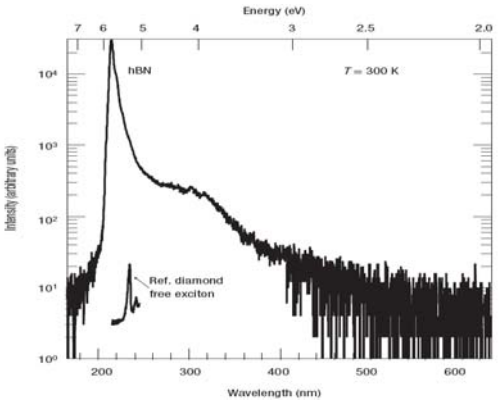

Figure 1- 6: Example of cathodoluminescence spectrum for h-BN at room temperature. Indirect free exciton luminescence of pure diamond is also shown as a reference[16].

This emission from h-BN pure crystals is 10^3 times stronger than an indirect-bandgap type IIa pure diamond material[34,35,36] which is used for optical device applications. The emission could be interpreted as a transfer of energy between Bloch waves having the same momentum near the conduction band minimum and valence band maximum.

This material is considered as a promising candidate for a wide range of advanced applications based on its luminescent properties (bandgap of 5.9eV).

To fulfill these potential applications, it is necessary to deposit BN thin films on a variety of substrates. The purpose of this thesis is to deposit h-BN thin film using a homemade PVD system to response to the exciting challenge.

1.2 Preparation of thin h-BN films

The preparation of thin BN films requires some deposition techniques. While the high pressure and high temperature (HPHT) technique produces high quality crystals, the technique itself is rather cumbersome, leading to small, irregular crystals that are difficult to handle due to their fragile nature. Since 1980's, the miniaturization of the technological devices requires thinner and thinner films (µm to nm range). In this way, the use of vapor phase techniques at low pressure made its apparition. The analogies between c-BN and diamond have inspired again a development of this new material. Taking into account the development of those techniques, many authors have reported the synthesis of thin h-BN films in the same way as c-BN by CVD technique using various source gasses. In order to clarify these studies, the other CVD technique are summarized in a Table 1- 4 (section 1.2.4), and to point out the growth of h-BN using physical vapor deposition (PVD) techniques, less studied and subsequently discussed.

1.2.1 Plasma enhanced chemical vapor deposition (PECVD)

During the growth of BN, CVD technique assisted by plasma (PECVD) supposes the decomposition or dissociation of inorganic compound as boron trifluoride (BF_3), nitrogen (N_2) and H_2 within a Micro-wave plasma source (MW).Using this (MW-PECVD) method (Figure 1- 7), Yu et al.[37] are the first authors to report the synthesis of vertically aligned h-BN sheets on silicon substrates.

This recent and unique reference concerning the growth mechanism of h-BN sheets (MW power=800 W, substrate temperature= 800 °C and chamber pressure= 6 kPa) is not clearly studied. However, the similitude with carbon nanowall[14,38,39,40] which gave its name to h-BN nanowalls (h-BNNWs) is the state of art. H-BNNWs have similar 2D nanostructures and typically have a wall-like structure in which the walls rise upwards from the surface of a substrate in a vertically uniform direction.

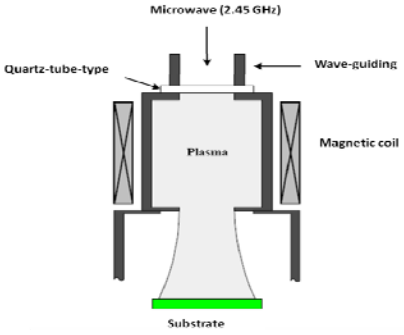

Figure 1- 7: Microwave reactor allowing the synthesis of h-BN nanowalls[37]

1.2.2 Physical vapor deposition (PVD)

Generally, PVD techniques can be divided into two main groups: evaporation and sputtering. In these two main groups there are many sub-divisions. In the evaporation group, thermal evaporation, arc evaporation, ion-beam and electron-beam evaporation can be found but will not be further discussed in this thesis. Some of them will be summarized in Table 1- 4 (section 1.2.4). Sputtering techniques which can be divided into diode sputtering and magnetron sputtering will be focused.

1.2.2.1 Plasma source

A plasma source, which in most laboratory conditions is a gas discharge, represents the physical and engineering basis of the plasma chemistry. For simplicity, an electric discharge can be viewed as two electrodes inserted into a chamber and connected to a power supply (Figure 1- 8a). The chamber can be filled with various gasses or evacuated (Figure 1- 8b). As the voltage applied across the two electrodes increases, the current suddenly increases sharply at a certain voltage required for a sufficiently intensive electron avalanche.

If the pressure is low, on the order of a few torrs, and the external circuit has a large resistance to prohibit a large current, a glow discharge develops. The glow discharge can be considered as major example of low pressure and non-thermal plasma source[41]. Keeping in mind that for instance, a non-thermal "corona" discharge occurs at high pressures (including atmospheric pressure) only in regions of sharply non-uniform electric fields and the arc discharge can be considered a major example of thermal plasma source.

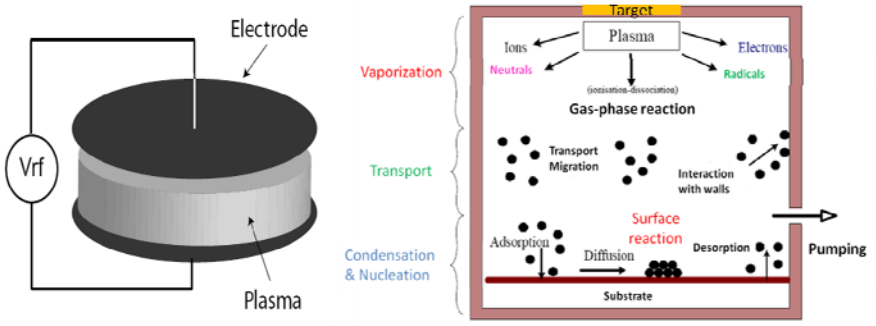

(a) *(b)*

Figure 1- 8: Overview of the PVD system (a) and the mechanism of deposition on the PVD chamber (b).

The thin films formation shown in Figure 1- 8b is split into 3 main processes as following:

1.2.2.2 Vaporization of the target material

During the vaporization process, interactions of active species, ions, neutrals, electrons, backscattering of atoms, x-ray emission and desorption of gas atoms occur from the target surface. Other processes shown in Figure 1- 9 illustrate the complex phenomenon of sputtering.

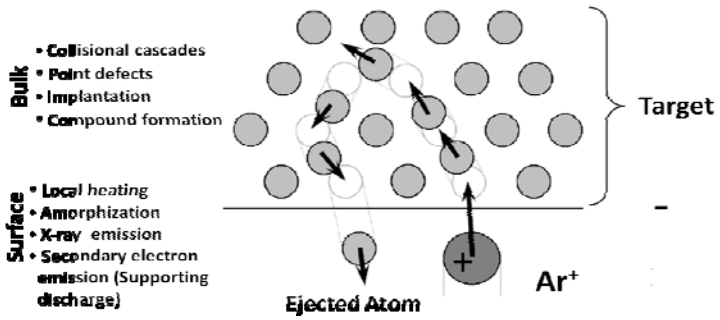

Figure 1- 9: Sputtering phenomenon

1.2.2.3 Transport of the material to the substrate

Sputtering processes are controlled by energy and momentum transfer (transport of the material), annealing effects and enhanced diffusion, which depends on the nature of the target material (metals, ceramic powder) by limiting their performance and create a need for process control[42] by handling the control parameters.

For instance, powder targets, prepared metallurgically, can release water vapor and if it is not properly degassed can cause surface chemical reactions. Additionally, in the presence of reactive or residual gases such as N_2, O_2 or hydrocarbons, chemical surface reactions occur and can cause compound formation on the target surface.

Usually these reactions result in reduced sputtering rate and compound formation is further intensified by a low target heat conductivity and cooling rate.

1.2.2.4 Condensation and Nucleation of the adsorbed atoms

The compounds that impinge on a surface in a vacuum environment (below 10^{-2} mbar) either are reflected immediately, re-evaporate after a residence time, or condense on the surface. During the re-evaporation stage, the atoms will have some degree of surface mobility over the surface before they try to condense again. The mobility of an atom on a surface will depend on the energy of the atom, atom-surface interactions (chemical bonding) and on the temperature of the surface. In the case of the strong atom-atom interaction (chemisorptions), surface mobility is low and each atom can act as a nucleation stage. Otherwise, desorption occurs and restarts the cycle of the PVD process[43].

Finally, the sources of different plasmas are summarized in Table 1-3 in order to compare them through their working pressure, electron temperature (T_{e^-}) and electron densities, respectively.

Plasma source	Gas pressure [mbar]	T_{e^-} [eV]	density [m^{-3}]
Capacitively coupled Radio Frequency (RF)	$6.6x10^{-2}$ - 1.3	3 - 6	10^{16} - 10^{17}
Capacitively coupled Direct current (DC)	$6.6x10^{-2}$ - 1.3	2 - 4	10^{15} - 10^{16}
Magnetron sputtering	$1.33x10^{-3}$ -$2.66x10^{-1}$	2 - 4	10^{14} - 10^{16}
Epitaxy	10^{-4} - $2.66x10^{-2}$	2 - 5	10^{14} - 10^{15}
DC arc jet	10 - 10^{3}	1 - 2	10^{18} - 10^{21}
Inductively coupled RF	10^{-4} - 1	1 - 10	10^{15}- $5x10^{18}$
Microwave ECR	10^{-5} - $2.6x10^{-2}$	1 - 15	10^{16} - 10^{18}
Microwave	10^{-3} - 1	1 - 15	10^{14} - 10^{17}

Table 1-3: Typical parameters of plasma sources used for thin film deposition[44].

1.2.3 Capacitive-coupled Radio frequency (RF) diode sputtering

Sputtering uses a glow discharge to generate a flux of ions incident on the target surface. Atoms are physically ejected from the surface target by momentum transfer i.e. the difference of the momentum of the ejected atoms to the incident atom (ex: Ar^+). Scattering caused by collision of ejected atoms within a glow discharge depends on the distance between the target and the substrate. When the target-to-substrate separation increases, the deposition rate decreases. In Addition, the scattering phenomenon increases with increasing gas pressure because the mean-free-path between collisions decreases as the pressure rises. Because of intense scattering within the discharge, ejected atom energies pass from a few tenths of an electron volt to a few electron volts arriving at the substrate (Figure 1- 10).

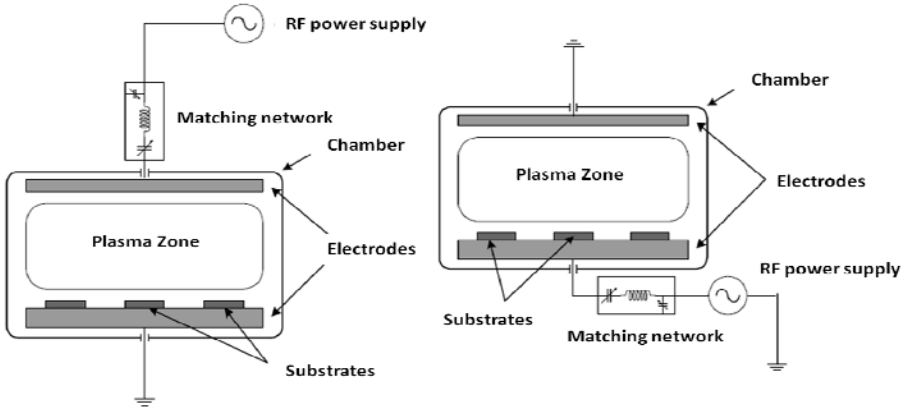

Figure 1- 10: Capacitive-coupled RF diode sputtering positively polarized (a) and negatively polarized substrate (b)

In low-pressure and high-voltage discharges, the mean free path between collisions is long, and it is statistically possible for a significant number of atoms to reach the substrate with high energies; these atoms are named energetic neutrals.

RF frequencies as the oscillating power source present several advantages depending on the frequency range i.e. when greater than 50 kHz, no conductive mode is needed for both electrodes because the electrodes can be coupled through an impedance. Greater than 1 megahertz (MHz), the ions do not undergo the oscillations of the potential due to their relatively large mass. Therefore, there is little accumulation at the cathode[45], and above 5 MHz, sputtering can be efficiently used. However standard frequencies as 13.56 MHz and 27 MHz are the specified frequencies required in industrial and medical use[46].

Various RF sputtering applications are possible and include deposition of metals, oxides, nitrides and carbides[47-49].

1.2.3.1 Magnetron sputtering

Compared to other techniques, the plasma is confined to the near-target region in a magnetron sputtering system. The secondary electrons (SE) i.e. electrons generated as ionization products are ejected above the target surface. SE is trapped by a strong magnetic field, increasing ionization, hence greatly improving the sputtering and deposition rates. The trajectories of the SE as spiral-like patterns skip across the surface of the cathode (see Figure 1- 11).

Targets with circular planar geometries are the most commonly used sources for all sputtering techniques including magnetron sputtering. However all planar magnetrons erode preferentially in the areas where the magnetic field is parallel to the target surface. Hence, annular distributions of sputtered atoms are often created as a racetrack-like erosion pattern. This technique is powerful as long as the target-to-substrate distance (d_{t-s}) is small. At large d_{t-s} distance, the ion bombardment of the films is frequently insufficient to produce dense film microstructures.

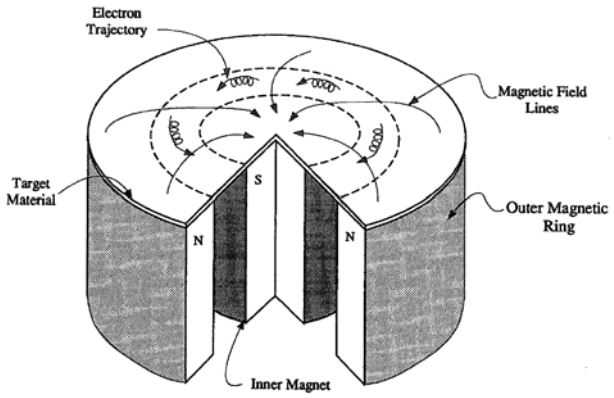

Figure 1- 11: Principle of magnetic field for a magnetron sputtering source

1.2.3.2 Unbalanced Magnetron Sputtering

To increase low-energy ion bombardment during film growth a new class of magnetron sources known as unbalanced magnetrons has been developed. In 1986, Window and Savvides[50] describe seven magnetic configurations and grouped them in three basic types I, II and intermediate (Figure 1- 12).

The type I magnetron is characterized by a weak outer pole and a strong inner pole. The type II is characterized by a strong outer pole and a weak inner pole. The intermediate known as balanced magnetron is typical of most conventional magnetrons.

The configuration of the magnetic field influences the efficiency of the target utilization. As shown in Figure 1- 12, the design of the type II distributes the energy of ions and electrons uniformly along the target. Whereas the type I condenses energy in the edges of the target. Therefore the sputtering yield increases with the type II which is of industrial interest in most applications.

In this study, the type II unbalanced magnetron sputter source have been used to extend the plasma. The restriction on the unbalanced magnetron systems is

that there must be an even number of cathodes so that the fields of each unbalanced magnetron cathode can be linked north pole to south pole with the adjacent cathodes. The interrelationship between cathodes is fairly complex because of the magnetic interactions and will differ according to the angle between cathodes[51].

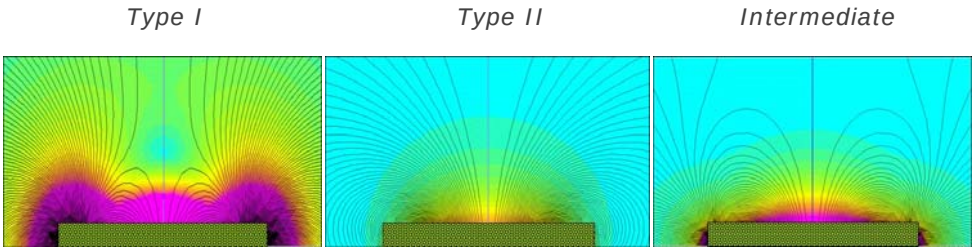

Figure 1- 12: Unbalanced magnetron (type I and II) vs. Balanced (Intermediate)

A variety of sputtering techniques can be used for BN deposition, but RF and magnetron sputtering seem to be most prevalent. Magnetrons are fairly common because they allow very low substrate temperatures.

1.2.3.3 Other sputtering processes

Some variants of previous process were also used to deposit BN as following:

- Triode sputtering: same design as the capacitive-coupled plasma (CCP) diode sputtering with an additional cathode used typically either as a simple biased conductor e.g. a tungsten filament or a thermionic electron emitter, providing a means of sustaining the discharge that is independent of the secondary electron generation used for diode sputtering.

- Ion plating: The principle is mainly to evaporate boron in the ionized gas medium composed either of nitrogen or ammonia (NH_3), or both, with an electron gun (0.1 eV and 3 keV) within a RF polarized discharge.

- Ion beam assisted deposition (IBAD): The ion source provides confined and directed Ar^+, N_2^+ plasma mixture to the substrate at low pressure, with controlled ion current and energy using a permanent magnet design. An additional source of electrons provided either by a tungsten filament, a hollow cathode electron source, or a plasma bridge neutralizer, is used to evaporate directly boron.

- Direct ion beam deposition (IBD): working with borazine ($B_3N_3H_6$) or other volatile compounds as boron source.

1.2.4 Summary of the CVD and PVD techniques

Furthermore, some techniques used successfully to deposit c-BN could be adapted to h-BN. The mechanisms to deposit h-BN (t-BN (0002) textured, with c axis parallel to the substrate) are multiple and similar to c-BN as the stress model, quenching model and sub-plantation model (Figure 1- 14). Different step to reach the desired layer are shown in Figure 1- 13.

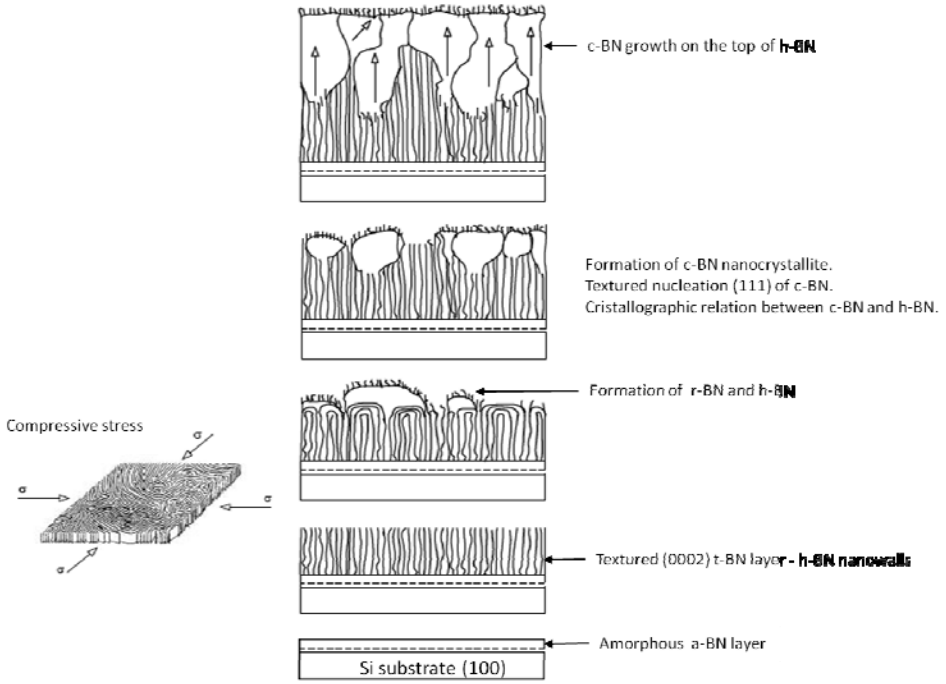

(a) *(b)*

Figure 1- 13: Orientation of graphite plane of h-BN film with a biaxial compression stress[9,52] (a). Steps of the nucleation and growth formations of h-BN and c-BN films (b)

In this case a lot of techniques in literature should be added as reference. An overview of all techniques is summarized in Table 1- 4.

Technique	Reactants	Comment	References
PVD method			
Sputtering (See Table 1-6)	B,BN,N_2 (Ar)	Films can be deposited without heating the substrate.	24,56
		Adhesion related to $T_{substrate}$ and polarisation	57
	N_2, H_2, h-BN target (Ar)	**Nanowalls formation without heating substrate.**	**110**
Evaporation (Ion platting)	H_3BO_3, NH_3,N_2	Ion beam plating of electron-beam-evaporated boron.	58-62
Electron beam evaporation	BN	Stable layers on Si substrates.	63-66
Ion beam evaporation (IBAD[1],MSIBD[2]) [1] Ion beam assisted evaporation [2] Mass Selected Ion Beam Deposition	B,N_2,NH_3 (Ar)	Ion beam plating of electron-beam-evaporated boron.	67-72
	B,N_2	• 30 keV N_2^+ ion bombardment on electron-beam-evaporated B. • With arc plasma or permanents magnets.	67, 73-77, 109
	$B_3N_3H_6$ (Ar)		78
Pulse plasma method	B_2H_6, B, N_2, H_2	Plasma decomposition, sp^3 structure.	79-80
Plasma jet	N_2,BCl_3 (Ar)	sp^2 and sp^3 structures	81-83
Ablation laser	Ar^+, N_2^+ , h-BN target	Laser CO_2, KrF, Nd-Yag, Ruby (Al_2O_3:Cr)	53,54,59
CVD method			
Conventional chemical vapour deposition (CVD)	B_2H_6, NH_3, N_2, H_2 (Ar)	• Vitreous and transparent deposition • 400°C< $T_{deposition}$<1250°C • Maximum deposition rate at 800°C	85-86
	BCl_3, NH_3, H_2 (Ar)	• 250°C< $T_{deposition}$ < 1250°C Films deposited at T< 450°C: unstable in a moist atmosphere • 1000°C<$T_{substrate}$<1250°C: Transparent and smooth BN film at substrate temperatures.	87-90
	BF_3, NH_3	X	91
	Hexachloroborazine	900°C< $T_{deposition}$<950°C: good adhesion of the films on silica while films on Si show cracks .	92
Molecular flow CVD (MFCVD)	$B_{10}H_{14}$, NH_3	Stochiometric BN films at $T_{substrate}$= 850°C	93-96
Low pressure CVD (LPCVD)	μ -trichloroborazine	$T_{deposition}$= 700°C: good insulating properties.	97
	BCl_3, NH_3	$T_{deposition}$ =900°C	98
	B_2H_6, NH_3	300°C< $T_{deposition}$<400°C: The optical and physical properties of the films formed are not changed after a long time at ambient condition.	99-100
	Borazine	Films formed between temperatures of about 300°C- 400°C, react with atmospheric moisture	99
	$B_3N_3Cl_6$, NH_3, BF_3	Amorphous hydrogenated boron nitride (a:BN-H) or hexagonal BN.	101
	B_2H_6, PH_3, NH_3	Hexagonal structure (low temperature)	55,102
Plasma enhanced CVD (PECVD)	B_2H_6, NH_3	$T_{deposition}$ = 1000°C, polycrystalline structure appears.	26
	B_2H_6, NH_3 (Ar)	$T_{deposition}$ = 300°C, amorphous structure, good insulating properties for semiconductor device applications.	103-104
	BCl_3, NH_3	550°C< $T_{deposition}$<620°C, amorphous structure, presence of Cl_2 in the coatings.	105
	$BH_3N(C_2H_5)_3$, NH_3 $BH_3N(CH_3)_2$ $B_3N_3H_3(CH_3)_2$	200°C< $T_{deposition}$<350°C, amorphous, good electrical properties for semiconductor device applications.	25,66, 106-108
	BBr_3 , NH_3		21
	BF_3, N_2 , H_2	T= 800°C: boron nitride nanowalls	36

Table 1- 4: The main synthesis methods of boron nitride[2,24]

1.3 Influence of deposition parameters on h-BN growth

1.3.1 Parameters

The most important parameter is the ionic bombardment due to its role to the formation of the c-BN phases by "the hammer penning-mechanical effect" (a-BN→h-BN (textured (0002) t-BN layer with c //substrate) →c-BN).

H-BN phase formation follows the same process as c-BN from the turbostratic phase of BN (disordered h-BN) with less energy of ionic species (Ei). The latter is defined by the interaction processes of energetic particles to surfaces and is described in

Table 1- 5.

PVD	Energy of ionic species (eV)	Mass of ionic species (kg)	Coefficient (dimensionless)	Ionic current (amps)	Atomic current (amps)	Incidence angle (°)
Ion beam evaporation (IBAD) [a]	E_i	m_i	γ_i	J_i	a	Θ_i
Mass selected ion beam evaporation (MSIBD) [b]			-	F_i	F_a	
Magnetron sputtering [c]			-			0°

Table 1- 5: The notation of parameters used to describe deposition. [a] Notation used on IBAD technique, [b] Notation used on MSIBD technique ,[c] Notation used on magnetron sputtering system.

The ionic current (F_i) is generally normalized by the atomic current (F_a) coming from the substrate. The substrate temperature and the substrate crystal structure as additional parameters are sometimes taken into account.

The origins of the hexagonal and cubic phase formations are schematically shown in Figure 1- 14.

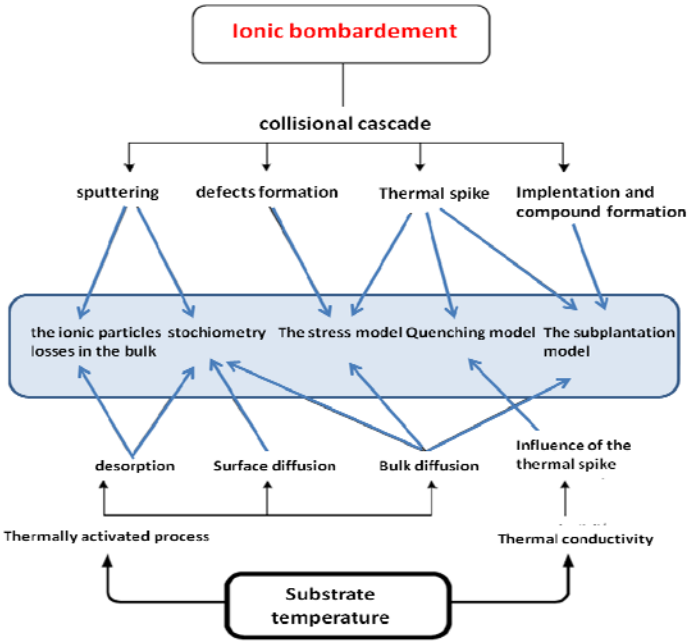

Figure 1- 14: Influence of ionic bombardment and temperature during h-BN deposition films[9].

1.3.2 Ionic bombardment

Different authors [70,72,111] observe that h-BN is formed at certain values of ion energy and the ratio of ion current to atoms deposited on substrate. There exists an h-BN formation threshold which can be defined by the experimental parameters such as mass of ions (m_i), energy of ions (E_i), current of ions (J_i) and the current of deposited atoms (a). The current of deposited atoms defines itself as the total current of boron and nitrogen atoms on substrate. Reinke et al.[112] have presented an interesting overview of BN thin film deposition, confirming the importance of the ion bombardment during the deposition and asserting that the parameters governing it i.e. the ionic current of boron deposited atoms J_i/a ($=F_i/F_a$) depending on the energy of ions obtained by IBAD (Figure 1- 15), must be related to the boron and nitrogen deposition rates. It should be noted that the formation of h-BN occurs with all the possible energies if the ratio of currents is high ($J/a< 0.5$).

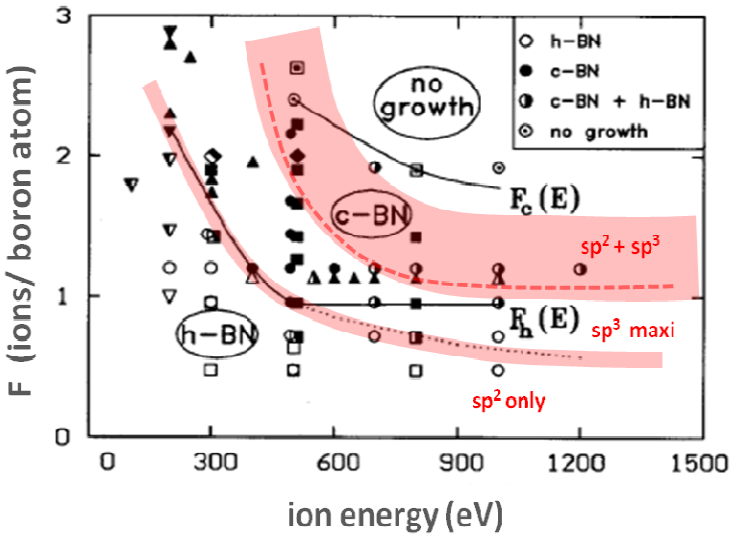

Figure 1- 15: Results on different BN phases performed by IBAD by transferring the current of ions per boron deposited atom depending on their energy. It points out the hexagonal phase formation [72,113,114].

1.3.3 Temperature effect

Generally, the increase of the substrate temperature promotes diffusion and desorption of the species within the layer, allowing the atomic rearrangement and thus reducing stress or improving crystalline quality. One can expect that the substrate temperature plays an important role for the quality of the crystal. Some studies show the existence of a minimum temperature threshold around $T_{s,\,min}$=150°C for the formation of h-BN. The increase of the temperature leads to sp^2 type bonding only if the total momentum transfer per boron deposited atoms is less than 200 $(eV.amu)^{1/2}$ (noted 200 u) (Figure 1- 16).

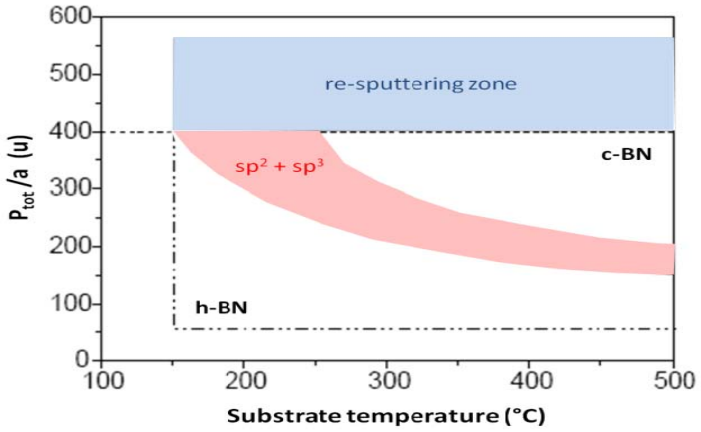

Figure 1- 16: Temperature threshold for the formation of h-BN[9,115] is 150°C ,if the total momentum transfer per boron deposited atoms (P_{tot} /a) is less than 200 (eV.amu)$^{1/2}$ (noted 200 u)

Mirkarimi et al.[116] suggest to consider the total momentum transfers per boron/nitrogen deposited atom (P_{tot}/a) not as simple collisions[72] but as collision cascades. They describe a threshold of different formation of BN phases observed using J_i/a (ionic current density normalized to atoms currents coming) mix into the momentum transfer (P_{tot}/a) transmitted by ions to atoms from the film and per atom deposited. Other important variables as the microstructure, the stoichiometry or as well intrinsic stress were added to this parameter (P_{tot}/a).

The equation obtained was adapted for IBAD and sputtering magnetron techniques, respectively:

$$P_{tot}/a = \sum_i (J_i/a)(2m_i E_i \gamma_i)^{1/2} \qquad (3.1)$$

Where i is the ionic species; E_i the energy of ionic specie; m_i the mass of ionic species and $\gamma_i = \dfrac{4m_i M}{(m_i + M)^2}$ with M the mass of atoms from the films.

For the magnetron sputtering techniques, one can define two parameters F_i and F_a (boron atom and/or nitrogen deposited) as follows:

$$F_i = 0.6 n_i \sqrt{\frac{kT_e}{m_i}} \quad \text{and} \quad F_a = \frac{v_c(m/s)\rho(g/cm^3)}{M(g/mol)} = \frac{2v_c\rho}{M}\left(\frac{atom}{cm^2}\cdot s\right) \qquad (3.2)$$

In both cases, $J_i/a = F_i/F_a$ and F_i represent the current of incident ions given by the Bohm plasma sheath criteria leading to a global supersonic condition and F_a, the current of deposited atoms on the substrate depending on the growth speed of the film (v_c), ρ is the density and M the molecular mass of BN.

Some additional condition should be taken concerning plasmas. In fact, for the magnetron sputtering, we do not have an mono-energetic current but a distribution of ion energies coming from the substrate, wherefore, it is necessary to get an average energy thus $E_i \to \langle E_i \rangle$ .Further, ion energy could be determined by bias voltage (V_B) and plasma potential (V_p) such as $E_i = ke(V_p + V_B)$ where k is a parameter depending on working pressure ($k = 1$ at p≤1x10^{-2} mbar; $k < 1$ at p>1x10^{-2} mbar) describing the type of predominant collisions in the sheath ($V_p < 0$).

So, the function is given by:

$$\langle P_{tot} \rangle / a = \sum_i (J_i/a)(2m_i \langle E_i \rangle)^{1/2} \qquad (3.3)$$

In summary, each approximation from this function gives some errors to the determination of the h-BN threshold formation in particular for magnetron sputtering techniques and generally for overall plasmas techniques.

1.3.4 Summary of the growth technique

There exist an "invariable" border between h-BN and c-BN phase formation which is independent of the applied method (CVD, PVD).

The mechanism of h-BN growth is the same for PVD or CVD techniques. In fact, they are both dominated by ionic bombardment and substrate temperature.

Into the mechanism of h-BN growth, one should add some secondary effects. These contributions do not proceed actively to the h-BN phase formation such as bombardment or temperature, but report the possibilities to obtain the h-BN phase or to explain the quality of the film:

- Stoichiometry: imperative condition for the h-BN formation.

- Impurities: the formation of the h-BN phase is allowed only when oxygen contamination is low (<4%)[117]. Higher oxygen rates exclude the possible h-BN formation (stacking defects), whereas higher carbon rate leads to crystallographic defects[118].

- The presence of hydrogen is recommended as a reduction agent for the preparation of pure h-BN[119]. Higher H_2 rates could lead to the destruction of the B-N bonds.

The latter point can explain the difference between films obtained by PVD or CVD methods. Some works have reported the influence of contaminants into the gas phase. Atomic hydrogen is inevitable within plasma CVD processes. In all cases where the formation of the h-BN phase is reported, atomic hydrogen is present within the bore precursors (B_2H_6, BHN $(CH_3)_3$).

In ion beam assisted deposition (IBAD), energetic ions B^+ have the same ion energy as nitrogen i.e. 100 to 500 eV.

In the PVD techniques, the energy of atoms and also ionized particles arriving to the substrate surface depend on the method (sputtering 3 eV, evaporation 0.1 eV)[9].

In the CVD technique, $BN_xC_yH_z$ non-defined, depend on different source gasses. Their fusion temperature is slightly above the ambient atmosphere pressure. For all of the methods, either physical or chemical assisted by ions, independently of the charge and the energy of boron species, the same domain of h-BN growth exists. Indeed, the plasmas are dealing with ion transport into the sheath by coupling the ion current to the electronic temperature of the plasma. As far as collisions in the sheath, depending on the working pressure, they involve the

average energy of ions. Nevertheless, these processes contribute less to the mechanism of h-BN growth and more to the understanding of the plasma physics.

The state of the art of h-BN growth by unbalanced magnetron sputtering constitutes the basis of this thesis. The different parameters which define the growth of h-BN are classified and summarized in Table 1-6.

Technique	Power (W)	Sub. T (°C)	Work pressure (mbar)	gas	Substrate	Growth rate (µm/h)	Ref.
Reactive sputtering	300	/	9,3 E-3	100% Ar 100%	(100) Si	0.45	120
RF magnetron sputtering (13,56 MHz) TORUS (1HV) ,RFX generator, ATX matching unit, bias voltage: by containing such to an auxiliary RF generator	120 (such 23W/cm2)	900	4 E -2	95% Ar 5% N_2	(100) Si	1.1	121
unbalanced RF magnetron (13,56MHz) sputtering	300	527	8 E-4	100% Ar		0.6	122
RF bias sputtering using a sintered h-BN target	1000	/		100% Ar	(100) Si	4,6 (-150	123
	1000					1,5 (-300 V)	
	2000					3,5 (-300 V)	
	1000					0,5 (-400 V)	
RF magnetron sputtering (27,12 MHz) substrate electrode connected via RF (27,12MHz)	400	<300	1 E-3	100% Ar	(100) Si	1,1 (-160V to -220V)	124
"Teer 550" unbalanced magnetron sputtering(13,56 MHz) using a sintered rectangle-shaped h-BN target, pulsed direct courant(PDC) negative biais	600	400	4 E -3	100% Ar 100% N_2 (Total flow rate=18 sccm)	(111) Si	0.36	125
	800					0.44	
	1000					0.62	
RF magnetron sputtering(13,56MHz) TORUS(1HV) using a pyrolitic h-BN,RFX 600 generator,ATX 600 matching unit	60-80 (such 12-16 W/cm2)	200-800	1,3 E-1 to 1,9E-1	83,3% Ar 16,6%N_2	(111)Ni foil (0,125 mm thick)	0.12	126
Bias sputtering with Target and the substrate electrode had their own RF power supplies (13,56 MHz), negative self-bias values	500	600	1.30E-02	100% Ar	(100) Si (32X32 mm2)	1.28	127
	1000		1.00E-02			1.37	
			2.60E-02			1.74	
			3.90E-02			0.69	
	1500		1.30E-02			2.56	
Bias sputtering with Target and the substrate electrode had their own RF power supplies (13,56 MHz),negative self-bias values	1000 (Target RF power) 30-350(Substrate RF power)	<300	1,3E-1 to 4E-1	Ar+N_2=50sccm 3% Ar 10%N_2	Si(111) wafers, thin cover glass sheets	0,55 (self-bias U=-100V) 0,18 (self-bias U=-500V)	128
Biais sputtering+ECR RF magnetron sputtering	600 and microwave ECR=200W	850	1.30E-03	Ar+N_2=50% 10 sccm Ar 10 sccm N_2	/	0.055	129
unbalanced RF magnetron (13,56MHz) sputtering	300	240-530	8.00E-04	Ar Kr	/	0.55	130
Biais sputtering		600	5,3E-4 to 2,1E-2	1% Ar	/	5,5 to 8,2	131,132
RF magnetron sputtering with a sintered h-BN target	360	300	1.00E-03	85% Ar 15% N_2	B(doped) -Si(100) P(doped) -Si(100) Glass	1-1,2	133
			4.00E-03	50% Ar 50% N_2	B(doped) -Si(100) Glass	1,15-1,37	
			1.00E-03	100% Ar+N_2	B(doped) -Si(100) P(doped) -Si(100) Glass Si+diamond Si+Ni (1,2,4 nm)	0,9-1,37	
			1E-3 1,4E-3	Ar+H_2 10%<H_2<30%		1 (10% H_2) 0,45 (30% H_2)	

Table 1-6: Synthesis of h-BN by unbalanced magnetron sputtering.

1.4 References

1. J.H. Edgar, Crystal structure, mechanical properties and thermal properties of BN, Properties of Group III Nitrides, Inspec. Publication, March **1994**.

2. S. Rudolph, *Am. Ceram. Soc. Bull.* **2000**, 79, 50.

3. P.B. Mirkarimi, K. McCarty, D. Medlin, *Mater. Sci. Eng. R* **1997**, 21, 47.

4. R. T. Paine, C.K. Narula, *Chem. Rev.* **1990**, 90, 73.

5. S.N. Grinyaev, V.V. Lopatin, *Sov. Phys. J.* **1992**, 35, 122.

6. M.Ueno, K. Hasegawa, R. Oshima, O. Shimomura, K. Takemura, H. Nakae, T. Matsuda, and T. Hirai, *Phys. Review B* **1992**, 45, 10226.

7. M.H. Manghnani, W.J. Nellis, M.F. Nicol, science and technology of high pressure: proceedings of AIRAPT-17, Honolulu, Hawaii 1999, 2, 937.

8. V.L. Solozhenko, V.Z. Turkevich, *J. Therm. Anal.* **1992**, 38, 1181.

9. A. Soltani, PhD thesis «Croissance de films minces de nitrure de bore hexagonal et cubique par depot chimique en phase vapeur assisté par plasma: Caracterisations optiques et électriques » Université de Metz (**2001**).

10. V. Mortet, PhD thesis « Croissance et caractérisation de couches minces de nitrure d'aluminium et de nitrure de bore cubique obtenues par pulvérisation triode » Université de Valenciennes et du Hainaut Cambrésis (**2001**).

11. T. Ouyang, Y. Chen, Y. Xie, K. Yang, Zh. Bao, J. Zhong, *Nanotechnology* **2010**, 21, 245701.

12. T. K. Pauli, P. Bhattacharya, D. N. Bose, *Appl. Phys. Lett.* **1990**, 56, 2648.

13. C. Li, Y. Bando, C. Y. Zhi, Y. Huang, D. Golberg, *Nanotechnology* **2009**, 20, 385707.

14. Y. H. Wu, P. W. Qiao, T. C. Chong, Z.X. Shen, *Adv. Mater.* **2002**, 14, 64.

15. Y. Kubota, K. Watanabe, O. Tsuda, T. Taniguchi, *Science* **2007**, 317, 932.

16. K.Watanabe, T.Taniguchi, H.Kanda, *Nat. Mater.* **2004**, 3, 404.

17. Y. Osaka, A. Chayahara, , H. Yokohama, M. Okamoto, T. Hamada, T. Imura, M. Fujisawa, *in Synthesis and Properties of Boron Nitride*, edited by J. J. Pouch and S. A. Alteroviz, *Mater. Sci. Forum* **1990,** 54-55, 277.

18. C. R. Dean, A. F. Young, I. Meric, C. Lee, L. Wang, S. Sorgenfrei, K. Watanabe, T. Taniguchi, P. Kim, K. L. Shepard, Hone, *Nature Nano.* **2010**, 5, 722.

19. J. L. Andujar, E. Bertran, Y. J. Maniette, *Appl. Phys.* **1996**, 80, 6553.

20. J. L. Huang, C. H. Pan, D. F. Lii, *Surf. Coat. Technol.* **1999**, 122, 166.

21. B.J. Choi, *Mater. Res. Bull.* **1999**, 34, 2215.

22. A. Soltani, P. Thévenin, A. Bath, *Mater. Sci. Eng. B* **2001**, 82, 170.

23. J. J. Pouch, S. A. Atterovitz, *Trans. Tech. Publications*, Brookfield, Vermont **1990**.

24. R. W. Pryor, *Appl.Phys.lett.*, **1995**, 68,pp.

25. S.P.S. Arya, A. D'Amico, *Thin Solid Films* **1988**, 157, 267.

26. W. Schmolla, H.L. Hartnagel, *Solid State Electron* **1983**, 26, 931.

27. S.B. Hyder, T.O. Yep, *J. Electrochem. Soc.* **1976**, 123, 1721.

28. A. Bath, P.J. Van Der Put, J.G.M. Becht, J. Schoonman, B. Lepley, *J. Appl. Phys.* **1991**, 70, 4366.

29. L.I. Maissel, R. Gland, *Handbook of Thin Film Technology*, McGraw-Hill, New York (1**970**) Chap. 16.

30. M. Hirayama, K. Shohno, *J. Electrochem. Soc.* **1975**, 122, 1671.

31. "Hexagonal Boron Nitride (hBN) - Applications from Metallurgy to Cosmetics". http://www.enotes.com/topic/Boron_nitride

32. Z. Remes, M. Nesládek, K. Haenen, K. Watanabe, T. Taniguchi, *phys. stat. sol. (a)* **2005**, 202, 2229.

33. K. Watanabe, T. Taniguchi, T. Niiyama, K. Miya, M. Taniguchi, *Nat. Photonics* **2009**, 3 (10), 591.

34. H. Kawarada, *Phys. Rev. B* **1993**, 47, 3633.

35. H. Kawarada, A. Yamaguchi, *Diam. Relat. Mater.* **1993**, 2, 100.

36. H. Kawarada, T. Tsutsumi, H. Hirayama, A. Yamaguchi, *Appl. Phys. Lett.* **1994**, 64, 451.

37. J. Yu, L. Qin, Y. Hao, S. Kuang, X. Bai, Y.-M. Chong, W. Zhang, E. Wang, *ACS Nano.* **2010**, 4, 414.

38. M. Hiramatsu, K. Shiji, H. Amano, M. Hori, *Appl. Phys. Lett.* **2004**, 84, 4708.

39. K. Teii, S. Shimada, M. Nakashima, A.T.H. Chuang, *J. Appl. Phys.* **2009**, 106, 084303.

40. K. Kobayashi, M. Tanimura, H. Nakai, A. Yoshimura, H. Yoshimura, K. Kojima, M. Tachibana, *J. Appl. Phys.* **2007**, 101, 094306.

41. J.M.E. Harper, in J.L. Vossen and W. Kern (eds.), *Thin Film Processes*, Academic Press (Bristol) **1978,** p.175.

42. C.R. Weissmantel, *Deposition of Metastable Films by Ion Beam and Plasma Techniques*, Proc. 9th Int. Vacuum Congress and 5th Int. Conf. on Solid Surfaces(Madrid),26 Sept-1 Oct **1983**, 229-308.

43. D.M. Mattox, Growth and Growth-Related Properties of Films Formed by Physical Vapor Deposition, ASM Handbook **1994**, Vol 5, pp 538-555.

44. S.M. Rossangel, J. Cuomo, W.D Westwood, *Handbook of plasma processing technology: Fundamentals, etching, deposition and surface interactions*, New York (**1990**).

45. J.A. Thornton, *Coating Deposition by sputtering*, *Deposition Technologies for thin Films and Coatings*, R.F. Bunshah, Ed., noyes Publications, **1982**,p 170-243.

46. R.J. Hill, Ed., *Physical Vapor Deposition*, Temscal, **1986**.

47. J.-E. Sundgren, B.-O. Johansson, S.-E. Karlsson, *Thin Solid Films* **1983**, 105, 353.

48. J.-E. Sundgren, B.-O. Johansson, S.-E. Karlsson, H.T.G. Hentzell, *Thin Solid Films* **1983**, 105, 367.

49. J.-E. Sundgren, B.-O. Johansson, S.-E. Karlsson, H.T.G. Hentzell, *Thin Solid Films* **1983**,105, 385.

50. B. Window, N. Savvides, *J. Vac. Sci. Technol. A* **1986**, 4, 196.

51. S. Rohde, *"Metal-Nitride Thin Films Deposited by Unbalanced Magnetron Sputtering," Dissertation*, Northwestern University, **1991**.

52. D.R. McKenzie, W.D. McFall, S. Reisch, B.W. James, I.S. Falconer, R.W. Boswell, H Persing, A.J. Perry, A. Durandet, *Surf. Coat. Technol.* **1996**, 78**,** 255.

53. T. K. Paul, P. Bhattacharya, D. N. Bose, *Appl. Phys. Lett.* **1990**, 56, 2648.

54. S. Mineta, M. Kohata, N. Yasunaga, Y. Kikuta, *Thin Solid Films* **1990**, 189,125.

55. C.R. Jr. Eddy, B.D. Sartwell, *J. Vac. Sci. Techno. A* **1995**, 13, 2018.

56. M.D. Wiggins, C.R. Aita, F.S. Hickernell, J*. Vac. Sci. Technol. A* **1984**, 2, 322.

57. N. Yamashita, T. Wada, M. Ogawa, T. Kobayashi, H. Tsukamoto, T. Rokkaku, *Surf. Coat. Technol.* **1992**, 54/55, 418.

58. H.A. Beale, *US Patent 4297387* **1980**.

59. K. Inagawa, K. Watanabe, H. Ohsone, K. Saitoh, A. Itoh, *J. Vac. Sci. Technol. A* **1987**, 5, 2696.

60. K.L. Chopra, V. Agarwal, V.D. Vanker, C.V. Deshpandey, R.F. Bunshah, *Thin Solid Films* **1985**, 126, 307.

61. R.F. Bunshah, *Handbook of Deposition Technologies for Films and Coatings*, Second Edition, Noyes Publications, Park Ridge, New Jersey, USA (**1994**).

62. P. Lin, C. Deshpandey, H.J. Doerr, R.F. Bunshah, K.L. Chopra, V. Vankar, *Thin Solid Films* **1987**, 153, 487.

63. M. Murakawa, S. Watanabe, *Surf. Coat. Technology* **1990**, 43/44, 128.

64. Y. H. Jeong, S. K. Jo, B. H. Lee, T. Sugano, *IEEE Electr. Device L.* **1995**, 16, 109.

65. D. Litvinov, C.A. Taylor II, R. Clarke, *Diam. Relat. Mater.* **1998**, 7, 360.

66. S.Y. Shapoval, V.T. Petrashov, O.A. Popov, A.O. Westner, M.D. Jr. Yoder, C.K.C. Lok, *Appl. Phys. Lett.* **1990**, 57, 1885.

67. C. Weissmantel, K. Bewilogua, D. Dietrich, H-J. Erler, H-J. Hinneberg, S. Klose, W. Norwick, G. Reisse, *Thin Solid Films* **1980**, 72,19.

68. B. Rother, H. D. Zscheile, C. Weissmantel, C. Heiser, G. Holzhüter, G. Leonhardt, P. Reich, *Thin Solid Films* **1986**, 142, 83.

69. C. Weissmantel, K. Bewilogua, K. Breuer, D. Dietrich, U. Ebersbach, H-J. Erler, R. Rau, G. Reisse, *Thin Solid Films* **1982**, 96, 31.

70. T. Ikeda, *Appl. Phys. Lett.* **1992**, 61, 786.

71. S. Watanabe, S. Miyake, W. Zhou, Y. Ikuhara, T. Suzuki, M. Murakawa, *Appl. Phys. Lett.* **1995**, 66, 1478.

72. D.J. Kester, R. Messier, *J. Appl. Phys.* **1992**, 72, 504.

73. S. Shanfield, R. Wolfson, *J. Vac. Sci. Technol. A* **1983**, 3, 323.

74. W. Halverson, D.T. Quinto, *J. Vac. Sci. Technol. A* **1985**, 3, 2141.

75. C. Weissmantel, K. Brewer, B. Winde, *Thin Solid Films* **1983**, 100, 383.

76. D. Bouchier, W. Möller, *Surf. Coat. Technol.* **1992**, 51, 190.

77. M. Kuhr, S. Reinke, W. Kullisch, *Diam. Relat. Mater.* **1995**, 4, 375.

78. M. Satou, F. Fujimoto, *Jap. J. Appl.* **1983**, 22, 171.

79. M. Sokolowski, *J. Crystal Growth* **1979**, 46, 136.

80. M. Sokolowski, A. Sokolowka, A. Michalski, Z. Romanowski, A. Rusek-Mazurek, M. Wronikowski, *Thin Solid Films* **1981**, 80, 248.

81. D.H. Berns, M.A. Cappelli, *Appl. Phys. Lett.* **1996**, 68, 19.

82. K. Fukushima, M. Tobioka, *Jpn. Kokai Tokkyo Koho (Japanese Patent)* **1989**, 36,759.

83. K. Fukushima, M. Tobioka, *Jpn. Kokai Tokkyo Koho (Japanese Patent)* **1988**, 63,662.

84. A. Ikegaya, M. Tobioka, *Jpn Kokai Tokkyo Koho (Japanese Patent)* **1988**, 63, 179.

85. S.P. Murarka, C.C. Chang, D.N.K. Wang, T.E. Smith, *J. Electrochem. Soc.* **1979**, 126, 1951.

86. M. Hirayama, K. Shohno, *J. Electrochem. Soc.* **1975**, 122, 1671.

87. W. Boronian, *Mat. Res. Bull.* **1987**, 7, 119.

88. T. Takahashi, H. Itoh, M. Kuroda, *J. Cryst. Growth* **1981**, 53, 418.

89. G. Clerc, P. Gerlach, Proc. 5th Int. Conf. on Chemical Vapour Deposition, U.K. **1975,** 777-785.

90. J.J. Gebhardt, Proc. 4th Int. Conf. on Chemical Vapour Deposition, U.K. **1973**, 460-472.

91. H.O. Pierson, *J. Composite Mat.* **1975**, 9, 228.

92. G. Constant, R. Feurer, *J. Less Common Met.* **1981**, 82,113.

93. K. Nakamura, *J. Electrochem. Soc.* **1985**, 132, 1757.

94. S. Nakamura, T. Mukai, *Jpn. J. Appl. Phys.* **1992**, 31,1457.

[95.] S. Nakamura, N. Iwasa, S. Nagahama, *Jpn. J. Appl. Phys.* **1993**, 32,338.

[96.] S. Nakamura, T. Mukai, M. Senoh, *Jpn. J. Appl. Phys.* **1993**, 32,16.

[97.] N.Patibandla, K.L. Luthra, *J. Electrochem. Soc.***1992**, 139, 3558.

[98.] K. Sugiyama, H. Itoh, *Mater. Sci. Forum* **1990**, 54/55, 141.

[99.] A.C. Adams, *J. Electrochem. Soc.* **1981**, 128, 1378.

[100.] A.C. Adams, C.D. Capio, *J. Electrochem. Soc.* **1980**, 127, 399.

[101.] H. Saitoh,; T. Hirose, T. Ohtsuka, Y. Ichinose, *Appl. Phys. Lett.* **1994**, 64, 1638.

[102.] E. Yamaguchi, M. Minakata, *J. Appl. Phys.* **1984**, 55, 3098.

[103.] H. Miyamoto, M. Hirose, Y. Osaka, *Jap. J. Appl. Phys.* **1983**, 22,216.

[104.] T.H. Yuzuriha, D.W. Hess, *Thin Solid Films* **1986**, 140, 199.

[105.] O. Gafri, A. Grill, D. Itzhak, A. Inspektor, R. Avni, *Thin Solid Films* **1980**, 72, 523.

[106.] W. Schmolla, H. L. Hartnagel, *J. Electrochem. Soc.* **1982**, 129, 2636.

[107.] W. Schmolla, *Int. J. Electronics* **1985**, 58, 35.

[108.] A. Bath, P.J. Van Der Put, , J.G.M. Becht, J. Schoonman, B. Lepley, *J. Appl. Phys.* **1991**,70, 4366.

[109.] N. Savvides, *Thin Solid Films* **1988**, 163, 13.

[110.] B. BenMoussa, J. D'Haen, C. Borschel, A. Soltani, M. Saitner, V. Mortet, C. Ronning, M. D'Olieslaeger, H-G. Boyen, K. Haenen. *MRS online Proceeding Library **1307**, mrsf10-cc06-09 (2011)*.

[111.] N. Tanabe, T. Hayashi, M. Iwaki, *Diam. Relat. Mater.* **1992**, 1,151.

[112.] S. Reinke, M. Kuhr, W. Kullisch, R. Kassing, *Diam. Relat. Mater.* **1995**, 4, 272.

[113.] S. Reinke, PhD Thesis, Kassel University (**1996**).

[114.] D. Bouchier, H. Séne, M.A. Djouadi, P. Möller, *Nucl. Instrum. Methods B* **1994**, 89, 369.

[115.] K.F. McCarty, D.L. Medlin, *Diam. Relat. Mater.* **1997**, 6, 1219.

[116.] P.B. Mirkarimi, K.F. McCarty, D.L. Medlin, W.G. Wolfer, T.A. Friedmann, E.J. Klaus, G.F. Cardianle, D.G. Howitt, *J. Mater. Res.* **1994**, 9, 2925.

[117.] H.B. Luthje, K. Bewilogua, S. Daaud, M. Johansson, L. Hulman, *Thin Solid Films* **1995**, 247, 40.

[118.] S.L. Delage, *Handbook Thomson CSF Beam Processing Technology, VLSI Electronics Series*

[119.] M. Hubáček, M. Ueki, *J. Solid State Chem.* **1996**, 123, 215.

[120.] M.D. Wiggins, C.R. Aita, *J. Vac. Sci. Technol. A* **1984**, 2, 2.

[121.] J.M. Caicedo, G. Bejarano, G. Zambrano, E. Baca, O. Moran, P. Prieto, *phys. stat. sol. B* **2005** ,242,1920.

[122.] S. Ulrich, J. Scherer, J. Schwan, I. Barzen, K. Jung, M. Scheib, H. Ehrhardt, *Appl. Phys. Lett.* **1996**, 68, 7.

[123.] D.V. Shtansky, O. Tsuda, Y. Ikuhara, T. Yoshida, *Acta mater.* **2000**, 48, 3745.

[124.] J. Ye, U. Rothhaar, H. Oechsner, *Surf. Coat. Technol.* **1998**,105,159.

[125.] X.Z. Ding, X. T. Zeng, H. Xie, *Thin Solid Films* **2003**, 429, 22.

[126.] Z.F. Zhou, I. Bello, V. Kremnican, M.K. Fung, K.H. Lai, K.Y. Li, C.S. Lee, S.T. Lee, *Thin Solid Films* **2000**, 368, 292.

[127.] M. Mieno, T. Yoshida, *Jpn. J. Appl.Phys.* **1990**, 29,175.

[128.] K. Bewilogua, J. Buth, H. Hiabsch, M. Grischke, *Diam. Relat. Mater.* **1993**, 2, 1206.

[129.] S.C. Kinder, A. Taylor II, R. Clarke, *Appl. Phys. Lett.* **1994**, 64, 1859.

[130.] S. Ulrich, J. Scherer, L. Schwan, I. Barzen, K. Jung, H. Ehrhardt, *Diamond Relat. Mater.* **1995**, 4, 288.

[131.] O. Tsuda, Y. Yamada, T. Fujii, T. Yoshida, *J. Vac. Sci. Technol . A* **1995**, 13, 2483.

[132.] O. Tsuda, Y. Yamada, Y. Tatebayashi, T. Yoshida, *Proc.12th Int. Syrup. on Plasma Chemistry*, **1995**, 2041.

[133.] S. Gimeno, J.C. Mufioz, A. Lousa, *Diam. Relat. Mater.* **1998**, 7,853.

Chapter 2 Procedure & analysis of film deposition

In this chapter, the easy to handle, scalable and cost effective reactive radio frequency magnetron sputtering (RF-MS) process is used in combination with a boron nitride (BN) target with the aim of depositing thin hexagonal boron nitride (h-BN) films. Using different $N_2/Ar/H_2$ gas compositions in combination with different substrates such as silicon Si (100), fused silica or quartz (0001), h-BN films of different thickness are deposited.

First, it was necessary to carry out a number of technical steps to eliminate contaminations. In addition, controlling deposition conditions is needed to grow hexagonal boron nitride of good quality, reproducible and uniform thickness films. A set of techniques used to characterize thin films will also be presented here.

2.1 Description of the RF unbalanced magnetron sputtering system

The home made experimental RF-MS setup used in this study is schematically shown in Figure 2-1.The chamber is equipped with circular parallel-plate electrodes separated by 40 mm. One of the electrodes, located on the top, is a pure and dense h-BN disc (99.99% purity, 1.96 g/cm^3) used as target material and acts as unbalanced magnetron sputtering cathode (TORUS 3HV) with a nominal RF sputtering power of 300 W used as a plasma source. For security reasons and due to plasma column heating, RF power supply has not exceeded 300W. The effective power during the deposition was 75 W .The other electrode is the sample holder at the bottom, connected to the ground.

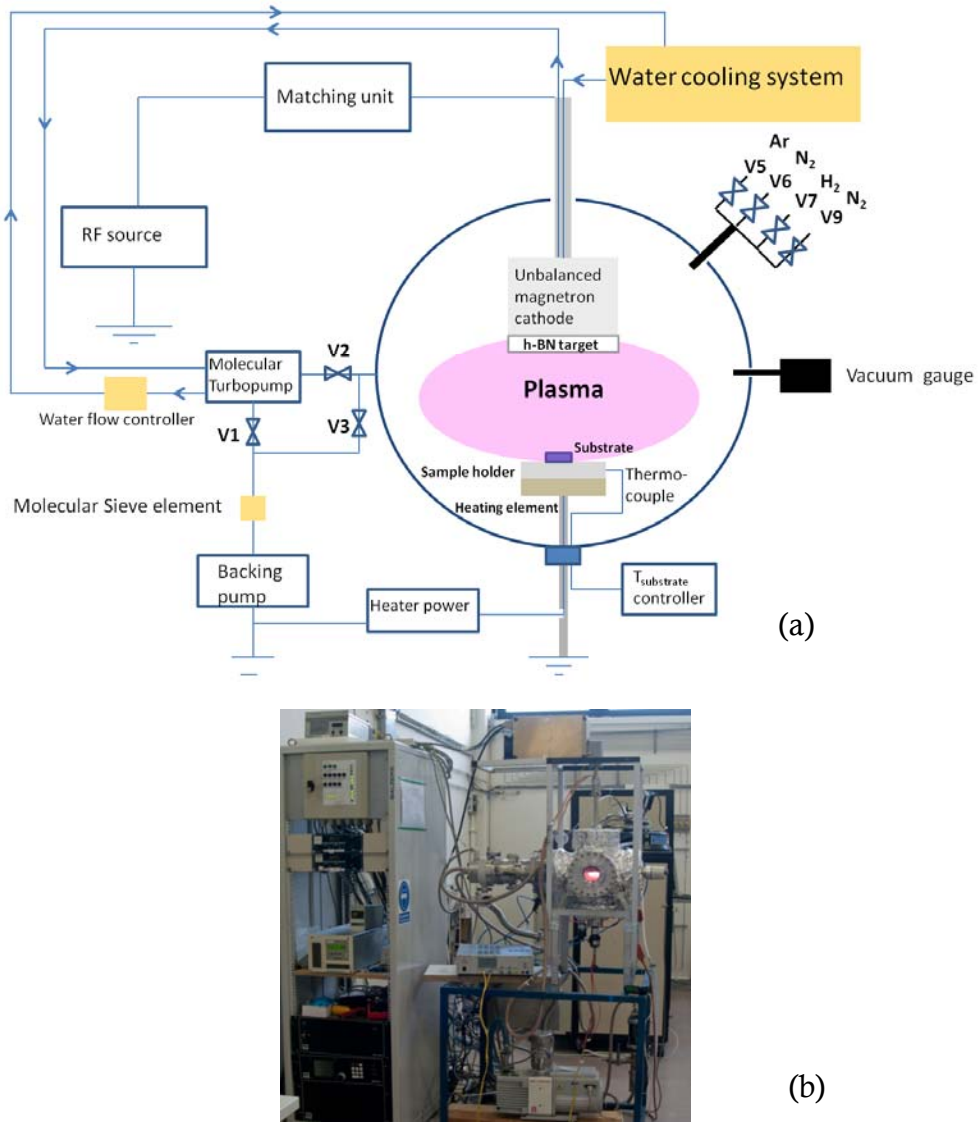

Figure 2-1: Schematic of the RF-MS apparatus (a). Photograph of the RF-MS reactor present at IMO (b).

The glow discharge is sustained by the radio frequency (RF) electric field between these two electrodes. The electric field depends on different parameters such as the size of the substrate holder (electrode) compared to the cathode, the distance between target and substrate, the pumping system, where a threshold vacuum pressure is needed to generate plasma, and the choice of the gas.

2.1.1 Radio-frequency (RF) source

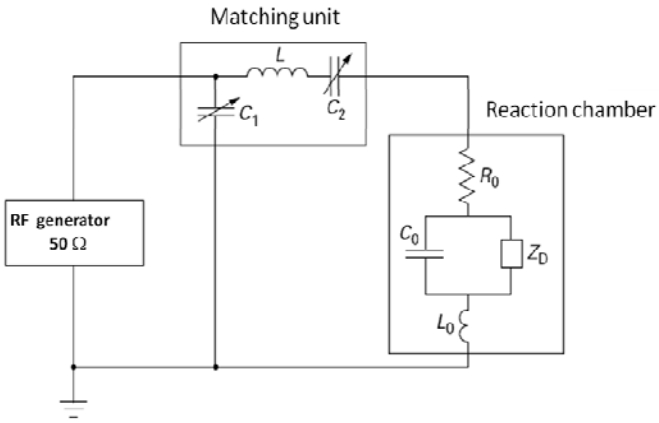

Figure 2-2: Electrical diagram equivalent to the RF discharge.

This system (Figure 2-2) is composed of several elements:

- Radio-frequency (RF) plasma generator (ACG-6B) of 13,6 MHz, designed to a rated power output of 600 W into 50 ohms suitable loads.
- An automatic matching network (MW-10D) is an inductor (L) circuit, interfaced between the cathode connected to the reaction chamber and the RF output coaxial cable from the RF generator. The 13.56 MHz RF plasma generator is required to reduce ohmic losses, which anticipates the lower plasma radiation resistance. The capacitive matching network consists of a variable combination of high-voltage vacuum variable

capacitors (C_1 and C_2) with series resistances .Their choice depends on source type, geometry and electrical characterization. The match box is enclosed in a conducting box to provide RF shielding. That is to obtain a reflected power to zero or near zero. Only high-quality 50 Ohms (Ω) coaxial cable should be used between generator (50Ω) and the load. However, the impedance equivalent to the excitatrice structure in the presence of the plasma must be equivalent to 50Ω, to get a maximum of power into the RF electrode.

Without any bias voltage, the potential of the cathode (V_c), called floating potential (V_f), is negative regarding to the plasma potential (V_p) when the plasma is stabilized. The anode (sample holder + walls) undergoes a ionic bombardment of energies $e^-(V_f - V_p)$ where e is electron. Using the self-polarization voltage (V_{self}), the energy of ions will be given by $e^-(V_{self}-V_p)$.

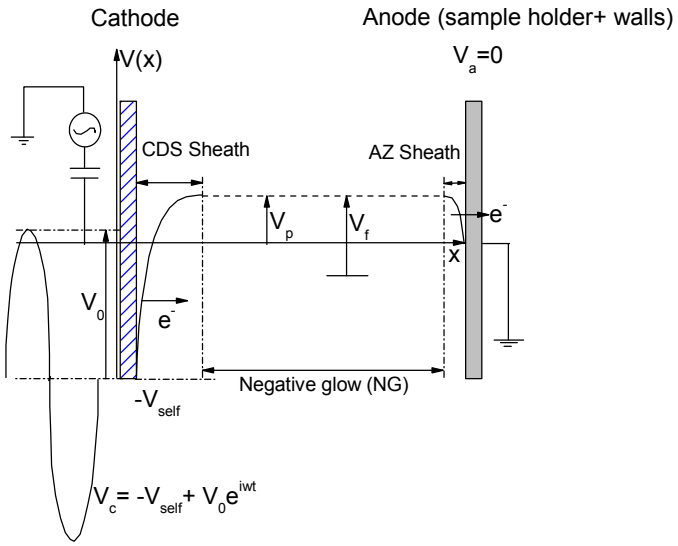

Figure 2-3: Potential distribution in the glow discharge[1,4].

The so-called low-temperature plasmas or more precisely the negative glow (NG) gas discharges[3] are considered as a virtual electric field free between the electrodes. The electric fields in the system are restricted to each adjacent side of the electrodes by sheaths[1]. Near the cathode (h-BN target) appears a cathode dark space (CDS) or plasma sheath (Figure 2-3). The dark region means that no

ionization happens in this region allowing thus electrons and positive ions to accelerate towards the cathode without any scattering. They cause the sputtering of the cathode material and the emission of secondary electrons which is trapped afterward by magnetic shield. The thickness of this region depends on polarization voltage and can vary until 1 cm. The CDS sheath fields repel electrons, having a much higher mobility than ions, trying to reach the cathode[1]. Indeed, the plasma potential (V_p) in the glow discharge is always higher than the adjacent anode zone (AZ), thus reducing the electron loss rate towards the walls. Moreover, the color of the optical emission of the plasma is characteristic of the target material, gas species, pressure, excitation, and so on (Figure 2-4).

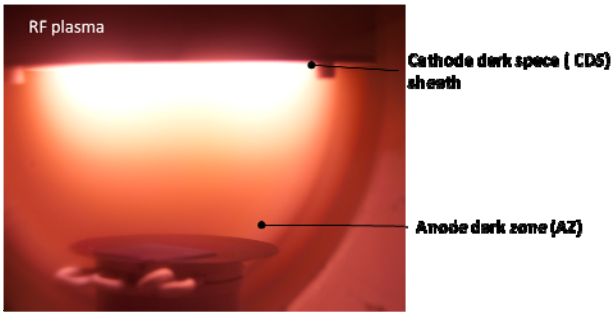

Figure 2-4: Picture of the plasma ball during the h-BN growth process with reactant gasses: 5 % H_2; 44 % N_2 and discharge gas: 51 % Ar.

2.1.2 Substrate holder with heating element

It is composed of a molybdenum circular piece (Figure 2-5) and a heating element which is sandwiched with another circular piece (molybdenum).The heating element is an Inconel alloy sheat (Philips thermocoax), ∅ 2 mm (diameter), R=3.1 $\Omega.m^{-1}$ at 20°C. The maximum temperature accessible for the heating element is 800°C.

Its temperature is controlled by a heating power supply (0-10 A) with a thermocouple type K (chromel–alumel) placed under the substrate holder and connected to a temperature read-out unit, respectively.

The depositions were made on substrates whose surface is typically 1x1 cm^2. Some of them were achieved on 2x2 cm^2 e.g. for mass density measurement, roughness and Fourier transform infrared spectroscopy in oblique transmission.

To insert or move substrates out of the deposition chamber, they are fixed prior on a 2'' inch silicon (100) wafer, and sustained on the top of the molybdenum circular piece.

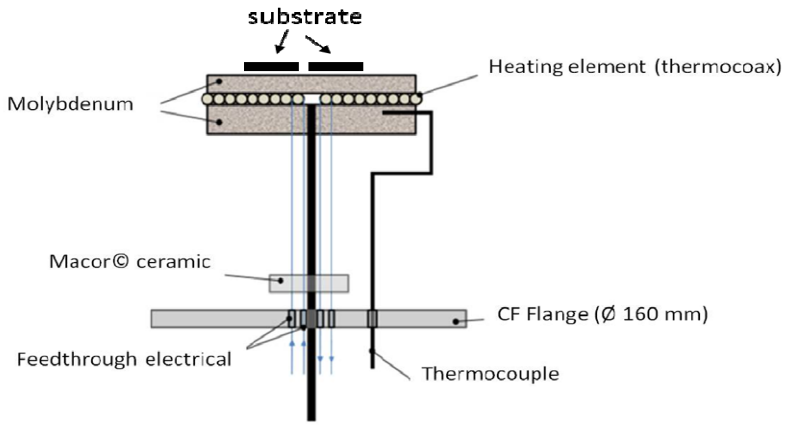

Figure 2-5: Cross section of sample holder with heating element.

2.1.3 Enhanced substrate holder

After, a vacuum leak was detected from a linear homemade feedthrough, new linear and rotary position locks (UHV-compatible) were installed with a new sample holder stage (Figure 2- 6). It is composed of a shutter blade and a heating element with the same characteristic as the previous substrate holder, followed by a bias connection. Two inox connection heating cables are sandwiched by three insulators, such as the Macor ceramic. The maximum temperature accessible for the heating element is 800°C.

Its temperature is controlled by a heating power supply (0-10 A) and the read-out temperature is checked using a infrared thermometer (Minolta/Land Cyclops 52). The vacuum pressure was improved to optimize the h-BN growth. Biasing the sample holder with either DC (direct current) or RF (radio-frequency) power supply will allow to synthesize the cubic boron nitride in the future (not used in this study).

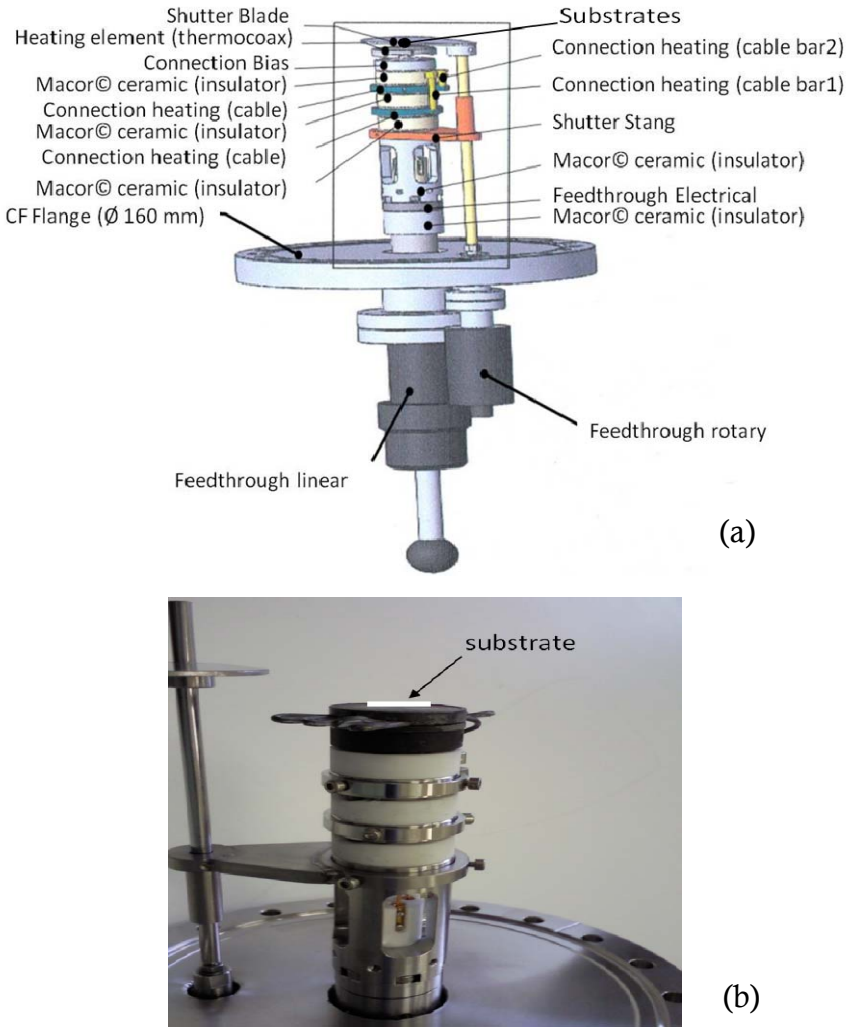

Figure 2- 6: Biased sample holder stage with linear and rotary feedthrough: schematic representation (a), and photograph (b)

2.1.4 Pumping system

The pneumatic valve V1 and a gate pneumatic valve V2 allow to control a turbo pump TPH 240 (Volume flow rate for Nitrogen (N_2) = 230 l /s, Helium = 240 l/s,

Hydrogen (H_2) = 210 l/s), and are shunted with a rotary oil pump (16 m^3/h) controlled by a pneumatic valve V3 (Figure 2-1). The pressure was measured by a duo of Pirani vacuum gauges (till 10^{-3}-10^{-4} mbar) and cold cathode (till 10^{-9} mbar). The deposition chamber is a grey cast iron chamber whose inner surface is almost 2500 cm² and the volume is 13200 cm³, closed by stainless steel flanges.

2.1.5 Gas lines

2.1.5.1 Choice of gases

Here, each gas line is equipped with a pneumatic valve (V5, V6, V7, V9) and a MKS mass flow controller is determined by their volume as a standard cubic centimeter per second (sccm) (Figure 2-1). Argon (Ar) as an inert gas, is controlled by the V5 pneumatic valve and its mass flow is 69.5 sccm. Ar does not interact directly in the formation of compounds on either the target or the substrate due to the saturation of its valence band. Ar is used as a discharge gas to generate plasma and to sputter material from the target. There are two main reasons to choose argon. First, its mass is high enough to ensure adequate sputtering yields and secondly it is less expensive compared to xenon or krypton[5].

The percentage of nitrogen (N_2) and hydrogen (H_2), used as reactive gas within the gas of discharge (Ar), determine the stoichiometry of the deposited film (see chap 3, section 3.2.1). Here, the gas lines of nitrogen (N_2) and hydrogen (H_2) are monitored by V6, V7, respectively and its mass flow is 50 sccm, 100 sccm, respectively. An additional nitrogen (N_2) gas line is used to flush the deposition chamber in order to reach the atmospheric pressure before opening the deposition chamber. The working pressures vary from $1.7x10^{-2}$ mbar to $3.1x\ 10^{-1}$ mbar.

2.1.5.2 Purity control of gases

Optical emission spectroscopy (OES) was made to control the purity of gases used in this studies. An oxygen spectrum measured in Ulm university and shown in Figure 2- 7 a and Figure 2- 7 b, is used for a comparison in the experimental conditions of the plasmas. No presence of oxygen is detected in Ar plasma and N_2 plasma measured at IMO.

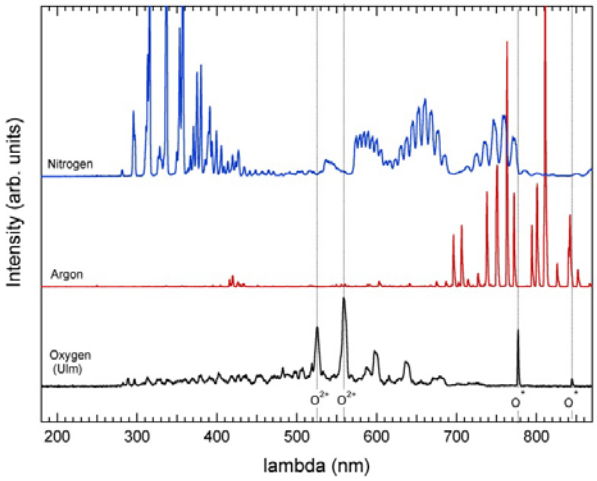

(a)

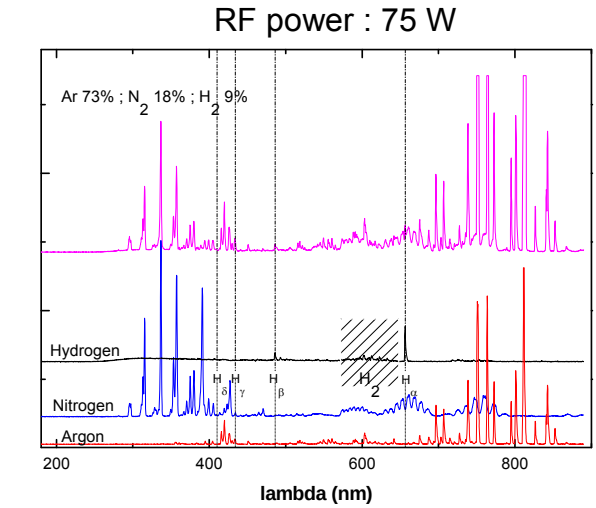

(b)

Figure 2- 7: Optical emission spectroscopy (OES) spectra of Ar, N_2 (IMO) and O_2 plasmas (Ulm university)(a).Control of gas purity in the condition of growth at IMO (b).

2.1.6 Growth Procedure

2.1.6.1 In-situ cleaning of deposition chamber

At the beginning of the study, an intensive cleaning was made using isopropanol and soap water. Then, a polytrifluoroethylene (PTFE) heating tapes (max. surface temperature: 260°C) i.e. PTFE-Teflon® isolated heating conductor with mesh wire and glass fibre coating, covering the outside of the deposition chamber, has been heated continuously during several days. Before each deposition, the reactor is cleaned with pure H_2 plasma after activating a plasma by Ar. Few minutes were enough for stripping of contaminants from the substrates and walls. Figure 2- 8 shows the stripping efficiency of these as evidenced by FTIR spectra from 200 nm thick BN films deposited on Si. This procedure was efficient to enhance the reproducibility and the quality of films. After a great number of depositions, the reproducibility and better quality were proven without using presputtering H_2 plasma from FTIR spectra. Thereafter, the procedure without using presputtering H_2 plasma will be retained.

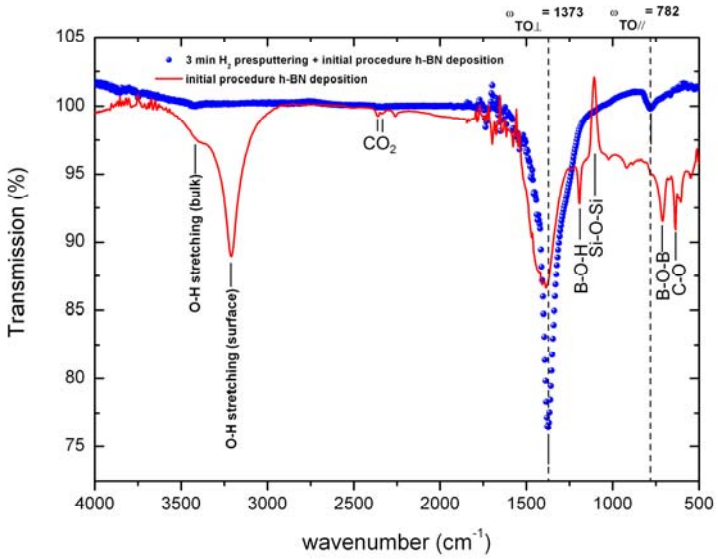

Figure 2- 8: Infrared spectra of h-BN film, 200 nm thick using deposition procedure with and without H_2 presputtering. $TO_{\perp}$ and $TO_{//}$, features of h-BN phase, will be explained further (chapter 4, 4.2.3)

2.1.6.2 Pretreatment of substrates

Depending on the type of substrates, at least two ex-situ cleaning procedures are required. An organic cleaning (steps 1 & 2) used to oxidize the surface and eliminate some persistent traces of contaminants followed by the step 3, are shared by all of them (silicon, quartz, fused silica, sapphire). Then a chemical cleaning (steps 4 & 5) was made only for silicon to remove the oxide interface formed during the first steps of cleaning, and to put a clean oxide as a protective film efficient during couple of hours.

1. *15 min. in acetone solution under ultrasonic vibration bath.*
2. *15 min. in hot ethanol solution under ultrasonic vibration bath.*
3. *Rinsing with deionized water.*
4. *2 min. in 40% HF concentrated solution under ultrasonic vibration bath.*
5. *Rinsing with deionized water.*
6. *Drying under nitrogen flow (common to all samples)*

2.1.6.3 Substrate positioning

Samples are positioned on a 2 inch silicon wafer, placed on sample holder with a clamp and immediately protected by the shutter (shutter on) to the target. Then, one proceeds to the pumping of the system. At the same time, the system is covered with heating tapes and aluminum foil, the former which is controlled by a heating power supply and set at 120°C during one night in order to boost the outgassing.

2.1.6.4 Procedure

When the vacuum reaches its lowest value around $2x10^{-8}$ mbar, the deposition procedure is started as following:

1. Ar gas is introduced in the chamber to switch on the plasma (discharge gas). During one hour at low power (20 W), with the shutter on the substrate, Ar plasma is used to clean the slightly oxidized target and substrate, contaminated with air during the opening of the deposition chamber.

2. Adjustment of Ar, N_2 and H_2 flows according to the deposition conditions. Plasmas are kept during 10 min at higher power (75 W) to be stabilized with the shutter on the substrate.
3. Then, till the shutter is rotated to start the growth until the desired thickness is reached.

2.2 Characterization techniques

In this paragraph, one present different tools of characterization used to determine the h-BN film properties. First part will be consecrated to chemical-physical techniques which inform about chemical composition of the deposits i.e. impurities, stochiometry, crystalline structure and optical properties. The second part, more specific, is applied to the microscopic surface imaging of films. These studies have the aim to improve films quality by optimization of deposition conditions. Some of them will be used systematically (FTIR, UV-Vis, EDS, FESEM) and other more occasionally (Raman, XPS, RBS, XRD, AFM, CFM, TEM, and CL).

2.2.1 Gravitometric measurements

These deposits samples were measured by Sartorius (CP64) micrometric balance. One of the most important parameter is the material density[4,6] $\rho_F\left(g.cm^{-3}\right)$ which is given by:

$$\rho_F = \frac{M_F}{S.t_F} \qquad (2.1)$$

Where $M_F(g)$ is the difference of mass taken after and before deposition; $S\left(cm^2\right)$ is the substrate surface; $t_F(cm)$ the film thickness. The relative uncertainty of measurements is between 5% to 10% and it is reduced when the film is thicker.

2.2.2 Stress determination on thin film

Dektak3ST surface profiler technique allows to appreciate the order of the intrinsic stress of thin films. The total stress of the thin films (σ_F) is the sum of internal stress (σ_{int}) and the thermal stress (σ_{th}). The thermal stress[4,6,7,8] is the difference between thermal expansion of the film and the substrate. In this case, where the deposition is mostly on silicon substrates and the temperature of deposition is lower than 300°C (without heating), one can neglect this thermal stress[4]. Thus, the estimation of the intrinsic stress films on the measurement of the curvature variation substrate corresponds to the internal stress. Indeed, the substrate deforms depending on the stress. The stress deformation is either tensile or compressive (Figure 2- 9).

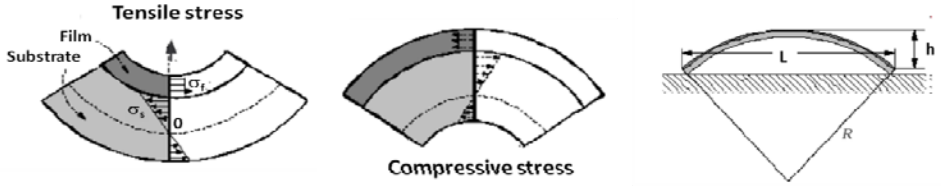

Figure 2- 9: Tensile and compressive stress and method to determine curvature radius[4,6,7,9].

The film stress σ was measured via the stoney relation , which is established by the isotropy conditions of the stress in the plane of the substrate ($\sigma_{xx}=\sigma_{yy}$), using a portion of a sphere radius R (curvature radius) assimilated to the isotropy condition, and to put the other components of the stress tensor equal to zero ($\sigma_{zz}=0$). Further, the film thickness t_F should be lower than the substrate thickness t_s ($t_F << t_s$), which is the conditions[4,6,7,9]:

$$\sigma_F = \sigma_{\text{int}} = \pm \frac{E_s}{6(1-\nu_s)} \frac{t_s^2}{t_F} \left[\frac{1}{R} - \frac{1}{R_0} \right] \qquad (2.2)$$

By convention, the sign "±" corresponds to the tensile stress and compressive stress respectively. ν_s is the Poisson's ratio when the Si substrate is stretched,

of the contraction or transverse strain to the extension or axial strain. E_s is the Young modulus relative to the Si substrate.

The determination of the stress requires knowing the initial curvature radius R_0 of the substrate before deposition. The curvature radius of the Si substrates which are chosen very smooth is estimated and checked to be infinite. The curvature radius before and after deposition is measured using a Dektak3ST surface profiler (Figure 2- 10).

Figure 2- 10: Dektak3ST surface profiler.

2.2.3 Fourier transform infrared spectroscopy (FTIR)

Fourier transform infrared spectroscopy (FTIR) is a non-destructive method, which gives quick information about chemical composition, crystal size using the full width at half maximum (FWHM) and structure of a deposited film. The optical system of the spectrometer used, i.e. a 8700 FT-IR Nicolet, is based on a Michelson interferometer (Figure 2- 11).

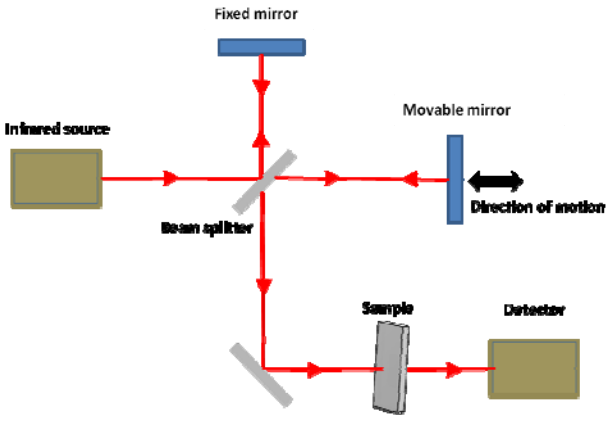

Figure 2- 11: Schematic view of a Michelson interferometer.

A beam splitter divides the output beam from the infrared source into two halfs: one is reflected toward the fixed mirror while the other 50% of the radiation is transmitted towards the movable mirror. Then, they recombine from the perpendicular mirrors "fully silvered" towards the beam splitter giving rise to an interference figure. The motion of the mirror allows modulating an analyzed wavelength. The half of the created output beam is transmitted back to the source and is discarded. While the other half is reflected to a new path toward the sample. The thin films used for this analysis, are deposited on silicon (100) substrates chosen for their transparency for infrared radiations. The interferogram contains informations from the source, the substrate and features of transmission of the deposited film. To discard the components "source" and "substrate" from the interferogram, one achieve a calibration of the apparatus only using a substrate (background) coming from the same wafer used for the substrate on which the film is deposited. The Fourier transform of the final interferogram allows getting the spectral response of the film with different absorption peaks associated to transitions between the energy levels of vibration. The spectral domain covers the mid-infrared region i.e. 4000 cm^{-1} (2.5 µm) to 400 cm^{-1} (25 µm). The best resolution is 2 cm^{-1}, but for practical reasons, one use 8 cm^{-1} for all spectra measured, which is adequate. The measurements are made under nitrogen flush, minimizing the CO_2 absorption peaks at 2360 and 680 cm^{-1}.

The infrared analysis allows determination of the presence of impurities such as hydrogen, oxygen, carbon tabulated in the literature (Table 2- 1). However, for monoatomic solids, such as graphite and diamond, the technique is very sensitive to the presence of defects or impurities in the lattice. FTIR using

normal incidence of the h-BN thin films give only information concerning the transverse optical resonance mode (TO) because the longitudinal optical resonance mode (LO) is not decoupled at normal incidence to be observed (See more details are given in chapter 4). To observe the LO, some modifications need to be made to the experimental set-up. One made a rotative sample holder, with a pitch of 10° from the normal (Figure 2- 12a). One can apprehend better the crystalline structure of films with this technique, i.e. so-called oblique transmission. To deepen the investigation, these measurements which depend of the polarization state of the light, were made using a grid polarizer (Specac) covering the mid-infrared region. The purpose is to discern the component of the electric field parallel to the plane of incidence, termed *p-like* (parallel) and the component perpendicular to this plane termed *s-like* (from *senkrecht*, for perpendicular). These results were compared to the reflective FTIR in quasi-normal incidence and oblique incidence using polarized infrared reflection (PIRR) (Figure 2- 12b).

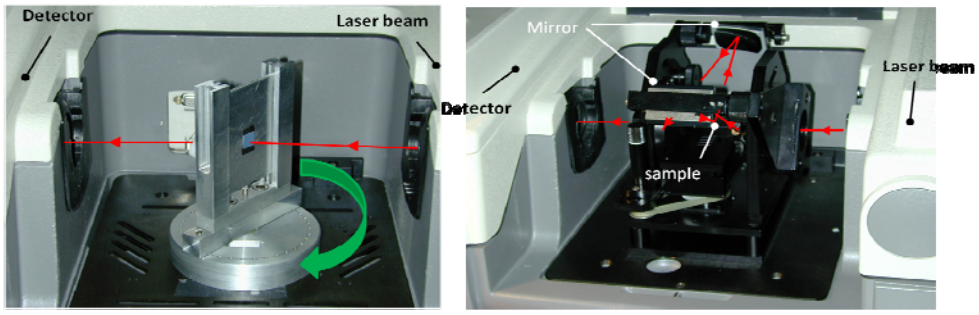

(a) (b)

Figure 2- 12: The homemade rotative sample holder (a). Polarized infrared reflection technique (b)

Group frequency	Band assignment wavenumber (cm^{-1})	Group frequency	Band assignment wavenumber (cm^{-1})
714-719	B-O-B asym./sym. bend	**1380**	**$TO_{\perp}$ (h-BN) in -plane stretching**
780-811	**$TO_{//}$ (h-BN) out-of-plane bending**	**1460**	B-O asym./sym stretch
800	B-O asym./sym . bend	**1500**	C=N/C-C
810	Si-O-Si asym.. /sym. bend	**1550**	NH_3
840-870	N-O	**1587**	B-O asym./sym stretch
880	B-C asym./sym. stretch	**1600**	C=C/C=O
900	N-H, B-H out-of-plane bending	**1700**	B-H-B
1050	SiO_x	**1735-1750**	C=O
1060	Si-O-Si asym. /sym. Stretch, C-H	**2200**	$C \equiv N$ /C-C
1100	B-C, C-N	**1540-2220**	B-H-B
1106	Si-O-Si	**680-2500**	CO_2
1175	C-O-C	**2564**	B-H
1180	B-H in plane bending	**2900**	C-H
1190	B-O-H asym./sym . bending	**3400**	N-H
1350	C-N stretch. ,C-H bend , C-O stretch., N=O sym. stretch.	**3225-3448**	O-H asym./sym stretch

Table 2- 1: Possible attributions of IR absorption peaks[4,10].

2.2.4 Raman Spectroscopy

Raman spectroscopy is a branch of vibration spectroscopy and is complementary to IR absorption spectroscopy[10]. However, the selection rules for Raman spectroscopy differ from those for infrared spectroscopy. Indeed, the fundamental requirement of the matter to be infrared active, leading to absorption of infrared radiation, is that there must be a sharp change in dipole moment during the vibration of the molecule or the functional group to be studied. Whilst, a net change in bond polarizability must be observed for a transition to be Raman active[10,11,12]. Wherefore many transitions are observed in the Raman spectrum and not in the IR spectrum, and vice versa.

Raman scattering is an inelastic light scattering resulting in a shift of the wavelength of the light emitted by the sample. It corresponds to the variation of the polarizability of the crystal by the optical vibration modes[4] (center of the first Brillouin zone, q=0). The shift of the observed frequency between the incident beam frequency and the backscattering frequency coming from the sample is feature from a given pulse and corresponds to the consecutive atomic vibrations. When the incident beam excites a sample, some photons interact with atoms and undergo energetic modifications. One observes different events:

- If photons pass through the sample without any change of the energy (absorption line=emission line), there is Rayleigh scattering (ν_0).
- If there is a modification of the energy, it corresponds to Raman scattering. One observes 2 distinct emissions waves of both sides of the exciting wave, named Stokes (loss energy) and anti-Stokes (gain energy). In the Raman scattering processes, variations of energy are measured in relative distance regarding the exciting wave: It is the Raman shift measured in cm^{-1} units (Figure 2- 13).

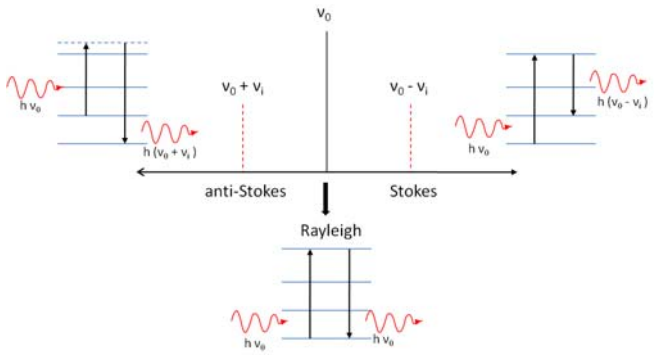

Figure 2- 13: Schematic representation of scattering effects during Raman measurements.

2.2.4.1 Micro-Raman set-up

The use of Raman spectroscopy seems to be mandatory in the case of reduced structures such as thin films. All measurements were made in the "Laboratoire de spectroscopie infrarouge et Raman" (LASIR) at Lille I university under the responsibility of Dr. Ali Soltani. Four different devices were used during this study (Figure 2- 14):

a) Jobin-Yvon (UV HR LabRam) equipped with a confocal microscope, spectrograph (focal 800 mm) and a charged couple device detector (CCD). The system is dedicated to the Ultra-Violet (UV) measurement. Thus, samples are irradiated by a solid state laser at 266 nm via a confocal microscope. Using a long focal length spectrograph coupled to networks with a large number of strokes which can achieve spectral resolutions of about 1.5 cm^{-1} per pixel in the UV. Concerning the UV laser power, it is taken constant at 230 mW. The backscattering signal power coming from the sample is observed with filter (4.3 mW to 9 nW) and without filter (9.6 mW)

corresponding to the area of the sample. The use of UV excitation has several advantages: UV radiation has a low penetration depth in most of materials (tens of nanometers), which significantly reduces the depth of probed matter, confining the obtained information to the surface, which is not the case for visible light, for which materials are often transparent.

b) Microspectrometer XY Dilor (Jobin Yvon Horiba Gr.) coupled with Ar^+ laser Spectra- Physics mod. Stabilite 2017, allowing to record visible spectra with 473 nm (blue) and 532 nm (green). The detection of Raman signal is provided by a CCD Wright camera cooled down by liquid nitrogen. The visible laser power is particularly high and is available at 2 W.

c) Microspectrometer LABRAM Dilor (Jobin Yvon Horiba Gr.) which is coupled with a He-Ne laser at 632.8 nm with maximum power 18 mW. The optical filtering of the Rayleigh line is provided by a "Notch" filter. A motorized platinum XY coupled with a piezo self-focus device in Z direction allows a point to point axial resolution of 1 to 2 μm. Spex CCD detector (2048 pixels X 512 pixels) type lit from the front, cooled with nitrogen, is well suited for long acquisitions.

d) Microspectrometer HoloLab Series 5000 (Kaiser Optical Systems). It is coupled to a near infrared diode laser which emits at 785 nm with a nominal power of 400 mW. The optical filtering of the Rayleigh line is provided by "Notch" filters. The CCD detector (Andor, 1024 x 128) type "deep depletion" backlit is optimized for the near infrared. All laser-microscope-spectrometer are connected by fiber optics. A motorized XYZ stage can record a point to point resolution of 0.1 microns controlled by the software "HoloMap" under Matlab v6.5.

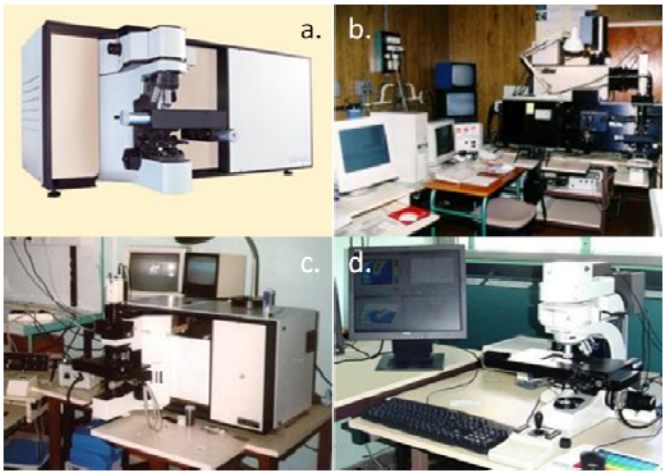

Figure 2- 14: Picture corresponding respectively to the micro-Raman set-ups with UV (a), Blue-Green (b), Red (c) and near infrared (d) incident laser wavelength, used in this study and describe above.

2.2.5 Ultraviolet-Visible spectroscopy (UV-Vis)

Films were deposited on substrates like fused silica or quartz, which are transparent in the wavelength range (175-900 nm) corresponding to the UV-Visible domain studied.

The measurement of UV-Vis transmission spectra depending on photon energy ($h\nu$), allow evaluating optical constants of h-BN thin films and their band gap. Indeed, the absorption coefficient α for thin films with thickness t is related to the transmittance T by the relation:

$$T = e^{-\alpha t} \qquad (2.3)$$

The relation remains correct if multiple reflections in the layer are neglected. It constitutes an easy way to determine qualitatively optical properties of films, and to evaluate optical band gap.

In order to get a better accuracy on optical properties of thin films, an easy method to determine thickness and optical constant were proposed by R. Swanepoel[13,14]. This method requires to build numerically 2 functions T_{max} and T_{min} as an envelope of the experimental data. The interferences generated from

2 distinct interfaces (Air/film) and (film/Substrate) leads to the refractive index n, absorption coefficient k and thickness t.

2.2.5.1 Description UV-Vis spectrometer

Measurements were achieved on a single beam Cary 500 UV-VIS-NIR (Ultra violet– visible-near infrared) spectrometer in the wavelength range (175-3300 nm) which was equipped with the software Cary winUV Scan application (version 3.00). The basic parts of the spectrometer are two light sources: The deuterium lamp is used in the region 160-380 nm while higher wavelengths are emitted with the halogen lamp. An optical system in the monochromator converts the diverging light of the source to collimated light. When a sample of h-BN/fused silica is exposed to light, certain functional groups within the film absorb light of different wavelengths in the UV or visible or NIR region while the passing light, then is collected by the PbS (Lead(II) sulfide) photodiode detector, which is thermoelectrically (Peltier element) cooled to 0°C to reduce photometric noise. UV-VIS-NIR spectroscopy is used for qualitative and quantitative analysis of materials.

2.2.5.2 Procedure

All measurements are made in the wavelength range (3300-175 nm):

1. Use scan without sample to check 100% transmission
2. Use scan with only fused silica or quartz substrate
3. Measure h-BN on fused silica or quartz

2.2.6 X-Ray diffraction (XRD)

To perform the structural characterization of a crystalline material, X-ray diffraction (XRD) is used under well-defined conditions.

2.2.6.1 Conditions

Samples were measured on 2x2 cm^2 substrates size with film thicknesses higher than 1 µm in order to reduce the edge effect at grazing angles and the influence of the substrate, respectively. All measurements were made with a step size of 0.04°/min (0.02°/min by the source motion and 0.02°/min by motion of the detector) starting at 2θ from 10° to 140° (θ-2θ coupled mode).

2.2.6.2 XRD diffractometer

The XRD measurements are performed with a Bruker D8 discover diffractometer with a Θ-Θ goniometer whose sample holder is fixed, while the X-ray source and the detector, are both rotated at the same Θ-2Θ coupled mode angle (Figure 2-15). The system works in parallel beam geometry by using a Göbel Mirror for Cu radiation as a line focus, mostly Cu $K_{\alpha 1}$, $K_{\alpha 2}$ and K_{β} rays. The X-rays are measured by a "lynx eye" position sensitive detector. This 1D detector has 192 separate channels of compound silicon strip which all act as single detectors.

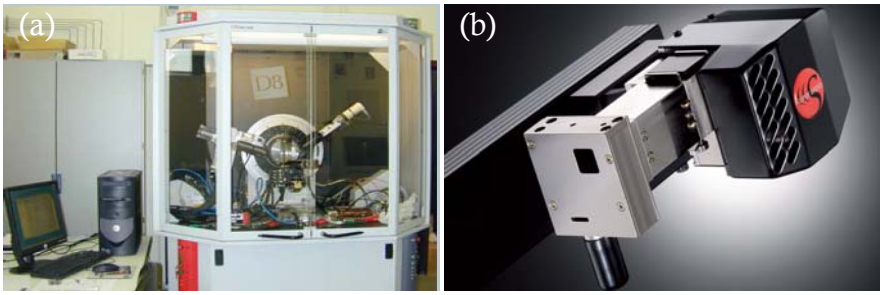

Figure 2- 15: X-Ray Diffractometer BRUKER D8 Discover (a) and lynx eye position sensitive counter detector (b).

2.2.7 X-ray Photo emission Spectroscopy (XPS)

2.2.7.1 Description

X-ray photoemission spectroscopy (XPS) is a quantitative and non-destructive technique. This technique measures the chemical composition (binding energy) of the elements that exist within a material. The phenomenological aspect of the XPS technique is described by the Spicer model (Figure 2- 16a). Three steps are needed: the photo-excitation of an electron from its binding level towards an empty level leading to the photoionisation. The cross section σ[15,16] describes the probability of the process. Then, the transfer of the electron to the surface leading to the determination of the mean free path[17], without inelastic interaction (1), after inelastic interaction (e/e, e/plasmon) (2), and after several randomly inelastic shocks. To reach the surface of the detector and therefore to be detected, ultra high vacuum (UHV) is needed ($p<6.6x10^{-8}$ mbar) in the analysis chamber[18,19]. Figure 2- 16b, shows the attribution of each peak encountered in XPS spectra. The principle is to irradiate the sample by

monoenergetic X-rays extracted from material (Aluminium or Manganese), then to collect ejected electrons from the sample by isolating each corresponding kinetic energy (Figure 2- 16c). By measuring the kinetic energy of photoelectrons, it's easy to highlight these elements. Indeed, the binding energy E_B of electrons and therefore the kinetic energy E_K due to the relationship when the sample is in electrical contact with the spectrometer:

$$E_B = h\nu - E_K^{'} - \phi_{sample} = h\nu - E_K^{''} - \phi_{spectrometer} \qquad (2.4)$$

Where $E_K^{'} = E_K + \phi_{sample}$ and $E_K^{''} = E_K + \phi_{spectrometer}$, with ϕ_{sample} and $\phi_{spectrometer}$ correspond to the working function of sample and spectrometer, respectively.

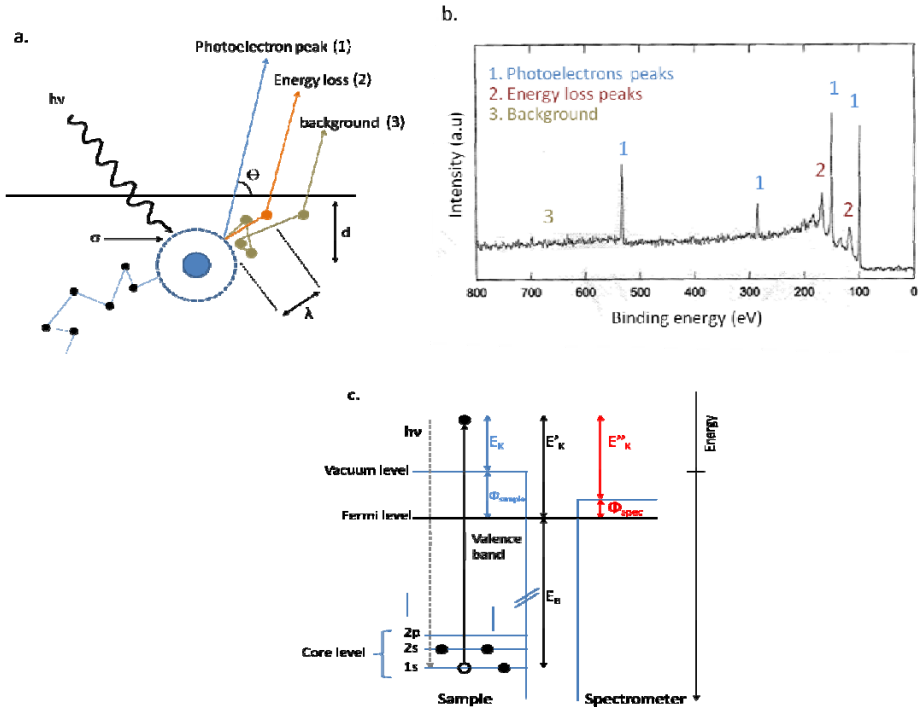

Figure 2- 16: Phenomenological aspect: processes of photoelectron-solid interaction near surface (Spicer model)[15,16,17,18,19] (a) and its schematic representation[15] (b).Principle of XPS measurements[15] (c)

2.2.7.2 XPS spectrometer

The analysis of (BN/Si) films with this technique was performed by M. Saitner, under the responsibility of the copromotor prof. dr. Hans-Gerd Boyen. All photoemission spectra were measured using a commercial photoemission system (Physical Electronics PHI 5600 LS). Core-level spectra were acquired by XPS using Al K_q X-rays (1486.60 eV) for analysis of the chemical state of the samples. The spot size of the X-ray beam was 1.1 mm and the overall energy-resolution is smaller than 0.4 eV (FWHM). The binding energy scale was calibrated by means of an independent Au reference sample, setting the Au-$4f_{7/2}$ core-level position to 84.00 eV.

2.2.7.3 Condition

As we know, XPS is a surface characterization technique with a depth penetration around 5 nm. Therefore, some samples were prepared with a maximum thickness of 200 nm on a 1x1 cm^2 Si (100) substrate, enough for this study and compatible with other characterization techniques such as EDS and RBS described further.

2.2.8 Energy dispersive X-ray spectroscopy (EDS)

The chemical composition is evaluated in a qualitative way with the EDAX DX4 energy dispersive X-ray spectroscopy (EDX) technique attached to the FESEM (See section 2.3.1).This technique is a non-destructive technique that allows to identify elements present in the bulk of the film and to quantify their chemical information. EDX technique measures the energy of the X-rays emitted after irradiation of the sample by a high energetic electron beam. The EDX are a standardless technique. This means that a rough estimation of the B_xN_y concentrations is determined via the B/N peak height ratio's.

For all the measurements, an accelerating voltage of 5 kV has been used so that a similar background can be assumed for the EDX spectra. Nevertheless, the charging effects being sometimes important, the peak ratio's could be changed due to other effective accelerating voltage. Depending on the density of the material under study, the information depth Z_m (µm) that is probed varies between 0.3 and 1.0 µm.

$$Z_m = 0.033 \times \frac{E_0^2 - E_c^2}{\rho} \qquad (2.5)$$

Where E_0 is an accelerating voltage of impinging electron beam (=5 kV). E_c is excitation energy of X-ray to be measured (kV). E_c for $B_{K\alpha}$ and $N_{K\alpha}$ is 0.183 keV and 0.392 keV, respectively. ρ is the density in g/cm^3.

An external reference sample as the stoichiometric h-BN target was measured and its peak height ratio is compared with peak height ratio from all samples at same conditions.

2.2.9 Rutherford backscattering spectroscopy (RBS)

The stoichiometry and the product of t.ρ is detectable (thickness t evaluated from a SEM measurement), determined by Rutherford backscattering spectroscopy (RBS -HVEE tandetron) at Jena university (Germany) by C. Borschel under the responsibility of prof. dr. Carsten Ronning (Figure 2-17).

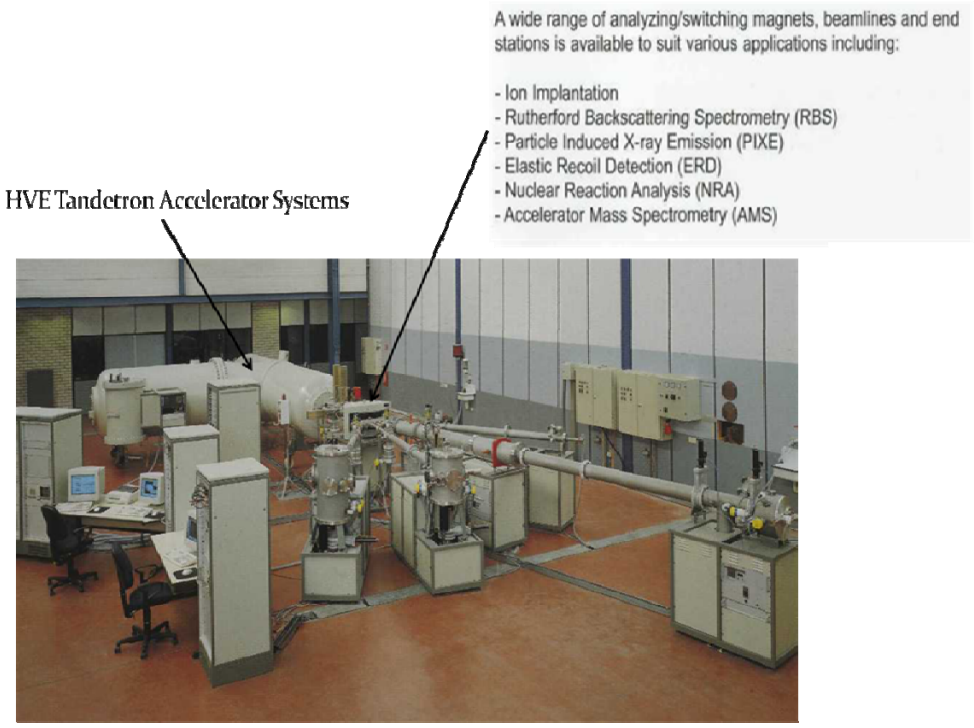

Figure 2-17: Photograph of variable spectroscopy applications, including RBS at Institute for Solid State Physics (University of Jena).

Rutherford Backscattering Spectroscopy (RBS) belongs to a versatile set of non-destructive methods for depth profiling, which allows to identify atoms present in the bulk of the film (Figure 2- 18a).

RBS has the advantage that it can in principle measure absolute atomic concentrations without the need of a standard sample. The high energy resolution of the detector is 16-17 keV (FWHM).

However, an ion accelerator is required and RBS is not really suited for light elements as boron (B). The sensitivity of B detection is related to the He ion energy. Indeed, the He ions with a initial energy of 1.4 MeV or 4.22 MeV lose energy while travelling through the matter, which provides the depth information.

One of the drawbacks is that RBS cannot distinguish between a rough surface and a rough interface because depths are measured from the surface and all depths are averaged over the beam spot (1mm^2).

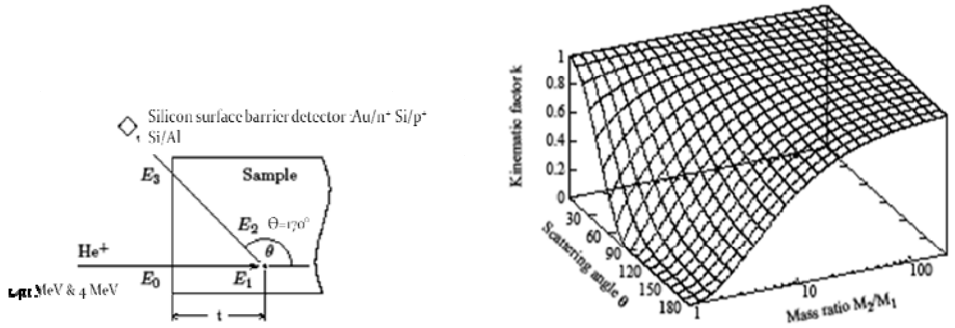

(a) (b)

Figure 2- 18: Schematic representation of a RBS measurement. A beam of He ions impinges on the sample. The energy of the ions that leave the sample under a certain angle is detected[20]. (a) Kinematic factor k, plotted as a function of scattering angle Θ and mass ratio M_2/M_1. (b).

Due to their little dependence on the scattering angle, it can be observed that the mass resolution is better for large scattering angles close to 180° (Figure 2-18b). Additionally, the kinematic factor k which denotes the ratio of energies after and before the collision, is determined by the conservation of energy and conservation of momentum. It can still be assumed to be constant for that solid angle, wherefore most RBS measurements are done with large backscattering angles.

$$k = \frac{E_1}{E_0} = \left(\frac{\sqrt{1 - \left(\frac{M_1}{M_2}\right)^2 .\sin^2\theta} + \left(\frac{M_1}{M_2}\right)^2 .\cos^2\theta}{1 + \left(\frac{M_1}{M_2}\right)} \right) \approx \left(\frac{M_2 - M_1}{M_2 + M_1} \right)^2 \qquad (2.6)$$

Where M_1= 4 g.mol^{-1} is the molecular mass of helium (He), M_2 is the molecular mass of either boron (B) or nitrogen (N) met in the path of the He ion, and θ is scattering angle in the laboratory frame of reference. E_0 is the He^+ ion energy and E_1 is the He ion energy passing through the BN film before the collision with B or N nucleus (see Figure 2- 18a).

2.2.9.1 Kinetic Energy (X scale)

The purpose is to determine the kinetic energy corresponding to the X scale in the RBS spectra. The He^+ ion loses energy passing through the BN film into the target (B or N nucleus) using the eq.2.7.

$$E_1 = E_0 - t.\left(\frac{dE}{dx}\right)_{E_0} \qquad (2.7)$$

Where t is the thickness. Then, the He^+ ion transfers energy and momentum to the target (B or N nucleus) using the kinematic factor k (eq. 2.8).

$$E_2 = k.E_1 \qquad (2.8)$$

On the way out, the He^+ ion loses energy again, but the path length is now increased by $1/(\cos\theta)$ in the eq.2.9.

$$E_3 = E_2 - \frac{t}{\cos\theta}\cdot\left(\frac{dE}{dx}\right)_{E_2} \qquad (2.9)$$

2.2.9.2 Backscattering yield (Y scale)

The purpose is to determine the backscattering yield corresponding to the Y scale in the RBS spectra. For two positively charged particles, the repulsive potential is the Coulomb potential. The differential scattering cross section (σ) for this potential is given by the Rutherford formula:

$$\frac{d\sigma}{d\Omega} = \left(\frac{Z_1 Z_2 e^2}{16\pi\varepsilon_0 E_K}\right)^2 \cdot \frac{1}{\sin^4\frac{\theta_K}{2}} \approx \frac{Z^2}{E_K^2} \qquad (2.10)$$

$$Y \propto n(i,t).\frac{d\sigma}{d\Omega}(E_1; Z_2; \theta) \qquad (2.11)$$

Where Z_1 and Z_2 are the proton numbers of projectile (He^+ ions) and target, respectively, and E_k is the projectile's energy. Y is the backscattering Yield corresponding to the number of ions backscattered.

To interpret the results, simulation used a Nuclear Data Furnace[21] code (NDF), which is commercially available. The simulation is made including homogeneous deposition of each component which is expected to be present in the films i.e. B, N, O, C, and Ar. Four parameters are modified: the solid angle, offset, thickness and density. The solid angle and offset are used to adjust the simulation to the experimental data for different He^+ ion energy.

The most important parameter is the atomic density N(at/cm^3) and layer thickness z(cm). The relationship between N and z is a constant and is given by eq. 2.12:

$$N \cdot z = 1100 \cdot 10^{15}\ at/cm^2 \qquad (2.12)$$

Where the constant is determined by NDF. Hence, the mass density ρ (g/cm^3) is determined by the relation below:

$$\rho = \frac{1}{2\mathfrak{N}} \cdot N \cdot M \qquad (2.13)$$

Where $\mathfrak{N}$ (Avogadro's number) = $6{,}022.10^{23}$ at/ mol,

and M (BN) = M (B) +M (N) = 10,8+14= 24,8 g/mol.

2.3 Characterization techniques: Microscopic imaging

2.3.1 Field emission Scanning Electron Microscopy (FE SEM)

The uniformity and morphology of the deposits was observed using a field-emission scanning electron microscope (FESEM-FEI Quanta 200F). The electrons are generated by a field emission gun and are focused onto the sample by a set of electromagnetic lenses. Several parameters such as the accelerating voltage, and the spot size influence the SEM performance. A small sized beam of electrons in the range of several scans the sample surface, while the electron-sample interactions are analyzed by several detectors. Electron-sample interactions are quite diverse due to the elastic and inelastic scattering processes of the primary electron. Thus, the kinetic energy of the primary electron are mostly transferred into heat whereas a part of energy leaving the sample, could be emitted into multitude of signals as X-rays, CL, light (UV-Vis-IR), secondary electrons (SE) and backscattered electrons (BSE). However for the imaging in SEM, the emission of secondary electrons and the backscattering of the primary electrons are the most important processes, and these images will be used in this thesis. Secondary electrons (SE) generated within a shallow depth profile (energy loss around 10 eV) below the specimen surface can escape the specimen and reach the detector. They are mostly used to reveal the surface morphology of the sample and are detected by an Everhart-Thorton Detector (ETD) in high vacuum. To determine the thickness, the cross-sectional SEM measurement is performed using a solid state backscattering detector (SSD). SSD is preferred to ETD due to the contrast of charge density between h-BN layer and Si (100) substrate. Here, all surface images were performed with the accelerating voltage of 15 kV, corresponding to a penetration depth in the order of several microns, WD taken constant as 10 mm, with the magnification ranging between 2500 to 80000 times using the ETD detector. Idem for the cross section imaging, except for the different magnification is in combination with the SSD detector (not shown in this thesis).

After the EDX measurements to take SEM images, all samples were covered with a few nanometers of conductive layer (carbon layer) in order to suppress the drift of the electron beam, due to the electro charging effect on insulating h-BN samples.

2.3.2 Transmission electron microscopy (TEM)

2.3.2.1 TEM preparation

The cross sectional TEM preparation was performed at « Institut d'Electronique, de Microélectronique et de Nanotechnologie (IEMN) » under the responsibility of Dr. Ali Soltani, using a focused ion beam (FIB).

A metal (platinum or/and tungsten) line is ion beam deposited on the area of interest to prevent damage and spurious sputtering of the top portion of the specimen and to also delineate the location of the area of interest. Typical dimensions of the metal line are 3 µm wide × 3 µm high × 30 µm long. Large trenches are sputtered on either side of the area of interest using a high Ga^+ beam current (7nA at 30kV) with a tilt of ± 20°.The beam current is reduced at 1nA to dissociate the foil from the substrate at tilt of 52°. Tungsten tip micromanipulator is used to lift out the foil inside the vacuum chamber and stick the foil on a specific TEM grid with ion beam platinum deposition for TEM measurements. Milling at 1nA is performed on alternate sides of the foil until 150 nm thickness or less (the final thickness of the specimen will depend on the information sought and the density of the material(s)). Final smooth milling is realized at 5kV and 1nA to minimize the amorphous material thickness at each side of the foil due to Ga^+ implantation.

2.3.2.2 TEM measurement

The cross sectional TEM measurement was performed with a FEI TECNAI SPIRIT transmission electron microscopy at an accelerating voltage of 120 kV at IMO under the responsibility of Dr. Jan d'Haen. Bright field images, dark field images from a selected area electron diffraction pattern (SAED) and convergent beam electron diffraction (CBED) images were explored on samples grown with 5 % H_2 (See chapter 3, Figure 3-15). This technique is preferred to other techniques to measure the thickness of "nanowalls or platelets" and to highlight the (002) axe orientation.

2.3.3 Atomic Force Microscopy (AFM)

The atomic force microscope (AFM) belongs to the "scanning probe" instruments. It's a method of measuring topography with a very high resolution

at the same time leaving the surface undamaged. One used the Veeco multimode microscope equipped with the Digital Instruments Nanoscope IIIa (Figure 2- 19a) controller and the quadrex module. The Z-resolution scale is around 1 Å while the 2D-resolution is around 1 nm. These measurements were done in tapping mode in air. The tip has a specified radius of curvature smaller than 10 nm, a spring constant around 42N/m and a resonance frequency around 330 kHz. The tip that probes the surface is fixed at the end of a cantilever made in silicon (Si) or silicon carbide (SiC) with a lower spring constant (0.07 to 0.31 N/m). The degree of freedom of the tip is controlled by a piezoelectric ceramic, which can move in response to an applied voltage. XY piezo leads to the scan of the surface while Z-piezo is kept constant. When the tip scans the surface, the latter interacts with atomic forces (Van der Waals) leading to the deflection of the cantilever in the Z direction. A laser beam is directed on the cantilever (Figure 2- 19b). The deflection of the latter is observed by a sensitive photodiode detector. By adjusting the height (Z dimension) of the probe support, the electronic interface unit (EIU) keeps the force between the tip and the surface constant. The correction signal (mechanical-electrical converter) leads to the formation of the AFM images (Figure 2- 19c).

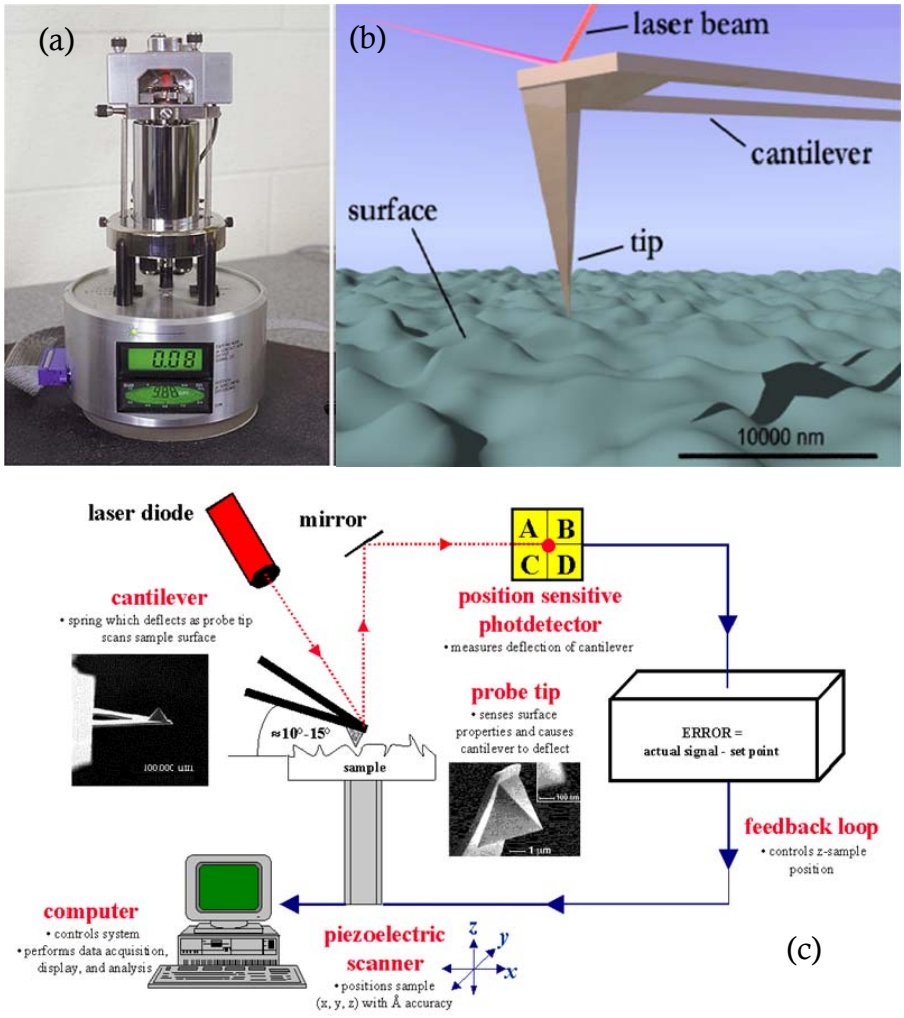

Figure 2- 19: Digital Instruments Nanoscope IIITM Multimode Scanning Probe Microscope, in combination with the atomic force probe (IMO) (a). Illustrations of atomic force microscopy, using an optical cantilever[22](b). A sketch of the atomic force microscopy setup[23] (c).

2.3.4 Cathodoluminescence (CL)

The nano-cathodoluminescence (CL) experiment is performed at 10 K using a 5 keV, 4 nm diameter electron beam on a sample deposited with 5 % H_2. This sample is prepared as a foil by focused ion beam and stuck on a TEM grid with ion beam platinum deposition. The CL signal is collected with a UV monochromator from Horiba Jobin Yvon installed on a high spatial resolution JEOL7001F FEG-SEM. A CCD camera is used to record spectra dispersed by a 600 grooves/mm grating giving a spectral resolution of 0.5 nm for a 0.15 mm slit aperture. A photomultiplier is synchronized with the beam scanning to acquire monochromatic CL images. These spectra were measured in ″Groupe d'Etude de la Matière Condensée ″ (GeMaC) at CNRS-Université de Versailles Saint-Quentin-en-Yvelines under the responsability of Dr. Julien Barjon.

2.4 Other techniques

2.4.1 Specular reflectance technique

The refractive index of the h-BN samples was measured by a LAMBDA 900 Perkin Elmer beam spectrometer equipped with a specular reflectance module with a 6° fixed angle for reflectance spectra (chap 5, figure 5-1)

To have an estimation of the porous character of h-BN films, a fit to the experimental reflectance spectrum is performed to determine the optical thickness by evaluating the beat of the interference fringes. This adjustment is made using the transfer matrix formalism and the Bruggeman model[24, 25].

2.4.2 m-lines technique

The m-lines technique (also referred to as the prism coupler technique) is commonly used to determine the effective refractive index n_{eff} of thin films. It estimates the particular angle allowing the propagation of a He-Ne laser beam (at 633 nm) within a planar waveguide (thin film) by coupling the evanescent wave obtained to the basis of a prism with a high refractive index.

This measurement is performed as follows: a Rutile (TiO2) coupling prism is pressed onto the waveguide (Figure 2- 20). A laser beam is then coupled into the prism so that total reflection occurs inside the prism at the interface to the

waveguide. In the vicinity of the waveguide the overlapping incident and reflected beam generate a standing wave. The evanescent field of that standing wave penetrates into the waveguide[26]. It appears that the response of the laser beam (at 633 nm) depends on the wave polarization state whether it is a transverse electric (TE) or transverse magnetic (TM) plane waves. Any arbitrary plane wave can be described as a combination of TE and TM wave.

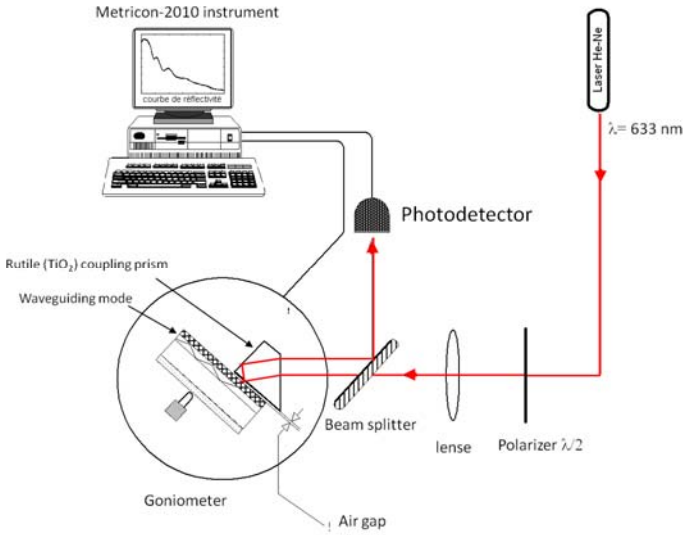

Figure 2- 20: Schematic representation of the m-lines setup.

2.4.3 Contact angle measurement

A contact angle (CA) measuring device, e.g. SCA20, is an instrument which performs an automatic measurement of the wetting behavior of dionized (DI) water on solids surfaces. It allows but not always the estimation of the super-repellent (hydrophobicity) features of the h-BN nanowalls.

2.4.4 Confocal imaging

Confocal experiments are performed on a Zeiss LSM 510 META one-photon CLSM (Jena, Germany) equipped with a new 30 mW air cooled argon ion laser, which was set at 45% of its maximum power (this corresponds to a tube current

of 5.7 A). The Alexa fluorophores on the 8 bp DNA strands were excited with a 488 nm line laser under the control of an acoustic optical tuneable filter (AOTF). After passing a 0.6 neutral density filter (25% transmittance), the excitation light was directed to the sample via a dichroic mirror (DC; HFT 488) and a Zeiss EC Plan-Neofluar 410x objective. The fluorescence collected by the objective was transmitted through the DC and a 505 nm LP emission filter to a photomultiplier tube. Images were acquired with the 4.0 version of the Zeiss software. A photomultiplicateur cell was positioned in a translation stage and focus in order to have the region of interest well centered. The zoom factor was set to 4 (104.9 nm/pixel). A photomultiplier tube (PMT) gain and signal amplification were adapted in order to have a sufficiently high signal to noise ratio. The detection pinhole diameter was set to 1 airy unit (66 µm diameter), which in these conditions corresponds to an optical slice <0.9 µm, to reduce the contribution of the solution as much as possible.

2.4.5 SQUID technique

This study was performed in the Laboratory of Materials for Nanosystems and Bio-interfaces in Prague (Czech Republic) under the supervision of Dr. Jana Poltierova Vejpravova.

A superconducting quantum interference device (SQUID) is the most sensitive available device for measuring magnetic fields and it was used on h-BN granular structure and h-BN nanowalls structure samples.

SQUID magnetometer, MPMS 7XL by Quantum Design RSO mode, is used to characterize the h-BN materials on Si with 0 % H_2 (granular structure) and with 5 % H_2 (nanowall structure). The sample areas are 5 x 5 mm^2.

2.5 References

1. "Introduction to Glow Discharges". http://www.glow-discharge.com

2. A. Bogaerts, E. Neyts, R. Gijbels, J. van der Mullen, *Spectrochim. Acta B* **2002**, 57, 609.

3. R. Redmer, *Phys. Reports* **1997**, 282, 35.

4. A. Soltani, PhD thesis « Croissance de films minces de nitrure de bore hexagonal et cubique par depot chimique en phase vapeur assisté par plasma :Caracterisations optiques et électriques » Université de Metz (**2001**).

5. D.M. Mattox, Growth and Growth-Related Properties of Films Formed by Physical Vapor Deposition, ASM Handbook, Surface Engeneering ASM (**1998**).

6. V. Mortet, PhD thesis « Croissance et caractérisation de couches minces de nitrure d'aluminium et de nitrure de bore cubique obtenues par pulvérisation triode » Université de Valenciennes et du Hainaut Cambrésis (**2001**).

7. A. Bosseboeuf, PhD thesis Université de Paris-Sud, Orsay (**1985**)

8. M. Ben el Mekki, M.A. Djouadi, E. Guiot, V. Mortet, J. Pascallon, V. Stambouli, D. Bouchier, N. Mestres, G. Nouet, *Surf. Coat. Technol.* **1999**, 93, 116.

9. M.A. Djouadi, PhD thesis Université Paris-Sud, Orsay (**1995**)

10. J. Coates "Interpretation of Infrared Spectra, A Practical Approach" in Encyclopedia of Analytical Chemistry **2000**, R.A. Meyers (Ed.) Copyright © John Wiley & Sons Ltd, pp 10815.

11. P. Gans, Vibrating Molecules: an Introduction to the Interpretation of Infrared and Raman Spectra, Chapman & Hall, London, **1975**.

12. J.M. Hollas, Modern Spectroscopy, 3 rd edition, John Wiley & Sons, New York, **1996**.

13. R. Swanepoel, *J. Phys. E: Sci. Instrum.* **1983**, 16, 1214.

14. R. Swanepoel, J. *Phys. E: Sci. Instrum.* **1984**, 17, 896.

15. D. Briggs, M. P. Seah, Handbook of Practical Analysis by Auger and X-ray Photoelectron Spectroscopy, Wiley, **1983**.

16. B. Agius, M. Froment, Surfaces, Interfaces et Films Minces, Dunot, Paris, **1990**.

17. J. Als-Nielsen, D. McMorrow, Handbook "element of Modern X-ray Physics", John Wiley and Sons Ltd (**2001**)

18. D.M. Hoffman, B. Singh, J.H. Thomas, Handbook of vacuum science & Technology, Academic Press, **1998**.

19. J. Leclerc, Technique du vide, introduction (BM-4000), Technique de l'Ingénieur, Traité Génie Mécanique **1997**.

20. C.M. Borschel, Analysis of Thin Film Interfaces using High Resolution Rutherford Backscattering Spectrometry, diplomarbeit (**2008**).

21. N.P. Barradas, C. Jeynes, R.P. Webb, *Appl. Phys. Lett.* **1997**, 71, 291.

22. A. Siber, a schematic 3D description of an atomic force microscope (AFM), Institute of Physics Zagreb. http://www.nanotech-now.com/Art_Gallery/antonio-siber.htm

23. http://aqnmol.kw.ac.kr/RESEARCH.html

24. D. E. Aspnes, *Thin Solid Films* **1982**, 89, 249.

25. W. Theiss, *Surf. Sci. Reports* **1997**, 29, 91.

26. http://www.metricon.com/basic.html

Chapter 3 h-BN (NWs) deposition and structural properties

The main goal of this chapter is to discuss the experimental parameters used to deposit hexagonal boron nitride thin films. In the second part, the influence of these parameters on the structural properties is discussed.

3.1. Parameter space

Table 3-1 indicates the most important parameters to adjust and their range of values used.

RF power (13.56 MHz)	50-300 W
Total Gas flow ($Ar/N_2/H_2$) (sccm)	0-69.5/0-50/0-100
Distance target-substrate (cm)	4-8
Working pressure (mbar)	$9.1x10^{-3}$ – $3.3x10^{-1}$
Substrate temperature (°C)	100-600

Table 3-1: General parameters of RF sputtering magnetron system used to control the deposition.

3.2. Parameter steps and their improvement

In order to see the influence of these parameters to reach a good quality of films, some examples of parameter steps will be given. Then, to obtain the h-BN phase, improvement steps to the parameters will be following.

3.2.1 Preliminary experiments

Here, all films were deposited on silicon Si (100) substrates. In order to optimize the growth rate the nitrogen (N_2) gas flow relative to argon (Ar) was varied.

After several experiments, three different set of gas compositions, so-called merely 1, 2, 3 will be described in more detail (Table 3- 2).Two series of film thickness were performed to be studied by different characterization techniques as XPS (200 nm) and FTIR (200 nm and 2 µm).

area of samples	Gas composition included in the respective areas	Working pressure (mbar)	RF power supply (W)	Substrate temperature (°C)	Distance target-substrate (cm)	Thickness
1	90% Ar 10% N_2	$1.2x10^{-2}$	300	155	5	2 µm 200 nm
2	60% Ar 40% N_2					
3	20% Ar 80% N_2					

Table 3- 2: Growth conditions and thickness related.

The total working pressure remains constant ($1.2x10^{-2}$ mbar), and only the partial pressure varies when the gas composition varies (% Ar, % N_2). Different tests were performed at different working pressure. Noteworthy is that plasma is triggered at pressure $\neq 1.2x10^{-2}$ mbar is not stabilized during the deposition process. I put forward the hypothesis that a threshold of gas flow to create the plasma is related to the gas flow pumped into the deposition chamber. The threshold of gas flow is $1.2x\ 10^{-2}$ mbar.

As shown in Figure 3- 1, three area were spitted in accordance with the B/N height ratio determined by EDX and normalized by the stoichiometric h-BN target height ratio. The working pressure for different points is $1.2x10^{-2}$ mbar. The thickness of films grown at different N_2 gas flow is measured by FESEM.

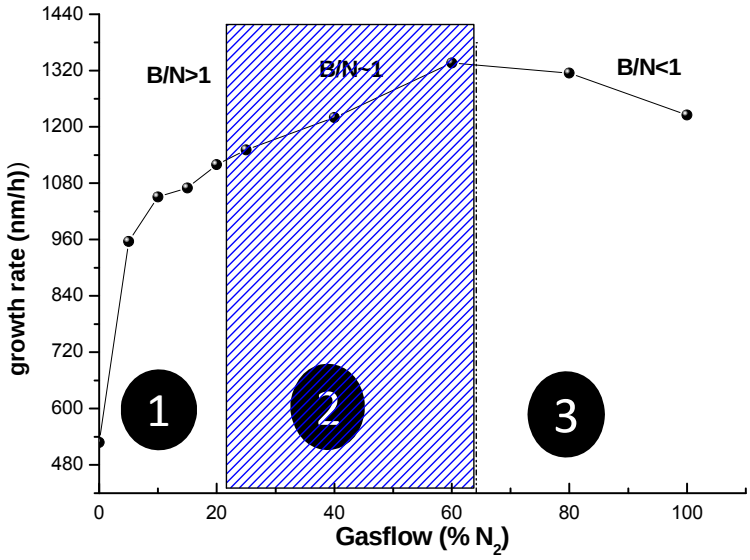

Figure 3- 1: Graph of BN/Si growth rate in function of N_2 gas flow at 300W RF power.

B/N height ratio informs about the non-stoichiometric samples grown without N_2. Moreover, the growth rate is varying. To get stoichiometric films, the growth rate must be constant. For this N_2 was added to the Ar plasma.

- Area 1: too low N_2 content to compensate for decreased B/N in plasma. BN films with an excess of boron lead to their instability (Figure 3- 2a). Besides, these films were totally delaminated and dissolved in water. Huge amount of C and O contaminant contents and cracks are present.
- Area 2: BN films, (Figure 3- 2b) with a reduction of C and O contamination content, but still instable in atmosphere.
- Area 3: too high N_2 content to compensate for decreased B/N in plasma. BN with an excess of nitrogen leads to their instability (Figure 3- 2c). Besides, these films were totally delaminated and dissolved on water.

In summary, according to the Figure 3- 1, all films lead to instable films. Nevertheless, the amount of N_2 gas flow added to the plasma between 20% to 60% leads almost to a stable growth rate. Sputtering the target causes the release of the charged ions, neutral clusters, and other elements. In the plasma, undissociated clusters are likely falling down on the substrate due to the gravity

force. The ionized atoms are influenced by the electrical field that directs them (B-) into the substrates and towards the target (N+). Boron and nitrogen have a high electronegativity difference. This means that they could react easily with each other in the plasma or on the substrate surface. Depending on the deposition condition, a turbostratic boron nitride (t-BN) or a h-BN structure is formed. That should be referred to the plasma chemistry. After a certain time on air atmosphere corresponding to the time before the SEM measurement, some cracks appear on films leading to the total delaminations of films from area 1, 2 and 3.

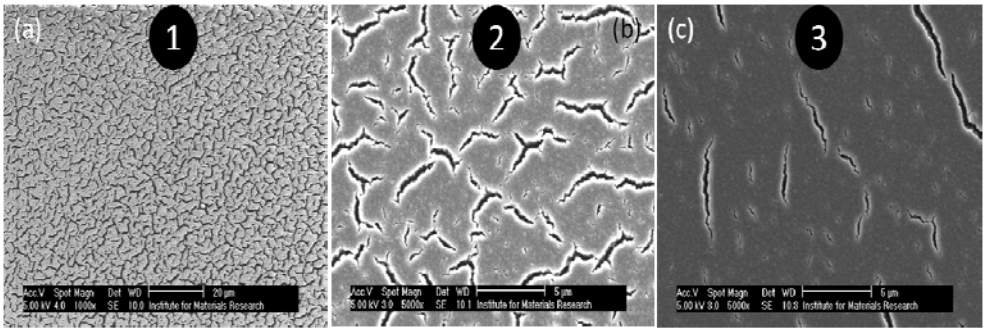

Figure 3- 2: Boron nitride on silicon grown with 90% Ar, 10% N_2 (a) 60% Ar, 40% N_2 (b) and 20% Ar, 80% N_2 (c).

Note that the presence of important C, O and F (between 0.4 and 1.2%) contaminants shown in EDX spectra (Figure 3- 3a) and XPS spectra (Figure 3- 3b), respectively reveal the worst quality of films. Some modification in the deposition system will be performed afterwards (see 3.2.2).

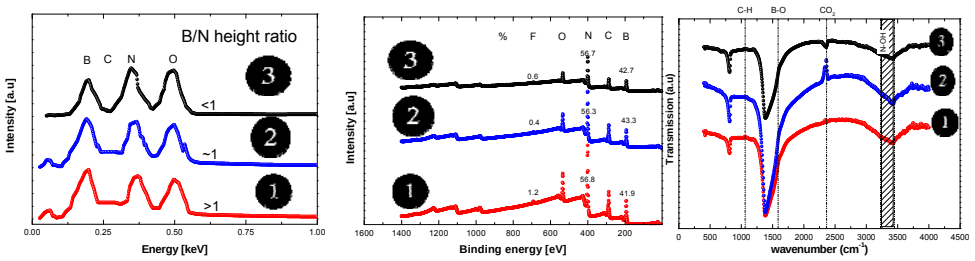

(a) (b) (c)

Figure 3- 3: 2 µm thick films from type 1, 2, 3 conditions, measured by EDS (a), XPS (b) and FTIR (c).

Infrared (IR) spectra shown in Figure 3- 3c reveal the presence of different mixture composition corresponding to the different films. Indeed, a broad band appears between 3200-3445 cm^{-1} which could be assigned to hydroxyl compounds (N-OH). The presence of this normal mode is due to instabilities of the films exposed to the atmosphere[1]. The shoulder observed at 2300 cm^{-1} corresponds to the presence of CO_2 inside the FTIR measurement chamber and not in the BN/Si films. Moreover, one observes peaks at 1060 cm^{-1} corresponding to the C-H group and 1587 cm^{-1} as an absorption band. Indeed, chemical bonds such as N-O, B-C, N-H, C-H, C-O, B-N, B-O..., have an absorption located between 1250 cm^{-1} and 1600 cm^{-1}. Akkerman et al.[2], from annealing experiments of h-BN, have concluded that this absorption band points either to the dehydrogenation of films or a crystalline rearrangement. Besides, this absorption was assigned to the existence of a tetrahedral structure, named x-BN in accordance with the work of Kuhr et al.[3]. Here, the low temperature of the substrate (150°C-160°C) indicated by a temperature read-out unit, leads probably to a poor dissociation rate of the complex mixture of B, N with C, H, O contaminants coming from air and water presence into the plasma. It would be difficult to determine clearly the presence or not in films of one or the other one bond. These bonds could explain the asymmetric growth of the absorption band at 1380 cm-1, more pronounced in the case of thick films (Figure 3- 3c, see also chapter 4). Nevertheless, implied by Hubáček et al.[1], h-BN is very sensitive to moisture. Also, h-BN can oxidize in the presence of water which interacts to form boric acid bonds (B-OH) as follows [4]:

$$\frac{13}{2}\ O_2 + 8\ \ BN + H_2O \rightarrow 2\left[\left(B_2O_3\right)_2 OH\right] + 4N_2 \qquad (3.\ 1)$$

Furthermore B_2O_3 reacts with moisture according to:

$$B_2O_3 + 3H_2O \rightarrow 2B(OH)_3 \qquad (3.\ 2)$$

This consideration leads to the formation of boric acid ($B(OH)_3$) due to the presence of diboron trioxide (B_2O_3).

Further, a chemical model of formation of boron nitride was suggested by Hubáček et al.[1] to be applied on boric oxide and ammonia where a hexagon, formed alternatively from boron and nitrogen atoms, is a precursor of the boron nitride monolayer and possessing –OH leaving groups at boron and H– radicals at nitrogen sites, respectively. In return, X-ray analysis has revealed a low-temperature form of boron nitride with structural faults resembling those which were found in some forms of graphite and named as turbostratic BN[5].

3.2.2 Reproducibility and homogeneity of stable films

In order to get a B/N height ratio closed to 1 and to reduce significantly all contaminants on films, one needs to take account some modifications on following these steps:

- **New**: Introduction of hydrogen as a reactive gas added to the Ar/N_2 gas mixture. The pressure in the chamber is varying related to the gas flow.
- The reduction of the RF power to reduce F contaminants
- Distance substrate-target to keep a growth rate constant
- Increase the substrate temperature.

In order to reduce the influence of moisture, now films will be placed under a desiccator immediately after deposition.

3.2.2.1 RF plasma power

During all film depositions at 300 W and distance substrate-target between 4 and 8 cm, it was notify that after a certain time, the cathode column was abnormally warm. This led to Fluorine (F) contamination from 2 Vinton O-rings present in the cathode. Indeed, the latter is a fluoro-carbon elastic-polymer (elastomeric) which only resists to maximum 200°C, leading to F contaminants observed by XPS measurement (see Figure 3- 3b).

To find an appropriate solution, the reduction of the RF power supply was compulsory. In Figure 3- 4a, the thickness of films, respectively the growth rate is linearly dependent in respect with the RF power. Then, the shape of the infrared spectra was analyzed in order to see the influence of the RF power on contaminants and to get the appropriate profile of h-BN (Figure 3- 4b). Noteworthy is that the increased absorption for high RF power is related to the thickness.

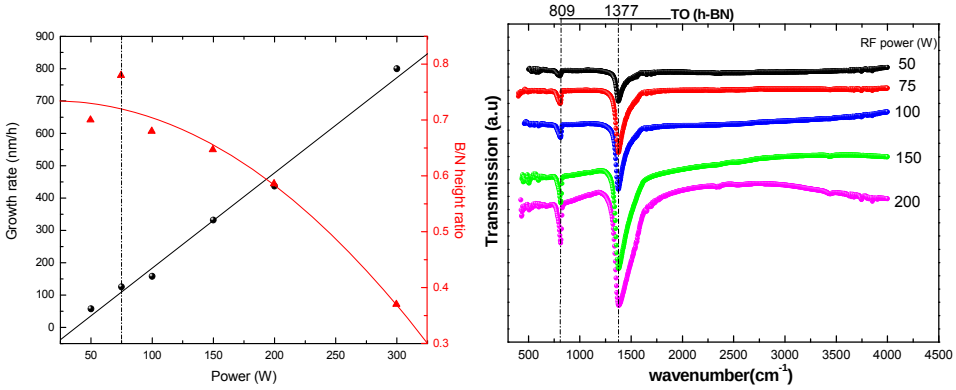

(a) (b)

Figure 3- 4: Role of the RF power on growth rate (a) and on shape of IR spectra (b) for films deposited with 73% Ar, 18% N_2, 9% H_2.

A final decision was undertaken to set the RF power supply at 75 W in accordance with the high value of the B/N height ratio (Figure 3- 4a). Higher than 75 W, it was observed using EDX analysis that the presence of C and O contaminants is significant and probably coming from air atmosphere. I put forward the hypothesis that BN target is not totally deoxidized or gas lines have internal leaks. Under 75 W RF power, the C and O contaminant content is constant for both of them but the growth rate is very low.

3.2.2.2 Distance substrate-target

Whereas RF power and substrate temperature are fixed to 75 W and 160°C, respectively, the distance substrate-target is varying from 4 to 8 cm. As the substrate - target distance changes, the growth rate changes as well. I put forward the hypothesis that the low RF power and low substrate temperature imply slow diffusion of adsorbed atoms (B or N) on Si substrate. Moreover, if the growth rate is high, contaminants as C and O are deposited quickly. Here, the growth rate is used as an indicator of the presence of contaminants. The higher the growth rate, higher is the contaminants content in the bulk BN material. Here, the purpose of the distance substrate-target parameter is to keep the growth rate lower. By bringing substrates closer to the intense plasma zone, that reduce considerably contaminants (traces of CO_2 are minimized). Only, the optical fingerprints of h-BN are clearly shown in the FTIR spectra at different distance substrate-target (Figure 3- 5a). The shape of the growth rate curve related to the distance substrate- target shown in Figure 3- 5b. A good compromise about the reproducibility of the h-BN films leads to fix the distance substrate-target of 4 cm, corresponding to 70 nm/h.

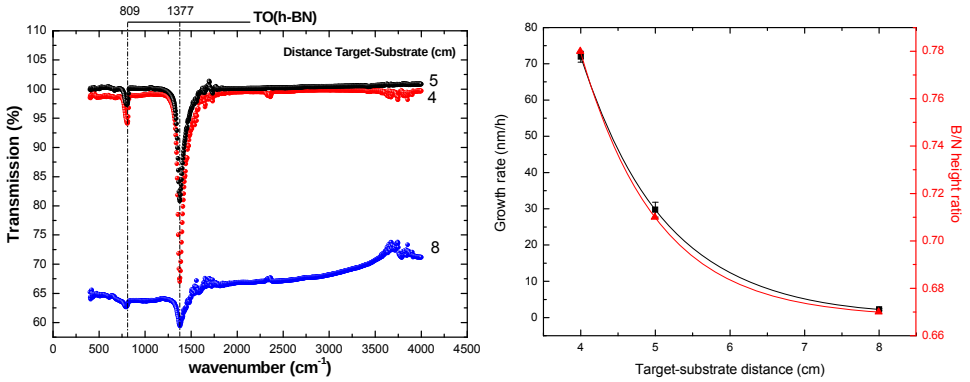

(a) (b)

Figure 3- 5: FTIR spectra (a) and the growth rate (b) of films at different distance substrate-target.

Hence, all further depositions will be performed at 75 W and 4 cm substrate-target distance.

3.2.2.3 Ar-N_2-H_2 gas flow controllers

To get a pure h-BN film, one should optimize the Ar-N_2-H_2 gas flows. This parameter is essential to the formation of the hexagonal phase. Whereas Ar is used to sputter the BN target (see chapter 2), N_2 in addition to Ar is used to reach the stoichiometry of films. A third gas is introduced within the Ar-N_2 gas mixture to enhance the purity of the films during deposition. This gas is dihydrogen (H_2). H_2 was used as plasma cleaning to remove impurities and contaminants from surfaces (walls, cathode and substrates). Indeed, with his small size, H radicals react more easily with contaminants as oxygen, and give OH radicals[6]. OH radicals are known to be volatile components which can be evacuated from the chamber during processing[7]. These species react with organic contaminants to form H_2O, CO, CO_2, and lower molecular weight hydrocarbons. These compounds have relatively high vapor pressures and these contaminants are again vaporized and evacuated from the chamber during processing. The resulting surface is ultra-clean.

Meanwhile, film presenting the lowest C and O contaminations peaks (EDX and FTIR spectra) was taken as reference sample (1-91113C (%): Ar (80); N_2 (20); H_2 (10)) for all further EDX measurements until a new film is getting quality better. After many depositions using hydrogen, a series of growth rate measurements was achieved by varying hydrogen content into an Ar/N_2 ratio

(55.6 sccm (80%) /10 sccm (20%)) constant and fixed. Then, the N/B height peaks ratios were established with respect to the reference sample.

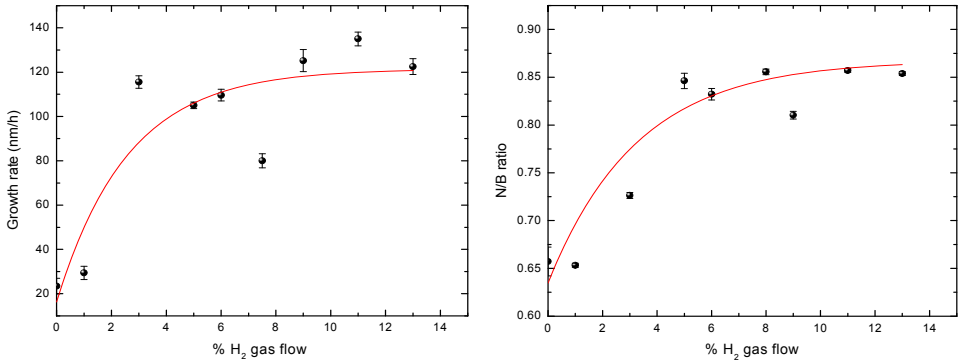

(a) (b)

Figure 3- 6: Influence of H_2 gas flow on the growth rate (a) and N/B ratio (b).

When H_2 gas flow is added to a constant Ar/N_2 plasma mixture, the growth rate increases exponentially from 0% to 5% and remains almost constant between 5% to 13% (Figure 3- 6a). According to the fitting curve, the growth rate of films grown with 5% and 6% H_2 gas flow are the more stable with the lowest error bar and predominantly reproducible. As shown in Figure 3- 6b, the growth rate constant between 5% to 13% implies an horizontal asymptote with N/B= 0.85.

Thence, one changes slightly Ar gas rate from 55.6 sccm (80%) to 69.5 sccm (100%) to keep the plasma even more stable and i assume the H_2 gas flow is optimized at 5 sccm (5%). Then, one looks for the influence of nitrogen with respect to the growth rate. By varying nitrogen, the growth rate reaches an optimum and the shape of the curve is shown in Figure 3- 7a. Films grown faster (around 125 nm/h) correspond to 47.5 % N_2 (23.75 sccm) within Ar/H_2 gas mixture. The N/B height peaks ratio from the same series of growth rate measurements (Figure 3- 7a) was established and shown in Figure 3- 7b. A fit of the experiment data was drawn, revealing an extremum at around 44% N_2 corresponding to the higher N/B ratio (0.88).

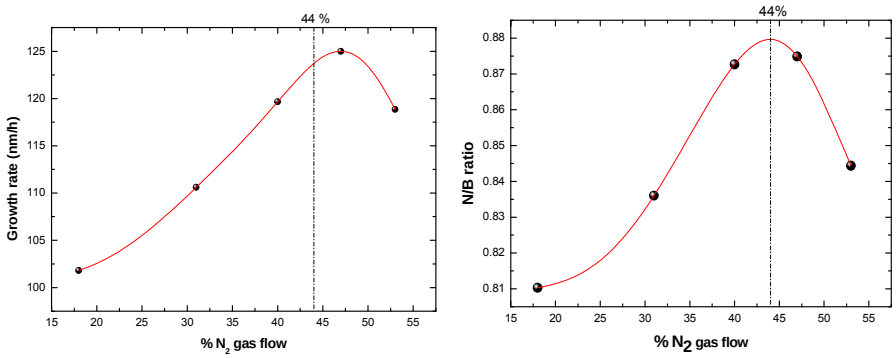

(a) (b)

Figure 3- 7: Influence of N_2 gas flow on the growth speed (a) and N/B ratio (b).

To summarize, a SEM image representing the mixture of 51%Ar, 44%N_2, and 5%H_2 is shown in Figure 3- 8a. After several experiments with the same mixture, these films correspond to constant and stable growth rates and lead to their quasi-stoichiometric (Figure 3- 8b). A shape of the infrared spectra corresponding to a stoichiometric film is observed in Figure 3- 8c.

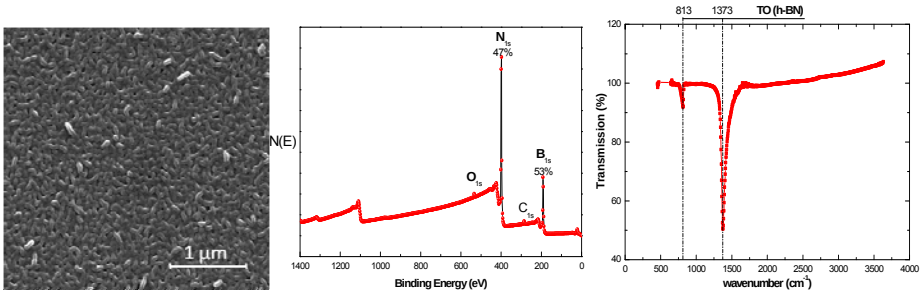

(a) (b) (c)

Figure 3- 8: A 200 nm thick film deposited on Si (100) with 51% Ar, 44% N_2 and 5% H_2 plasma mixture observed by SEM (a).The stochiometry of this film is verified by XPS spectra (b) and the features of stoichiometric h-BN film are visible in a FTIR spectrum (c).

3.2.2.4 Temperature

The growth rate remains more or less constant with the substrate temperature (Figure 3- 9a). For technical reasons concerning the reliability of the heater element, temperatures never exceeded 600°C. For different films grown from 100°C to 600°C, the full width at half maximum (FWHM) from FTIR spectra at 1376 cm-1 was measured. In this temperature range, FWHM from FTIR

measurements gives an idea about the crystal size and it is slightly increasing with the substrate temperature (Figure 3- 9b).

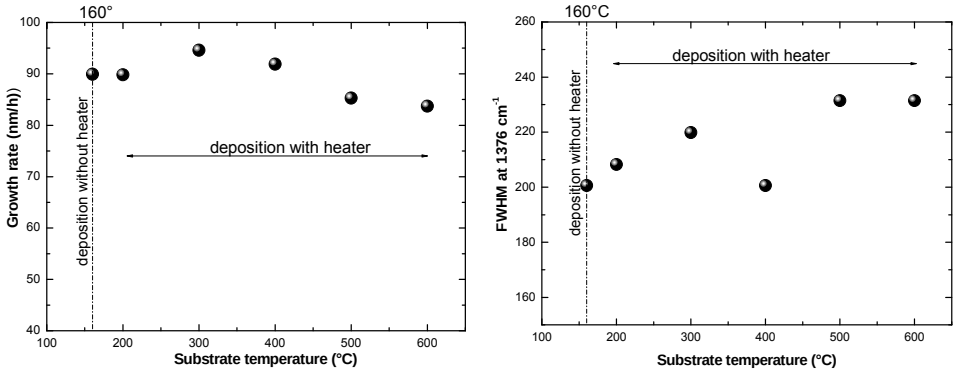

(a) (b)

Figure 3- 9: Growth rate (a) and FWHM at 1380 cm^{-1} (b) in function of substrate temperature. Depositions were performed close to the intense plasma zone.

To summarize, the heater element is used in this temperature range i.e. 100°C-600°C, which is not enough to observe any variations concerning the growth rate or the FWHM. To see a significant sizes of the crystallites which is inversely proportional to FWHM, the heater element should reach 1500°C [8,9]. That is not possible using this substrate holder.

Wherefore, thereafter, films will be deposited without the use of heater element.

3.3. Synthesis of h-BN (NWs) and interpretation

It is known that oxygen and carbon are the most prominent contaminants in different BN materials, which can be partially explained by the fact that B, N and C form a ternary compound system[10]. Therefore, the choice is made to add H_2 as process gas to the mixture of Ar and N_2, in combination with a BN target. This explains the drastically diminution of O impurities within h-BN films as observed in Rutherford Backscattering Spectroscopy spectra (see section 3.3.2) and confirmed by Hubáček et al.[1], when H_2 is added as a reduction agent for the preparation of pure h-BN. Secondly, the production of H atoms increases strongly as soon as H_2 was introduced in argon and reached an optimum at appropriate $H_2/Ar+N_2$ gas flow ratio in the plasma thus altering the floating potential and therefore the energy of species on the sample surface[11]. This is a sine-qua-non condition to get the (002) c-axis normal to the substrate[12,13,14,15]. The h-BN phase will be etched quickly in the Hydrogen/Argon plasma mixture

owing to the weak Van der Waals forces along the (002) c-axis orientation[7]. While the sp^2 hybridization with much higher resistance to H/Ar etching causes the nanowalls to grow higher and longer rather than thicker[7]. Their structural, morphological and opto-electronic properties are discussed with respect to the effects of the H_2 gas rate.

Figure 3- 10 shows several field emission scanning electron microscopy (FESEM) images of h-BN films deposited on Si using different H_2 gas concentrations. It is very clear that by the influence of H_2 during the deposition process, the deposited films are gradually evolving into 2D nanowall structures, whereas pure N_2/Ar plasmas lead to a granular structure. FESEM shows clearly well-separated platelets with bending and crumpling morphology, which are vertically positioned in agreement with TEM with respect to the substrate surface. In these experiments, the minimum amount required for the nanowalls formation is 1 % H_2. The dimensions and density of these walls are also undoubtedly dependent on film thickness. Whereas a 200 nm thick film shows densely packed walls of ~ 100 nm in width, thicker films become more porous, with ~ 1 µm wide walls that cover the surface more sparsely. Note that the walls in the case of a hydrogen gas addition R_{H2} of 5 %, shown in (Figure 3- 10d2), are sparser and better separated from each other as compared to the other samples (b2, c2, e2), suggesting an optimum concentration to form these structures.

When large additions of H_2 are used, the nanowall formation is being suppressed. For 20 % H_2 (Figure 3- 10f2), an intermediate situation is observed, with the platelet-like structures still visible, but already showing signs of granularity again. For 36 % hydrogen addition (Figure 3- 10g2), a pure granular morphology is seen again. The total pressure is constant but not partial pressure. When H_2 gas flow is increasing in the deposition chamber, insufficient N_2 is expected, disturbing the stoichiometry of the layers, rather than the pure chemical influence of large amounts of H_2.

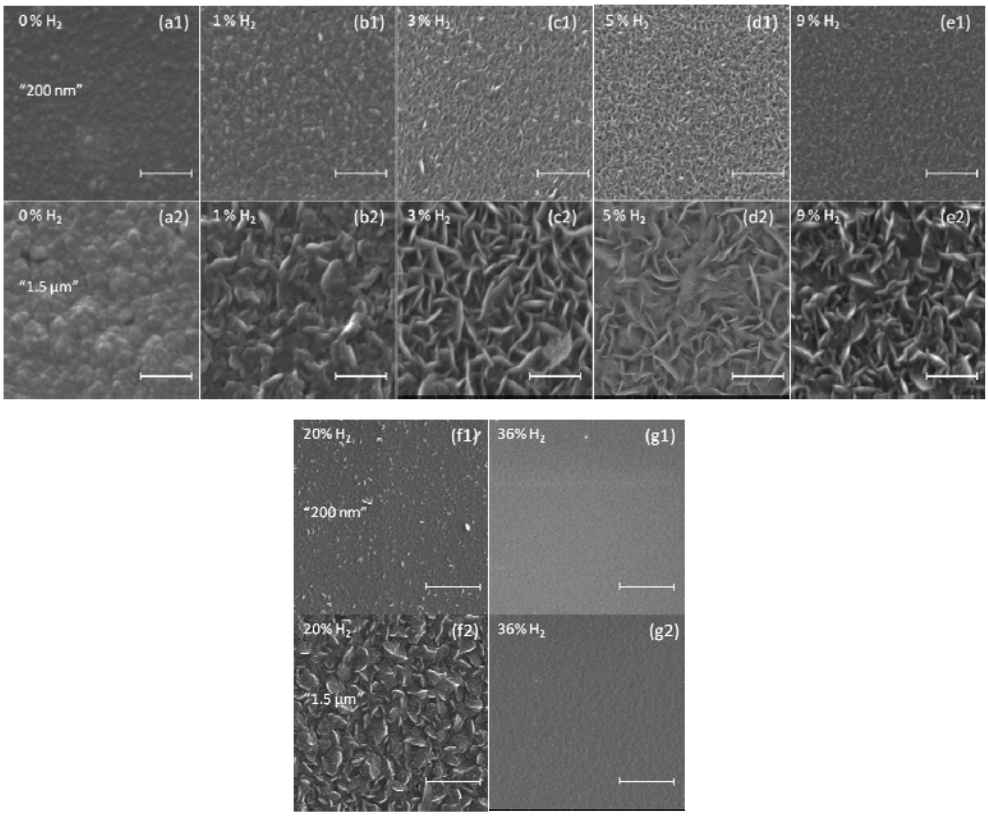

Figure 3- 10: FESEM images of h-BN films deposited on Si using different H_2 gas concentrations added to the Ar/N_2 plasma, leading to 200 nm (series 1) and 1.5 µm (series 2) thick layers. Inset: All images have the same magnification (x80000) and same scale bare (1 µm).

In case of longer deposition times, and thus thicker deposits, the additional effect of sub-branching starts to occur, leading to an increase in surface-to-volume ratio. In Figure 3- 11a, a FESEM pictures of a ~ 10 µm thick film on Si shows that new, smaller nanowalls start to nucleate on the sides of the larger, already present structures, thus forming 3D nanostructures. The BN nanowall and sub-nanowall formation is completely substrate independent. Experiments carried out on different materials like fused silica, sapphire, quartz, and freestanding unpolished polycrystalline diamond, all led almost to the same results (Figure 3- 11b-e).

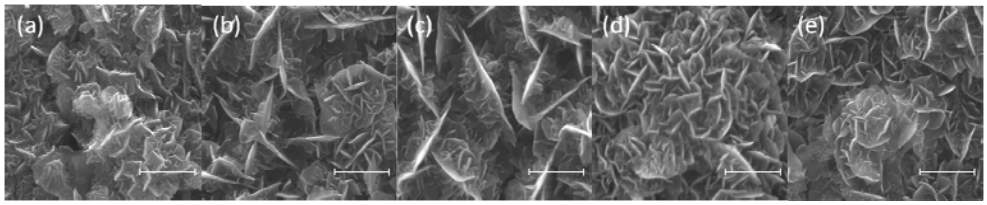

Figure 3- 11: Films of ~ 10 µm thick deposited with 5% H_2 on (a) Si (100); (b) fused silica; (c) sapphire; (d) (0001) quartz; (e) freestanding unpolished polycrystalline diamond Inset: All images have the same magnification (x80000) and same scale bare (1 µm).

At this stage, it is noteworthy that the growth of the boron nitride nanowalls shows certain similarities with the formation of carbon nanowalls (CNWs)[16,17]. According to Shiji *et al.*[18], H_2 is a prerequisite without which carbon nanowalls were not fabricated, a role that is tentatively attributed to an etching effect based on the presence of hydrogen radicals on the growing surface[19,20]. In addition, fluorine has been put forward as a crucial element for the formation of CNWs, as this element is usually constituent of the respective precursor gasses. This is also the case in the work of Yu and collaborators, where use is made of microwave plasma CVD in combination with $BF_3/N_2/H_2$, to form comparable BN structures[7]. The results reported here unmistakably contradict these findings: fluorine is not an indispensable factor in the formation of BN nanowalls using PVD in combination with a BN target and $Ar/N_2/H_2$ gas mixtures.

Similar to the growth of nitrides or oxides from a metallic target by reactive sputtering, the stochiometry of films is related to the growth rate[21]. The sine-qua-non condition to reach the stochiometry, the growth rate must be slow but mainly constant. When conditions are not respected, the target undergoes the plasma ion nitriding, the growth rate decreases and the composition of films changes[22,23].

Figure 3- 12 represent the growth rate deduced by taking cross-sectional SEM versus the hydrogen rate in the Ar/N_2 gas mixture. The growth rate increases from 0 to 3% H_2. After 3% H_2 in the Ar/N_2 gas mixture, the growth rate drops clearly due to the change of chemical composition. **Assumptions**: The surface of the target undergoes plasma ion nitriding[22,24,25]. Also, a possible leak from the H_2 gas line leads to a change of composition. Indeed, when the H_2 is on excess (36%), O is entering together with H_2 in the plasma at much higher concentrations and attacking BN films more effectively. That is followed by the change of composition of the deposition.

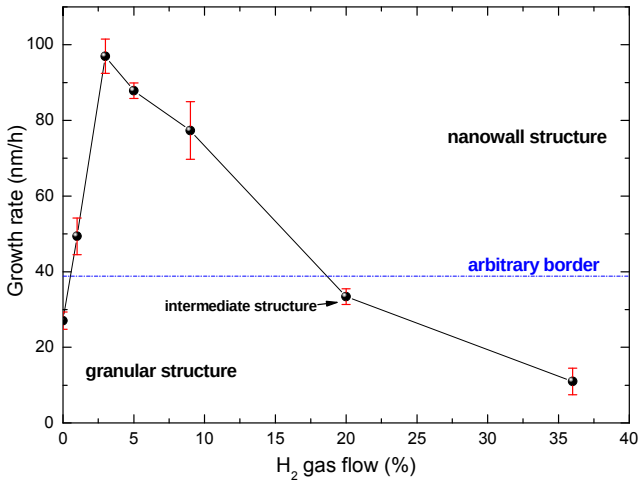

Figure 3- 12: The growth rate related to H_2 gas flow.

Moreover, related to SEM (Figure 3- 10), the growth rate has an arbitrary border (hypothetical border) at around 40 nm/h. Films grown under 40 nm/h are considered as a granular structure films (0%, 20% and 36% H_2). Whereas films grown with the growth rate higher than 40 nm/h, represent nanowall structure films i.e. films grown with 1%,3%,5% and 9% H_2 added to the Ar/N_2 gas mixture.

3.3.1 EDX

The ratio of the peak heights of the B and N peaks are used to evaluate possible changes in the composition of the BN layers. Within these assumptions and the limits of the EDX technique no differences could be observed in the B/N ratio. The EDX results show however a strong influence of the H_2 addition in the plasma (Figure 3- 13 a & b). The more H_2 is added in Ar/N_2 mixture, the less C and O contaminants are detected. Except for the samples growth with 36% H_2, where larger C and O peaks are detected compared to the samples grown without the presence of H_2.Here, the real explanation of why at 36% H_2, O is much higher is not clear yet.

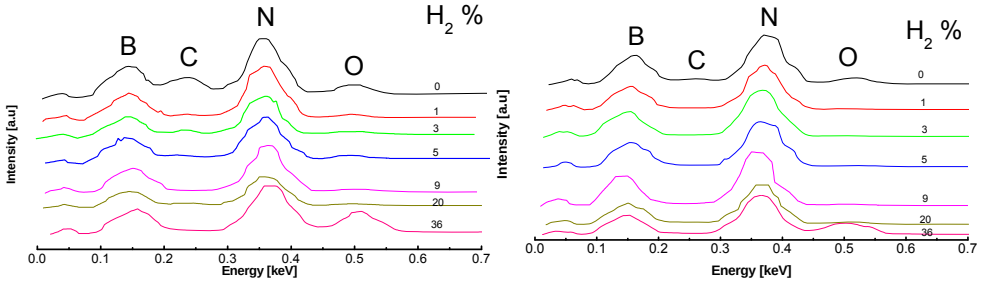

(a) (b)

Figure 3- 13: EDX spectra taken on 200 nm thick (a) and 1.5 µm thick (b) films.

3.3.2 RBS

To assess the nature and the stoichiometric properties of the deposits Rutherford backscattering spectroscopy (RBS) was used. In Figure 3- 14 RBS-spectra are shown of measurements carried out on series of 200 nm thick samples grown with different amounts of H_2. The obtained data were analysed and compared with a Nuclear Data Furnace (NDF) simulation[26] based on a 50/50 ratio of B and N. The first observation is that the sample grown with 5 % H_2 shows the best correspondence between the experimental data and the simulation, pointing to a perfect stoichiometry for this film, i.e. boron nitride is effectively deposited. Only at the Si edge at around 720 keV the width is sharper in the simulation than in the measurement, which points to the presence of a certain degree of surface roughness, in accordance with the SEM images. To support the assumption that too much hydrogen destroys the boron nitride nature of the film, as hinted by the results in Figure 3- 10 f2 & g2, the RBS spectra in Figure 3- 14c show the non-stoichiometric properties of such films. RBS can also detect the presence of impurities such as carbon and oxygen, if their concentration is not too low, a reoccurring problem in the synthesis of BN, as pointed out in the introduction of this section. No trace of oxygen appears in the 1400 keV spectrum leading to the conclusion that it must be strongly below the detection limit of about 5%. This is explained by the use of the hydrogen containing plasma, i.e. first as a cleaning step before deposition to remove oxygen residuals in the deposition chamber, and then during the deposition itself. However, the sensitivity of a RBS spectrum taken at 1400 keV is too low to reliably detect carbon. Therefore, the nuclear resonance around 4220 keV is used, enabling carbon detection, as can be seen in Figure 3- 14b and Figure 3-14d. On average, the backscattering yield for carbon is in this case increased by a factor of approximately 60-100 within the BN layer. From that, the total

amount of carbon within the BN layer grown with 5% H_2 can be determined to about 7.9 x 10^{16}/cm^2 (with 10% accuracy). This corresponds to a relative atomic carbon concentration of approximately 5% in the BN layer. Also, according to the carbon peak, the amount of carbon impurities is almost 2 times less than layers grown without H_2. It is also interesting to note that the actual carbon concentration might even be smaller because small amounts of carbon might be deposited during the ion beam irradiation while doing the RBS measurement. A comparison with the state-of-the art high-purity h-BN single crystals that were synthesised under high pressure learns that this leaves room for improvement. As proven by Taniguchi and co-workers, the superb luminescent properties are obtained for crystals where the impurity content of oxygen and carbon lies between 10^{17} and 10^{18} atoms/cm^3.[27]

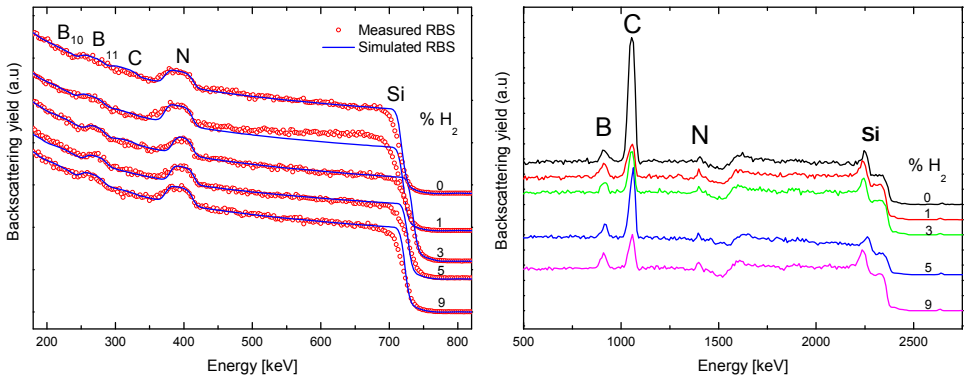

(a) (b)

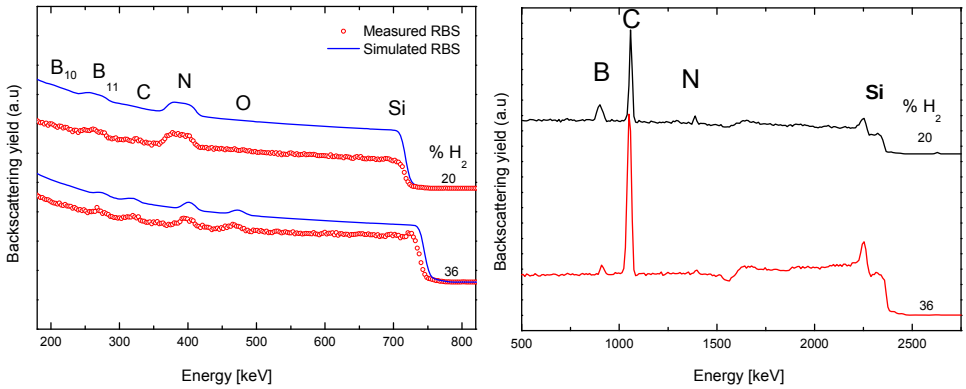

(c) (d)

Figure 3- 14: Rutherford back scattering (RBS) spectra of nominal 200 nm thick BN films as a function of H_2 addition during growth. The spectra were taken under an angle of 170 degree and at incident energy of 1400 keV (a)-(c) and 4200 keV (b)-(d),respectively. In Fig.3-14c, the nuclear data furnace (NDF) simulations are offset from the experimental data due to the suppression of the background signal from the silicon substrate because of the channeling.

The BN layer density can be determined from the B and N peak integrals of the normal RBS spectra .The signals, especially of boron are quite weak, so there is an uncertainty of perhaps 20%. The nitrogen signal is stronger so there the uncertainty is perhaps 10%. RBS measures the product of layer thickness and density (see chapter 2), so the assumed density depends on the layer thickness. Each layer thickness was determined by cross sectional SEM. Results are shown on Table 3- 3.

% H_2*	Thickness Z (nm) Δ~10 nm	EDX peak ratio (N/B)	ρ.Z	Density ($g.cm^{-3}$) ρ	Approx. At. Fract. Of N (%)	Approx. At. Fract. Of B (%)	Approx. At. Fract. Of C (%)	Approx. At. Fract. Of O (%)
0	198	0.66	$8.3x\ 10^{17}$	0.86	39	39	17	≤5
1	156	0.65	$8.0x\ 10^{17}$	1.06	52.5	42.5	3	
3	185	0.73	$5.8x\ 10^{17}$	0.64	48.3	44.8	4	
5	**166**	**0.85**	**$1.1x\ 10^{18}$**	**1.36**	**~50**	**~50**	**≤5**	
9	174	0.83	$7.86\ x10^{17}$	0.93	45.8	48.3	2.5	
20	84	0.85	$8.43\ x10^{17}$	2.05	45	49	6	
36	69	0.6	$3.746x10^{17}$	1.13	33	31	21	15

*: H_2 added to $Ar+N_2$ plasma

Table 3- 3: Summary of results obtained from RBS spectra.

Results from the RBS spectra reveal clearly that the best compromise between N/B ratio and atomic fraction of carbon is obtained by films deposited on Si with 5% H_2 added to the Ar/N_2 plasma mixture. Indeed, these films are stoichiometric with less than 5% carbon content and 5% oxygen content.

3.3.3 TEM

To investigate in detail the evolution of structure and morphology with film thickness, cross sectional TEM images were taken on a sample deposited with 5% H_2 addition. The Si substrate is represented on the top, while a protective layer of platinum (Pt) deposited during FIB preparation is underneath. Between the Si and Pt, one can see the platelets of h-BN, i.e. h-BN nanowalls. The observed intensity variations in the h-BN layer, visible in Figure 3- 15a, are caused by a mixture of electron diffraction contrast and electron absorbing

contrast. The absorbing contrast can be explained by the porous nature of the deposited h-BN layer. The selected area electron diffraction pattern (SAED) in Figure 3- 15b reveals some preferential orientation in the h-BN nanowall structure[28,29]. Many h-BN platelets have a (002) plane tilting over maximum 20° relatively to the normal direction of the Si substrate. This preferential orientation can be shown by the dark field (DF) mode where only electrons scattered towards the (002) direction in the diffraction pattern (indicated by an arrow) is contributing to the imaging process. This DF image clearly indicates the build-up of nanowalls forming the h-BN layer (Figure 3- 15c). Moreover, the cross-sectional TEM images (Figure 3- 15a & c) reveal a changing microstructure during the film formation process: closer to the Si substrate a dense layer is formed, while further during the process, i.e. for longer deposition times, a more porous platelet based structure is grown.

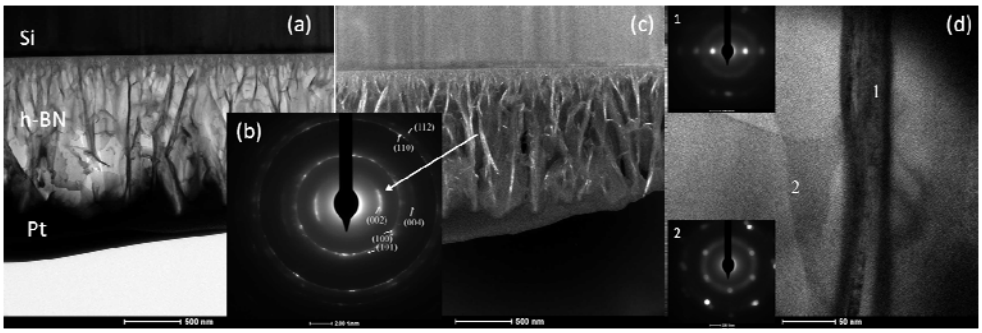

Figure 3- 15: TEM bright field (BF) (a), selected area electron diffraction (SAED) patterns (b), and dark field (DF) using the (002) diffraction arc (c), taken on a 1.5 µm thick film deposited with 5 % H_2. CBED pattern from smaller region of the sample (d) and SAED pattern corresponding to region (1) and (2).

To unravel the crystal structure of the nanowalls, a convergent beam electron diffraction (CBED) pattern in Figure 3- 15d is made from two typical distinct oriented platelets. Not only does this proof the presence of the hexagonal phase, it also points out that the thickness of a platelet or nanowall is typically below 50 nm. This corresponds to a stack of about 150 individual h-BN sheets.

3.3.4 XRD

X-ray diffraction (XRD) spectra in Figure 3- 16 are taken on 1.5 µm thick films deposited on Si (100) with and without H_2 gas addition. In order to clarify the

graph, one have shifted each XRD spectrum and performed smoothing analysis. The data don't reveal a (002) peak at low 2Θ-scales (26°). That confirms results from TEM in which nanowalls is laying almost perpendicularly to the surface. I put forward the hypothesis that due to the position of atoms and electrons, perpendicular to the diffraction plane, the difference in path length between incident and reflected rays doesn't exist. That leads to the non-existence of signal or weak intensity. Moreover, planes with a low electron density will give weak intensities. Peaks observed at Θ lower than 23° could be considered as artifacts of measurement. The unseparated peaks (100) and (101) at 41.51° and 43.753° from the 01-085-1068 JCPDS pattern (turbostratic BN; a= 2,51Å, c=6,69Å), respectively are the typical features of hexagonal boron nitride[30,31]. The latter (t-BN) is another graphite-like form of BN (h-BN) in which the two – dimensional atomic layers are roughly parallel, but each layer is randomly translated and rotated to the layer above and below it[32]. Moreover, one should notice that the peak at 61.7° is related to the Si (400) peak position recalculated using $\lambda_{k\beta}$ of the copper X-ray source into the Bragg´s law.

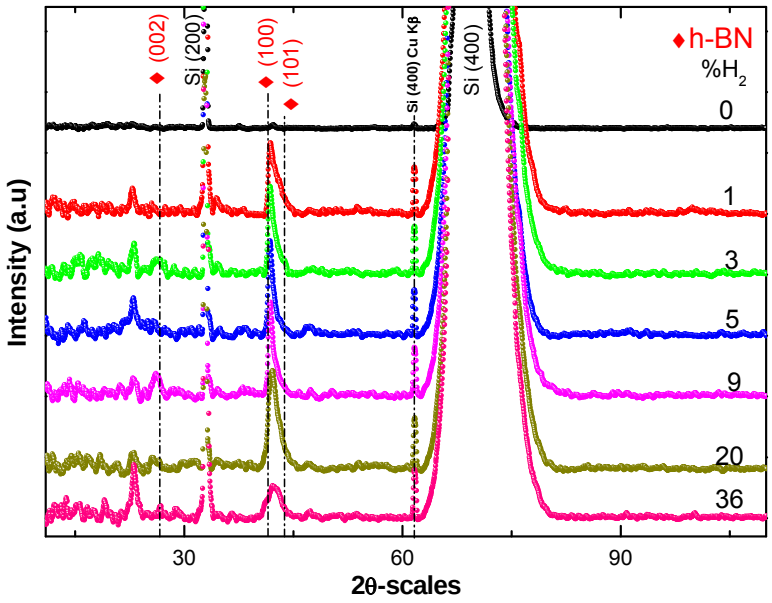

Figure 3- 16: XRD spectra of 1.5 µm thick films grown with different H_2 content.

When the size of the individual crystals is less than about 0.1 µm (1000 Å) , the term "particle size" is usually used .

Near peaks assigned to planes (002), (100) and (101), as shown on Figure 3-16, it was difficult to evaluate the particle size and stress. For this reason, and

to ensure the precision, the strongest and shared (100) intensity peaks was used from all the XRD measurements for calculation of the particle size. Concerning the stress measurement, XRD spectra from granular structured films i.e. 0% H_2 and 36% H_2 were used. Nevertheless, the (100) peaks are overlapping with (101) peaks. To resolve this issue, multiple Gaussian function peaks fitting were used to get a (100) peak decoupled as shown in Figure 3-17a.

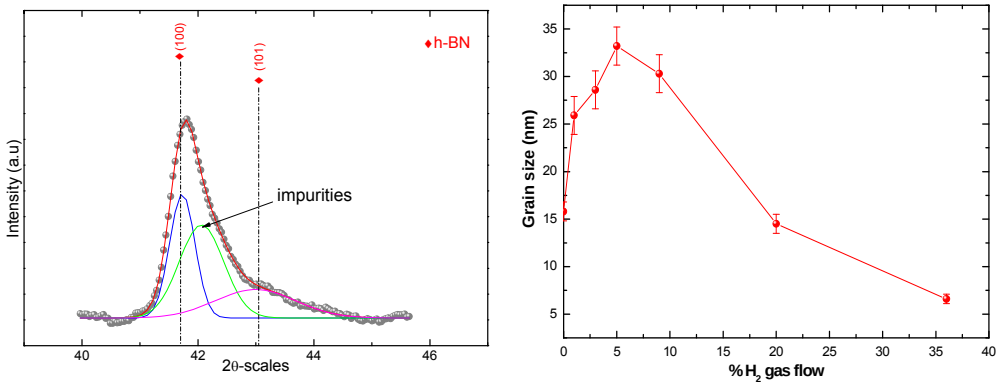

Figure 3- 17: Particle size determined from the (100) XRD peak.

The chief problem in determining particle size is to determine β from the measured width (FWHM) β_M of the diffraction line. The Warren's method is followed: we use a lanthanum hexaboride standard powder (LaB_6) which has a particle size greater than (1000 Å), and which produces a diffraction line near that line from the h-BN .This pattern will contain sharp lines from the standard (LaB_6 powder) and broad lines from layer (polycrystalline h-BN). Let β_S be the measured width, at half-maximum intensity, of the line from the LaB_6 standard.

Then β is given, not simply by the difference between β_M and β_S , but by the Gaussians profiles:

$$\beta^2 = \beta_M^2 - \beta_S^2 \qquad (3.\ 3)$$

$$\Delta\beta = \frac{\beta_M \Delta\beta_M - \beta_S \Delta\beta_S}{\beta} \qquad (3.\ 4)$$

As shown on Figure 3- 17b, β deduced from Equation (3. 3), it can be inserted into Equation (3. 5) to yield the particle size L_{hkl} (Å)**.** Crystal lattices in this size

range cause broadening of the Debye rings (circular patterns of spots on Laue photographs) which is produced by the diffraction of X-rays and determined by the Bragg's law. The extent of the broadening is given by the Scherrer equation:

$$L_{hkl} = \frac{K\lambda}{\beta(radian)\cos\theta} \qquad (3.\ 5)$$

Where K=1; L_{hkl}= particle size; β=broadening of diffraction line measured at half its maximum intensity (FWHM); $\lambda_{CuK\alpha 1}$ = 1.540598 Å.

Also, one should take care of all errors from 2Θ, β so as to calculate crystal size error from the Scherrer equation.

$$\Delta L_{hkl} = \frac{-\lambda \tan\theta \Delta\theta}{\beta\cos\theta} + \frac{\lambda\Delta\beta}{\beta^2\cos\theta} \qquad (3.\ 6)$$

A relation was found between the broadening produced and the nonuniformity of the strain by differentiating the Bragg law:

$$2d \cdot \sin\theta = n \cdot \lambda \qquad (3.\ 7)$$

We obtain[33]

$$b = \Delta 2\theta = -2\frac{\Delta d}{d_0}\tan\theta \qquad (3.\ 8)$$

Where b is the extra broadening, over and above the instrumental width of the line, due to a fractional variation in plane spacing Δd/d. This equation allows the variation in strain, Δd/d, to be calculated from the observed broadening. This value of Δd/d, however, includes both tensile and compressive strain and must be divided by two to obtain the maximum tensile strain alone, or maximum compressive strain alone, if these two are assumed equal. The maximum strain so found can then be multiplied by the elastic modulus E to give the maximum stress present, as shown only for granular structures (0% H_2 and 36% H_2).

Assuming a biaxial stress and neglecting shear components in the film, the stress is roughly estimated by Hooke's law and results will be present in

Table 3- 4 (section 3.4):

$$\sigma = E \cdot \frac{\varepsilon_{\psi}}{2} = E \cdot \frac{\Delta d}{2d_0} \qquad (3.\ 9)$$

Where $\Delta d = (d_0 - d)/d_0$ [26] E (GPa) = 22 // a ;6.9 //c (elastic or Young modulus for h-BN polycrystalline); σ: Maximum compressive stress (GPa); d: plane spacing; d_0: equilibrium plane spacing. In this study, σ=1.3± 0.5 for 0% H_2 and σ=1.435± 0.15 for 36% H_2 with Θ=72°

3.4. Summary

Optimization steps to deposit h-BN films:

- Films grown with 69.5 sccm Ar (100%), 300W RF power, distance target-substrate=5 cm → B/N height ratio= 1.55 (EDX), instable (delamination) and high C, O contaminations.
- Addition of N_2 to compensate the B/N height ratio. A window of B/N height ratio~1 appears between 55.6 sccm Ar (80%), 10 sccm N_2(20%) to 27.8 sccm Ar(40%),30 sccm N_2(60%).But films is still instable (cracks).
- To resolve the instability of films, the RF power is decreased from 300W to 75W and distance target-substrate from 5 cm to 4 cm. Note that to check the influence of distance target-substrate to the growth rate, set of measurements were performed to (80% Ar,20% N_2) films grown from 4cm to 8 cm. still high C and O contaminants.
- Noteworthy is done for the use of heater (temperature substrate from 200°C to 600°C). No real improvement was performed. Thereafter, all films have deposited without heater (150°C-160°C).
- Set of experiments using H_2 added to (Ar,N_2)=(80%,20%) constant. Still B/N height ratio ≠ 1 with less C and O contaminants. Note that the plasma is not stable by introducing H_2 gas flow→ increase Ar gas flow from 80% to 100% and increase of N_2 from 20% to 90%.

Several films deposited on Si (100) with different %H_2 gas additions, were characterized in a qualitative way with the EDS and RBS technique. Their thicknesses were measured via the cross sectional SEM images and with the mass density, roughness and stress, these different results are summarized in

Table 3- 4. Remark: stress of films grown in the presence of H_2 from 1% H_2 and 20% H_2 were not measured due to the porosity giving contradictory results.

Samples (% H_2)	Thickness (µm)	Density (g. cm^{-3})	Roughness (RMS)	Stress (GPa)	
		Sartorius (CP64) micrometric balance	Dektak3ST (nm)	hkl (100)	Dektak 3ST
0	1.49	*1.16 TF*	138	9.8 // a; 3.1 //c	1.3± 0.5
1	1.54	*1.06* ***NW***	205	-	-
3	1.97	*0.75* ***NW***	277.7	-	-
5	1.53	*0.96* ***NW***	318.77	-	-
9	1.69	*0.78* ***NW***	200	-	-
20	1.44	*1.96 TF*	102	-	-
36	1.11	*1.04 TF*	51	10 // a; 3.11 //c	1.435 ± 0.15

NW= Nanowalls; TF= Thin Film

Table 3- 4: Resume of mechanical properties of h-BN

However, it was possible to measure the stress of films grown with 0% and 36% H_2, via two different methods i.e. the shift of h-BN (100) XRD peak compared to the 01-085-1068 JCPDS pattern and the profilometer (Dektak3ST). It could be related to their granular aspect. Further, the density measured by 2 different methods such as the CP64 balance (1.5 μm thick films) and RBS techniques (200 nm thick films- Table 3- 3) reveal their thickness dependences i.e. the evolution of density when the thickness of films and the porosity effect are increased.

3.5. References

1. M. Hubáček, M. Ueki, *J. Solid State Chem.* **1996**, 123, 215.

2. Z.L. Akkerman, M.L. Kosinova, N.I. Fainer, Yu.M. Rumjantsev, N.P. Sysoeva, *Thin Solid Films* **1995**, 260,156.

3. M. Kuhr, S. Reinke, W. Kullisch, *Diamond Relat. Mater.* **1995**, 4, 375.

4. G.F. Cardinale, P. B. Mirkarimi, K. F. McCarty, E. J. Klaus, D. L. Medlin, W. M. Clift, D. G.. Howitt, *Thin Solid Films* **1994**, 253, 130.

5. T. E. O'Connor, *J. Am. Chem. Soc.* **1962**, 84, 1753.

6. J. Wang, Z. Huang, C. Tang, J. Zheng, *int. j. hydrogen energ.***2010**, 35, 7246.

7. J. Yu, L. Qin, Y. Hao, S. Kuang, X. Bai, Y-M. Chong, W. Zhang, E. Wang, *ACS Nano.* **2010**, 4, 1.

8. R. Schaal, « La Cinétique Chimique Homogène », Presse Universitaire de France, **1971**, 162.

9. J. Economy, I. Linn, Handbook ''Boron and Refractory Borides'' **1977**, 202.

10. H. Sachdev, N. Zahn, V. Huch , *z.anorg.allg.chem* **2009**, 635, 2112.

11. F. Rossi, L. Thomas, C. Schaffnit, *Surf. Coat. Technol.* **1998**, 100, 49.

12. S. Ilias, V. Stambouli, J. Pascallon, D. Bouchier, G. Nouet, *Diamond Relat. Mater.* **1998**, *7*, 391.

13. Y. Yamada-Takamura, O. Tsuda, H. Ichinose, T. Yoshida, *Phys. Rev. B* **1999**, *59*, 10351.

14. J. Widany, F. Weich, Th. Köhler, D. Porezag, Th. Frauenheim, *Diamond Relat. Mater.* **1996**, *5*, 1031.

15. C. Collazo-Davila, E. Bengu, L.D. Marks, M. Kirk, *Diamond Relat. Mater.* **1999**, *8*, 1091.

16. M. Hiramatsu, K. Shiji, H. Amano, M. Hori, *Appl. Phys. Lett.* **2004**, 84, 4708.

17. K. Teii, S. Shimada, M. Nakashima, A.T.H. Chuang, *J. Appl. Phys.* **2009**, 106, 084303.

18. K. Shiji, M. Hiramatsu, A. Enomoto, M. Nakamura, H. Amano, M. Hori. *Diamond Relat. Mater.* **2005**, *14*, 831.

19. C. L. Cheng, C.T. Chia, C. C. Chiu, I. N. Lin, *Diamond Relat. Mater.* **2002**, *11*, 262.

20. S. Matsumoto, W. J. Zhang, *Diamond Relat.Matter.* **2001**, *10*, 1868.

21. V. Mortet, PhD thesis « Croissance et caractérisation de couches minces de nitrure d'aluminium et de nitrure de bore cubique obtenues par pulvérisation triode » Université de Valenciennes et du Hainaut Cambrésis (**2001**).

22. C.R. Aita, C.J. Gawlak*, J. Vac. Sci. Technol. A* **1983** ,1(2), 403.

23. D.-Y. Wang, Y. Nagahata, M. Masuda, Y. Hayashi, *J. Vac. Sci. Technol. A* **1996**,14(6) ,3092.

24. A. Kumar, H.L. Chan, J.J. Weimer, L. Sanderson, *Thin Solid Films* **1997**, 406.

25. H. Windischmann, *Thin Solid Films* **1987**, 15554,159.

26. N.P. Barradas, C. Jeynes, R.P. Webb, *Appl. Phys. Lett.* **1997**, 71, 291.

27. T. Taniguchi, K. Watanabe, *J. Cryst. Growth* **2007**, *303*, 525.

28. J. L. Andujar, E. Bertran, Y. Maniette, *J. Appl. Phys.* **1996**, *80*, 6553.

29. Z. Chen, J. Zou, G. Liu, F. Li, Y. Wang, L. Wang, X. Yuan, T. Sekiguchi, H. M. Cheng, G. Q. Lu, *ACS Nano.* **2008**, *2*, 2183.

30. Q.Guo, Yi Xie, Chengqy, *J. Solid State Chem.* **2005**, 178, 1925.

31. X.L. Shi, S. Wang, H. Yang, X. Duan, X. Dong*, Mater. Chem. Phys.* **2008**, 112, 20.

32. J.H. Edgar, Crystal structure, mechanical properties and thermal properties of BN, Properties of Group III Nitrides, Inspec. Publication, March **1994**.

33. B.D. Cullity, Handbook: elements of X-Ray diffraction **1978**, 285.

34. G. Che, B.B. Lakshmi, E.R. Fisher, C.R. Martin, Nature **1998**, 393, 346.

Chap 4 Optical properties of h-BN/h-BN nanowalls

This chapter is dedicated to the optical properties of the thin h-BN films. Infrared techniques and micro-Raman spectroscopy are used to explore more in detail the crystal structure of the thin BN films. The optical parameters of the h-BN layers will be measured using UV-visible-NIR spectroscopy techniques and completed by cathodoluminescence measurements.

4.1. IR spectroscopy (FTIR)

4.1.1 Vibration modes of BN

To identify the allotrope of the BN films, Fourier transform infrared (FTIR) measurements were carried out as a powerful method. Indeed IR spectroscopy is widely used because each phase of BN gives a different absorption spectrum and structure and chemical composition of the films can be sensitively distinguished. The FTIR spectra of BN are characterized by two main wavenumber regions (cm^{-1}):

- **400-2000 cm^{-1}**: A local absorption is considered as short-range effects of Coulomb repulsion between electrons in molecules. It gives the "fingerprint" of h-BN and assigns directly types of chemical bonds (sp^2). (cf chap 1, section 1.1),
- **2000-4000 cm^{-1}**: A global absorption is considered as large-range effects of Coulomb repulsion between electrons in molecules. The common effect is an inhomogeneous repartition of species such as C-H, NH_2, N-H chemical bonds. These are associated with the presence of impurities within the films. (cf chap 3, section 3.2.1).

The BN crystallographic structures can be deduced as sp^2-bonded hexagonal BN (h-BN) and rhombohedral (r-BN) or sp^3-bonded wurtzite (w-BN) and cubic BN (c-BN) from the absorbed frequency bands as shown in Figure 4- 1.

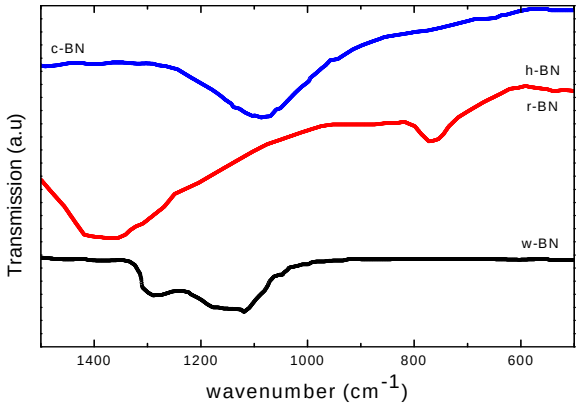

Figure 4- 1: FTIR spectra in transmission of different BN allotropes[1-6].

To complete this characterization, micro-Raman spectroscopy as a complementary technique was performed and summarized in Table 4- 1.

Structures	Modes		Frequencies (cm^{-1})	
	Activity	Symmetry	Infrared	Raman
c-BN[1]	R, IR	F_2 (TO , LO)	1065 – 1050 1340 - 1310	1056 1304
w-BN	R, IR	A_1 (TO ,LO)	(1090, 1120, 1230)[3]	(950 1015 1050 1295)[3]
	R	$2xE_2$		
	inactive	B_1	-	-
h-BN[2]	IR	A_{2u} (TO, LO)	783 828	
	inactive	$2xB_{1g}$	-	
	IR	E_{1u}	1367 1610	
	R	E_{2g}		52
	R	E_{2g}		1366 - 1370
r-BN	R, IR	A_1 (TO, LO)		790[4,5] (TO)
	R, IR	E (TO, LO)		1367[4,5] (TO)

E	Motions doubly degenerate regarding to the main axis.
A	Symmetrical motions regarding to an axis that is generally the main axis of the molecule.
B	Anti symmetric motions regarding to the main axis.
g	Symmetrical motions regarding to a center.
u	Anti symmetrical motions regarding to a center.

Table 4- 1: Phonon modes assigned by FTIR and Raman signals to different BN allotropes (R= Raman active, IR= infrared active).

The application of an external electric field generated by FTIR and Raman spectroscopy induces a sharp change in dipole moment during the vibration of the BN molecules. When molecule vibrations are in resonance with the IR beam, signals (normal mode) from the FTIR spectra are observed and called "infrared active". From Raman spectra, the magnitude of the dipole moment measured by the polarizability of BN molecule reveals also their activity or not (cf chapter 2, section 4.4).

4.1.2 Studies of hexagonal BN phases

H-BN bulk films are characterized by 4 optically active phonon modes, 2 localized in IR spectra and 2 in Raman spectra (2 times degenerated). In Figure 4- 2, these two possible vibration motions of h-BN crystal lattice are characterized by 2 absorption bands as infrared active modes. These absorption features are assigned to the A_{2u} modes at 780 cm^{-1} (B-N-B bending vibration mode parallel to the c-axis) and to the E_{1u} modes at 1380 cm^{-1} (B-N stretching vibration mode perpendicular to the c-axis) of the h-BN bulk material respectively[2,7,8].

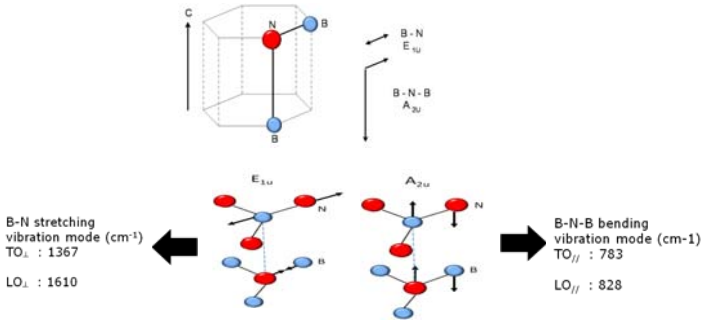

Figure 4- 2: Hexagonal structure of BN and its vibration modes from Geick et al.[2]

Some displacements in frequency of these modes as well as some modifications of shapes are often observed. This behavior has different origins such as crystal size, stress within the films, stoichiometry and the c-axis orientation.

4.1.2.1 Determination of the thickness

It is possible to determine the thickness of thin h-BN films using the IR transmission spectra in normal incidence when the absorption of the strongest band is not saturated. The thickness was calibrated using the cross sectional SEM images. The said thickness was compared to the area of the $TO_{\perp}$ mode at 1380 cm^{-1} (10-20% accuracy). Note that, the weakness of the Van der Waals interactions among overlapping layers[9] leads to high uncertainty of measurements (non measurable) using the A_{2u} mode at 780 cm^{-1}. A physical parameter determined from FTIR spectra is the integrated absorption coefficient.

The integrated absorption coefficient α_i is defined as follows[6,10]:

$$\alpha_i = \frac{\mathrm{A}_i}{t_F} \qquad (4.\ 1)$$

Where A_i is the area (integrated surface) of the $TO_{\perp}$ peak at 1380 cm^{-1}, which varies linearly with t_F as the thickness of h-BN films (SEM measurement). This relationship illustrated in Figure 4- 3a remains valid for all thin films whatever the orientation of the c-axis. This method is a very fast and simple way to evaluate the thin film thickness with a adequate accuracy[9]. However, this method is valid only for films under the same growth conditions i.e. same gas composition, substrate temperature, distance target-substrate and RF power supply because the thicknesses t_F are known from a reference sample with A_i and α_i already determined. Only the deposition time can be changed.

Figure 4- 3b shows that the absorption coefficient varies with hydrogen (H_2) content added to the Ar/N_2 plasma leading to the conclusion that the density of the films varies during the growth (as a function of the thickness) and the H_2 gas flow. This was confirmed by Sartorius micrometric balance (CP64) and by RBS (cf chap 2, section 2.2.1 and 2.2.9, respectively). The mass density deduced by RBS for 200 nm thick h-BN films varies from 0.64 to 2.05 g/cm^3, whereas the mass density measured by Sartorius-micrometric balance (CP64) for 1.5 ± 0.3 µm thick films varies from 0.75 to 2.09 g/cm^3 at different H_2 gas flow content. Due to the lack of sensitivity of the micrometric-CP64, it was difficult to estimate the weight of the h-BN 200 nm thick films.

Using α_i from 200 nm thick films and the densities $\rho_{h\text{-}BN}$ from RBS measurements (cf chap3, table 3.3), we are able to evaluate the average number of the B-N (n_i) bonding at 1380 cm^{-1} by the Jager et al.[10]method (Figure 4- 3b).

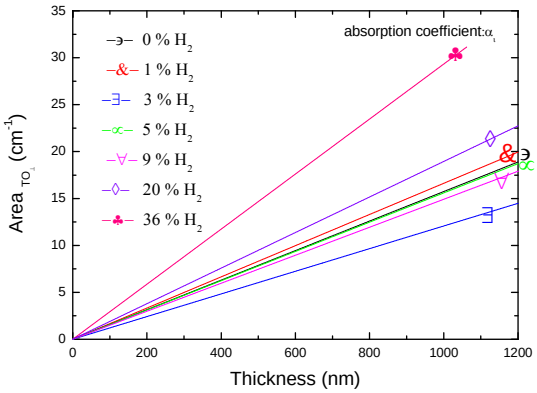

(a)

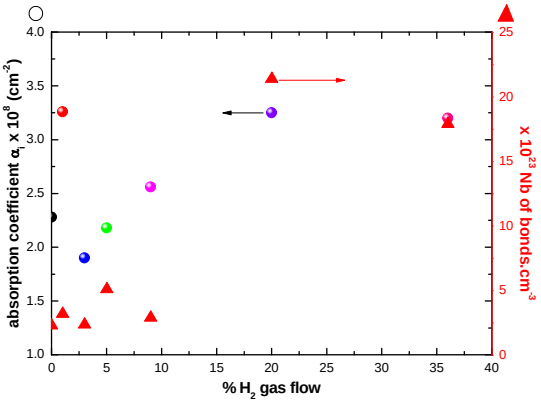

(b)

Figure 4- 3: linear fitting of h-BN film thickness deduced by the area of the $TO_{\perp}$ mode at 1380 cm^{-1} (a). Absorption coefficient α_i and number of bonds per cm^3 in function of H_2 gas flow (b)

h-BN stoichiometric films @H_2=5% present densities at around 1.36 g/cm^3, less than values measured[9,12,13] between 2.1-2.25 g/cm^3. The explanation is the presence of a high porosity on the h-BN thin films as shown in Chapter 3.

4.1.2.2 Determination of the optical constant: theoretical approach

To understand the influence of the c-axis orientation in IR spectra, it is necessary to know the optical constants of bulk h-BN. This is the starting point for the evaluation of the thin film optical properties.

Geick et al.[2] were the first to investigate the optical constants of pyrolitic boron nitride (p-BN) obtained by HPHT in reflection and transmission, using polarized infrared radiation. To simulate these optical constants, they used a classic Lorentz model defining the dielectric function of the p-BN bulk with two harmonic oscillators. The deduced parameters are listed in Table 4-2.

E// c	ε_∞ = **4.1**	$\varepsilon_{0//}$ = **5.09**		
	$\omega_{TO//}$ = 783 cm^{-1}	$\omega_{LO//}$ = 828cm^{-1}	s_1^2=3,26 10^{5}cm^{-2}	γ_1 = 8 cm^{-1}
	$\omega_{IO//}$ = 1510 cm^{-1}	$\omega_{LO//}$ = 1595cm^{-1}	s_2^2=1,04 10^{6}cm^{-2}	γ_2 = 80 cm^{-1}
E⊥c	ε_∞ = **4.95**	$\varepsilon_{0\perp}$ = **7.04**		
	$\omega_{TO\perp}$ = 767 cm^{-1}	$\omega_{LO\perp}$ = 778cm^{-1}	s_1^2=1,23 10^{5}cm^{-2}	γ_1 = 35 cm^{-1}
	$\omega_{TO\perp}$=1367 cm^{-1}	$\omega_{LO\perp}$ = 1610cm^{-1}	s_2^2=3,49 10^{6}cm^{-2}	γ_2 = 29 cm^{-1}

Table 4-2: Parameters of bulk h-BN oscillators are determined by Geick et al.[2] , where the dielectric constant at very low and near infrared frequencies is ε_0 and ε_∞ respectively; ω is the eigenfrequency; $\gamma_{1,2}$ is the damping constant and $s_{1,2}$ the oscillator strength of normal mode TO, LO.

These optical constants allow to determine the relative permittivity for each polarisation[2,6]:

$$\hat{\varepsilon} = \varepsilon_\infty + \frac{s_1^2}{\omega_1^2 - \omega^2 + i\omega\gamma_1} + \frac{s_2^2}{\omega_2^2 - \omega^2 + i\omega\gamma_2}$$

$$= \left\{ \varepsilon_\infty + \frac{s_1^2\left(\omega_1^2 - \omega^2\right)}{\left(\omega_1^2 - \omega^2\right)^2 + \omega^2\gamma_1^2} + \frac{s_2^2\left(\omega_2^2 - \omega^2\right)}{\left(\omega_2^2 - \omega^2\right)^2 + \omega^2\gamma_2^2} \right\} - i\left\{ \frac{s_1^2\omega\gamma_1}{\left(\omega_1^2 - \omega^2\right)^2 + \omega^2\gamma_1^2} + \frac{s_2^2\omega\gamma_2}{\left(\omega_2^2 - \omega^2\right)^2 + \omega^2\gamma_2^2} \right\}$$

$$= \varepsilon_1 - i\varepsilon_2 \qquad (4.\ 2)$$

where $\varepsilon_1 = \mathrm{Re}(\hat{\varepsilon})$ corresponds to the electromagnetic wave propagation in the h-BN bulk material and $\varepsilon_2 = \mathrm{Im}(\hat{\varepsilon})$ to the attenuation (dielectric loss).

Using equation (4. 2), the optical constants could be deduced as follows:

$$n = \frac{1}{2}\left(\left(\sqrt{\varepsilon_1^2 + \varepsilon_2^2}\right) + \varepsilon_1\right)^{1/2} \qquad (4.\ 3)$$

$$k = \frac{1}{2}\left(\left(\sqrt{\varepsilon_1^2 + \varepsilon_2^2}\right) - \varepsilon_1\right)^{1/2} \qquad (4.\ 4)$$

Here, the real part of the refractive index *n* indicates the phase speed, while the imaginary part k indicates the amount of absorption loss when the electromagnetic wave propagates through the material.

It is possible to determine, for each polarisation, the reflection spectra of h-BN bulk material (see in Figure 4- 4)

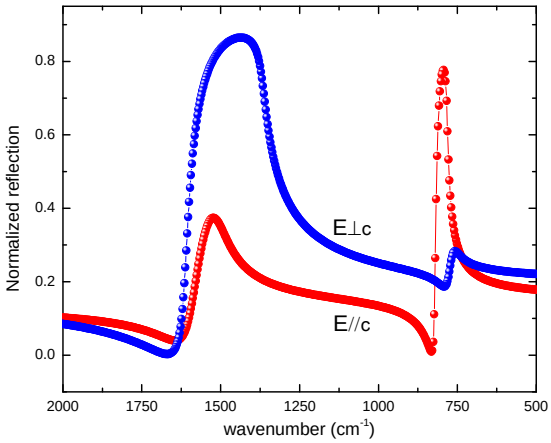

Figure 4- 4: Theoretical reflectivity of BN for both directions of polarization, computed by means of classical dispersion formula[2,6].

For each polarization, the optical constants n and k and their permittivity are calculated as shown in Figure 4- 5 and Figure 4- 6, respectively.

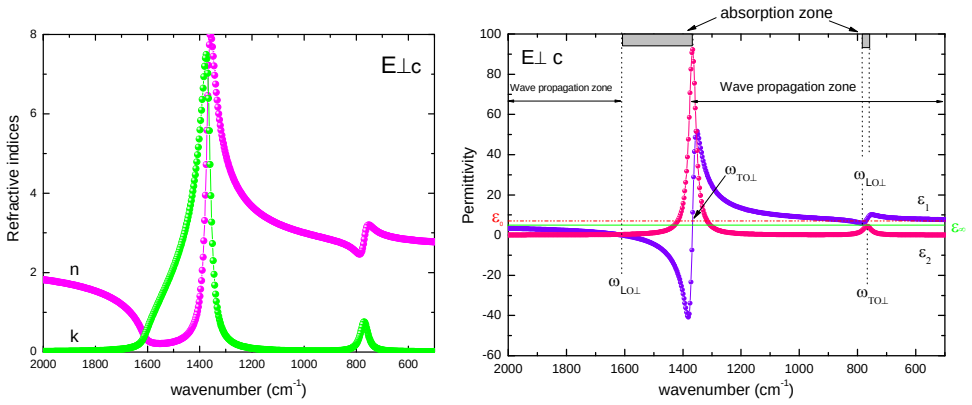

(a) (b)

Figure 4- 5: Refractive index n and extinction coefficient k (a) and permittivity of h-BN bulk material for E⊥ c (simulation[6]).

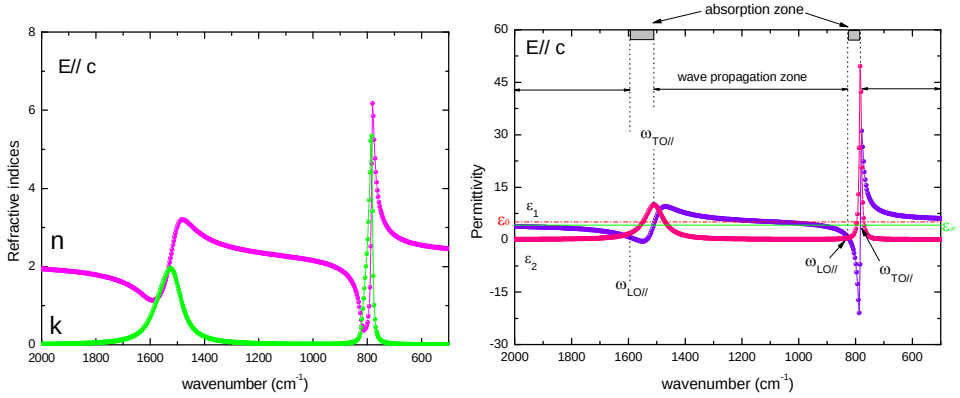

(a) (b)

Figure 4- 6: Refractive index n and extinction coefficient k (a) and permittivity of h-BN bulk material for E// c(simulation[6]).

The main explanation to the negative values of the real dielectric constant (ε_1) as shown in Figure 4- 5b and Figure 4- 6b, is given by the absorption zones of the electromagnetic wave in the h-BN bulk material. These absorptions are observed also in the FTIR spectra in transmission. The optical constants of the h-BN bulk material allow to start a comparative study with the optical constants measured on h-BN thin films samples.

4.1.3 Determination of optical constant: experimental approach

As shown in Figure 4- 7a, the E_{1u} and A_{2u} peaks are located at around 1380 cm^{-1} and 817 cm^{-1} respectively. The broad shoulder in the range 500-1200 cm^{-1} and 1500-2500 cm^{-1} are related to the interference due to the thickness of the films (1.5 µm thick). Moreover, the infrared spectra show the absorption relative to the water vibration at around 1500 cm^{-1} and in this case, water could be either on the surface or in the bulk.

Figure 4- 7b shows sharp absorption peaks at around 817 cm^{-1} and 1376 cm^{-1} for a 200 nm thick layers. These absorption features are assigned to the h-BN E_{1u} and A_{2u} modes respectively[2,14,15] and their representation on the structural lattice are shown in Figure 4- 8.

For a h-BN[16,17] polycrystalline structure , the A_{2u} and E_{1u} modes are located at 811 cm^{-1} and 1377 cm^{-1}, respectively, while in hollow BN nanoribbons[14], A_{2u} and E_{1u} modes are localized at around 818 cm^{-1} and 1367 cm^{-1}, respectively. Multiwalled BN nanotubes (MWBNNT)[16,18,19] show values of the A_{2u} and E_{1u} modes between 800 and 820 cm^{-1} and 1366 and 1372 cm^{-1} respectively, depending on their preparation temperature[15,20]. Since the absorbance (optical density) of a sample is proportional to the thickness of the sample, it should be noted that when films become thicker, the A_{2u} and E_{1u} peaks are more and more broadened.

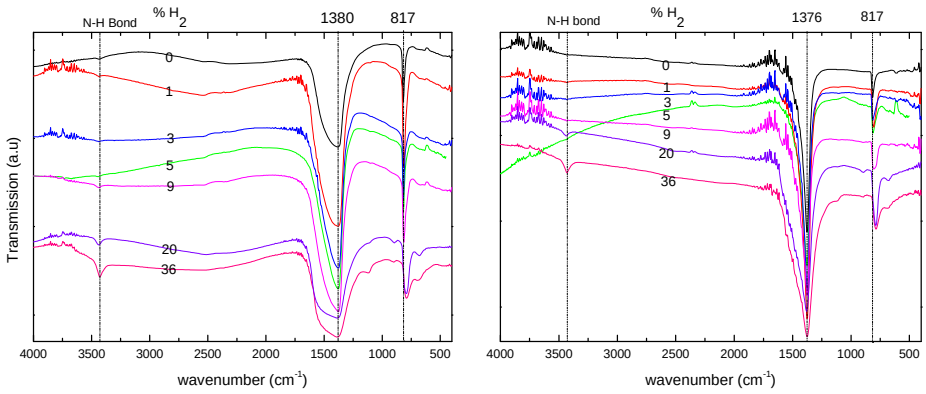

(a) (b)

Figure 4- 7: FTIR spectra for 1.5 µm thickness (a), and 200 nm (b).

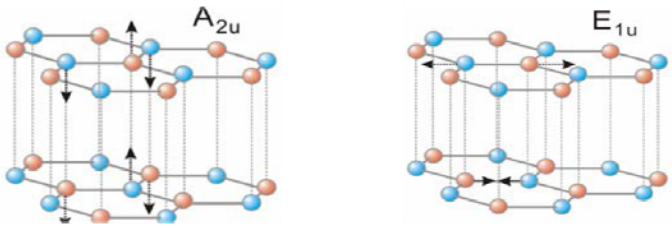

Figure 4- 8: Representation of the A_{2u} -bending mode- and E_{1u} -stretching mode- located at 817 cm^{-1} and 1376 cm^{-1}(1380 cm^{-1}) for 200 nm thickness (1.5 µm), respectively.

After measuring the E_{1u} and A_{2u} position peaks of h-BN / h-BN nanowalls structure, the goal is to estimate the dielectric constants. For that, our FTIR experimental data from the 200 nm polycrystalline h-BN thin film (0%H_2) was compared to an Lorentzian fit using 2 oscillators: one oscillator to fit the stretching mode at 1376 cm^{-1} and the other oscillator to fit with the bending mode at 817 cm^{-1} (see equation 4.2).

This sample presents a h-BN granular structure (cf chapter 3, section 3.3) . For other samples, with nanowall structures it was more difficult to estimate the dielectric constants. As shown in Figure 4- 9, the E_{1u} and A_{2u} absorptions peaks show asymmetric peaks at around 1377 cm^{-1} and 811 cm^{-1} , respectively. This could be related to the anisotropic features of the h-BN while the Lorentz model present a symmetry of absorption peaks for isotropic films. We observe a significant difference around 1550 cm^{-1} assigned probably to the NH_3 or B-O

absorption peaks. The dielectric constants can be roughly estimated and discussed later using the quasi-normal infrared reflection spectra (IRRS) by means of Kramers-Krönig equations.

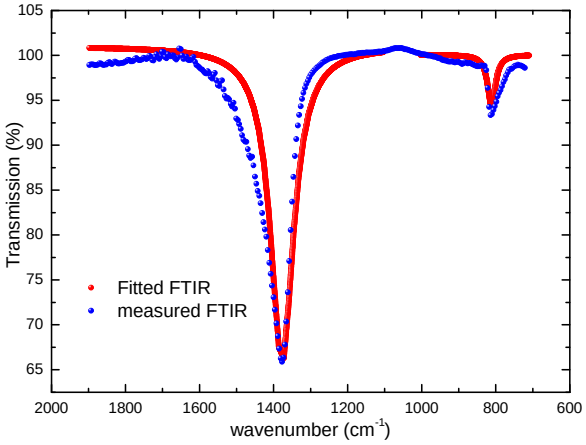

Figure 4- 9: FTIR spectrum of sample (200 nm-0%H_2) and computed by means of classical Lorentz model .

4.1.3.1 Determination of the c-axis orientation

In order to estimate the c-axis orientation of the h-BN nanowall, a simple and fast method[6] is to calculate the A_{2u}/E_{1u} ratio from the depth of the peaks. This ratio is used to determine roughly the c-axis orientation of an "overall" measurement of the complete film. Figure 4- 10a and Figure 4- 11a show the A_{2u} and E_{1u} peaks as a function of H_2 content added to the plasma for two h-BN film thicknesses i.e 200 nm and 1.5 µm, respectively. In Figure 4- 10b and Figure 4- 11b, the ratio of A_{2u}/E_{1u} height are deduced. It can be shown that this ratio is influenced by the H_2 content within the Ar/N_2 plasma.

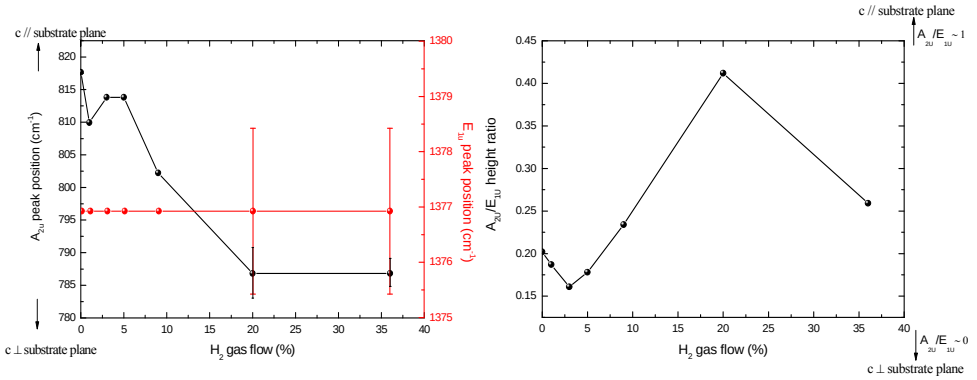

(a) (b)

Figure 4- 10: Influence of the H_2 gas flow on the A_{2u} and E_{1u} positions (a) and A_{2u}/E_{1u} height ratio (b) for 200 nm thick films.

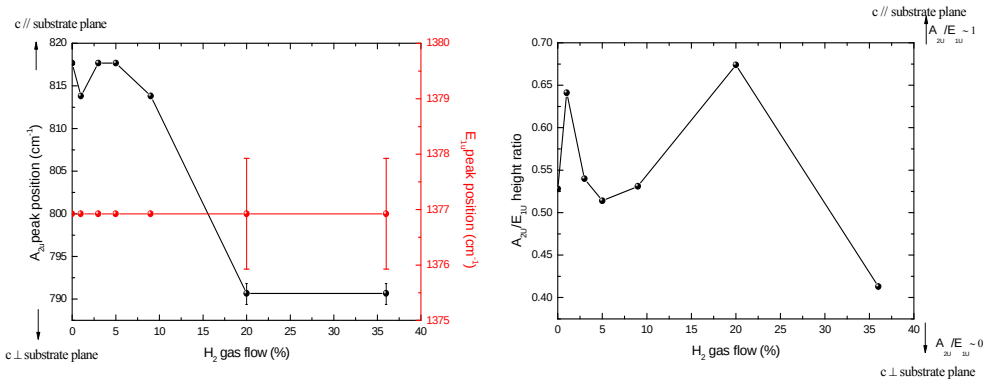

(a) (b)

Figure 4- 11: Influence of the H_2 gas flow on the A_{2u} and E_{1u} positions (a) and A_{2u}/E_{1u} height ratio (b) for 1.5 µm thick films.

As shown in Figure 4- 10b and Figure 4- 11b, the height ratio A_{2u}/E_{1u} with 5% H_2 is 0.18 for the h-BN stoichiometric 200 nm thick films, and 0.52 (approx. x3) for the 1.5 um thick films.

The first hypothesis from FTIR measurement is that the h-BN film starts to grow with the c axis ⊥ to the substrate plane, and then gradually becomes // to the substrate plane. This is confirmed by TEM measurement (chapter 3, section 3.3.3).

4.1.4 Thin film model: effective dielectric function

When samples are turned in respect to its normal axis of rotation regarding to a substrate holder, no shift of the longitudinal optical (LO) and transversal optical (TO) were observed. That assumes the polycristalline structure films are isotropically deposited in the plane of the substrate. The rotation origin of the optical axis Θ is due to intensity of the RF electric field between the cathode and substrate holder[6]. Further, the deposition chamber presents a spherical symmetry. The electric field remains always normale to the substrate during the deposition, only the intensities change depending on the experimental conditions.

Fitting a Lorentz model with two oscillators can not fully describe the experimental FTIR spectra. For this reason, an effective dielectric function model is introduced with a short overview given by A. Soltani[6]. This model is used for an uniaxial anisotropic medium as shown in Figure 4- 12.

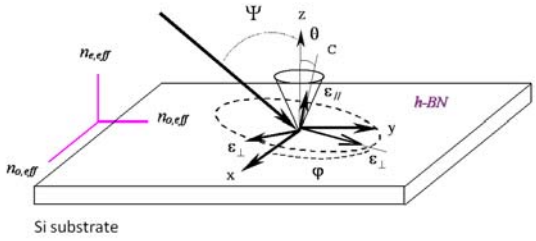

Figure 4- 12: Representation of the optical axis orientation with z, the normal to the substrate surface; Θ is conical angle between z and the c-axis of the h-BN nanowalls and ψ, the incidence angle of the IR beam. h-BN film is considered as an uniaxial anisotropy medium[6].

The classical permittivities of the Lorentz constitute the starting point of the new dielectric function and can be expressed by the dispersive function as follows[21]:

$$\varepsilon_j = \varepsilon_\infty + \Delta\varepsilon_j \frac{\omega_{TO_j}^2}{\omega_{TO_j}^2 - \omega^2 - i\omega\Gamma_j} \qquad (4.\ 5)$$

By replacing the oscillator strength of the vibration mode $\Delta\varepsilon_j$ and introducing the Lyddane-Sachs-Teller relation[22], respectively by:

$$\Delta\varepsilon_j = \varepsilon_{0j} - \varepsilon_{\infty j} \qquad (4.\ 6)$$

$$\frac{\omega_{LO_j}^2}{\omega_{TO_j}^2} = \frac{\varepsilon_{0j}}{\varepsilon_{\infty j}} \qquad (4.\ 7)$$

We obtain:

$$\varepsilon_j = \varepsilon_{0j} \frac{\omega_{TO_j}^2}{\omega_{LO_j}^2} + \varepsilon_{0j}\omega_{TO_j}^2 \frac{1 - \dfrac{\omega_{TO_j}^2}{\omega_{LO_j}^2}}{\omega_{TO_j}^2 - \omega^2 - i\omega\Gamma_j} \qquad (4.\ 8)$$

Where index $j \equiv //$ (out-of plane) or $j \equiv \perp$ (in-plane).

The ordinary and extraordinary effective dielectric function is given by:

$$Polarization\begin{Bmatrix} S \\ P \end{Bmatrix} = \begin{Bmatrix} \varepsilon_{0,eff} = \varepsilon_{\perp}\left(\frac{3+\cos 2\theta}{4}\right) + \varepsilon_{//}\left(\frac{1-\cos 2\theta}{4}\right) \\ \varepsilon_{e,eff} = \varepsilon_{//}\cos^2\theta + \varepsilon_{\perp}\sin^2\theta \end{Bmatrix} \qquad (4.\ 9)$$

The disorientation of the c-axis in the films leads to consider the model of the in-plane isotropy as shown in Figure 4- 13.

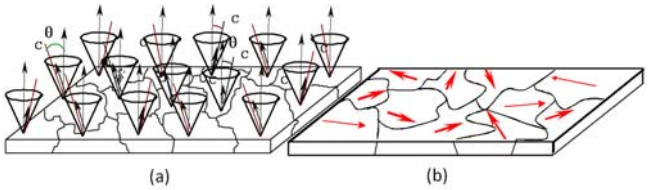

Figure 4- 13 Schematic representation of a preferential orientation of c-axis (a) and the projection of c-axis (b)

The film is textured in the sense that the crystallites or width of the nanowalls constituting the film, admit a preferential orientation of their optical axis localized by the Θ angle (Θ≠0) (Figure 4- 13a).The projection of c-axis on the surface is randomly oriented (Figure 4- 13b).

To obtain the optical constants of a material, the measurement of the reflection and the transmission at normally incident light are usual tools in solid-state spectroscopy. If the material under investigation is a thin film, the interaction of the electromagnetic field with the sample can be enhanced by oblique incidence measurements.

4.2. Oblique Polarized infrared transmission (PIRTo)

4.2.1 Theoretical approach

The same TO and LO modes are excited either by reflectance (R) or transmittance (T). In accordance with the Fresnel equations which describe the behavior of light when moving between different media, the refractive indices (n, k) can directly be derived from R (T) measurements, respectively. Wherefore, the studies will be performed only in reflection. The influence of the c-axis orientation of h-BN crystallite or nanowall structures on the reflection spectra was already described by A. Soltani[6]: Two limit cases could be identified as the c-axis of crystallites are oriented either normal to the substrate (Θ=0) or in the plane of the substrate (Θ=90°). When Θ=90°, two cases were discussed: c-axis is parallel (//) and normal ($\perp$) to the plane of incidence.

Moreover, the measurements depend of the polarization state of the light. Either **P** or **S** is parallel to the plane of incidence (E//c) or out of plane (E$\perp$c) according to the electric component of the wave light, respectively (chapter 2 cf 2.2.3). In this theoretical approach, the reflectivity value was determined using the effective dielectric function under angle of incidence ψ=30° (Figure 4- 14).

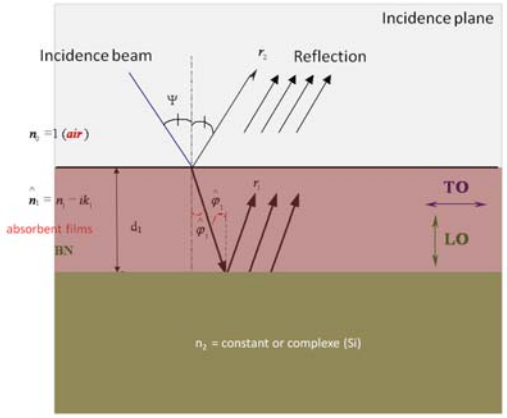

Figure 4- 14: Representation of multiple reflections in the films and directions of atomic vibration according TO or LO modes (angle of incidence ψ=30°).

The simulations of the reflection spectra with an effective dielectric function, give an indication about the general behavior of the h-BN films as follows:

- LO modes are not activated in **S** polarization,
- $LO_{//}$ is activated in **P** polarization only whether the c-axis is normal to the surface,
- $LO_{\perp}$ is activated in **P** polarization only whether the c-axis is parallel to the surface,
- $TO_{//}$ is not observed when the c-axis is normal to the surface.

These various features give the orientation of the c-axis from the type of excited mode for a given polarization. Further, it appears that the thickness has an influence on the shape of reflectivity spectra. Above 300 nm thick films, shoulders in the reflection spectra start to appear and become more and more important when the film thickness increases, leading to a spectra with two phonon peaks[2].

The c-axis orientation in the frame of the effective dielectric function can explain the anisotropy of the h-BN films in the IR spectrum as shown in Figure 4- 9. Indeed:

- The displacement in frequency of $TO_{//}$ mode,
- Variation of its intensity,
- Shoulder band at 1550 cm^{-1} that is assigned to an effect related to the thickness of the film.

4.2.2 Experimental approach

The objective is to determine the c-axis orientation of thin h-BN films. As an introduction, Figure 4- 15a and Figure 4- 15b illustrate the directions of atom vibrations when the c-axis is parallel and normal to the (Si) substrate and their corresponding excited modes, respectively.

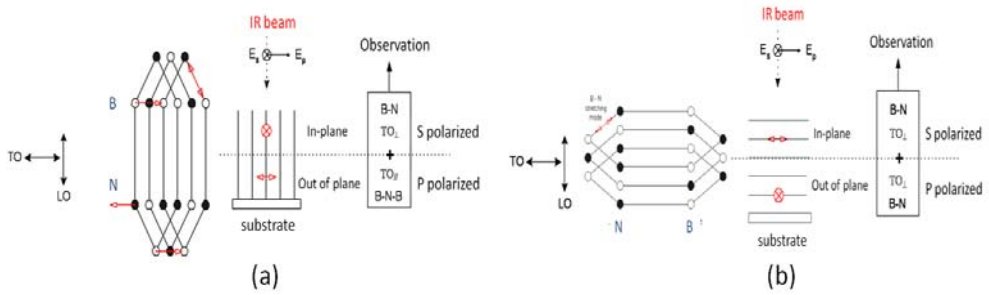

Figure 4- 15: Schematic representation when the c-axis is parallel to the substrate (a) and normal to the substrate (b).

In Figure 4- 16, the normal modes (E_{1u} and A_{2u}) from samples (166 nm thick-5% H_2) and (1.5 µm thick-5% H_2) are clearly seen using the incidence angle of the IR beam at ψ=60° and at ψ=40°, respectively. Thereby the excited modes at oblique incidence are the same in reflection and in transmission. This corresponds to the case shown in Figure 4- 15a where the c axis is parallel to the substrate at normal incidence (ψ=0°). This was confirmed by TEM measurements (cf chap 3, section 3.3.3). This behavior changes if we go from normal incidence to an oblique illumination of the thin film with p-polarized light. With this polarization, the electric field has a component normal to the surface. The surface charges[23] (i.e. Plasmon) produced by this normal component generate a resonance at the LO frequency called the Berreman effect[24] and is observed clearly in Figure 4- 16a and Figure 4- 16b. At ψ=10°, p-polarized at oblique incidence in reflection mode (p-IRRS, see cf 4.2.4) has revealed an average angle value of c-axis orientation in a bulk. Whereas at ψ=45°, it has revealed an average angle value of c-axis orientation on the surface.

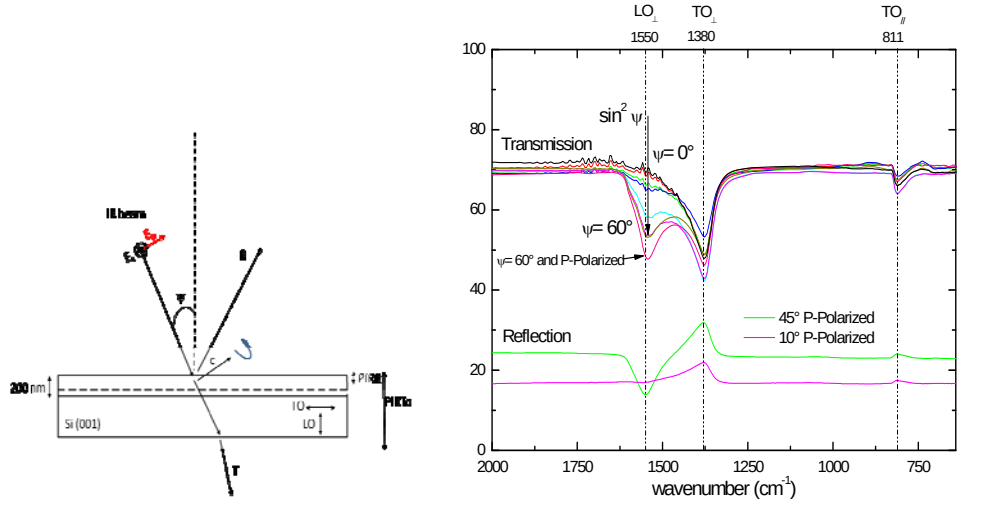

(a)

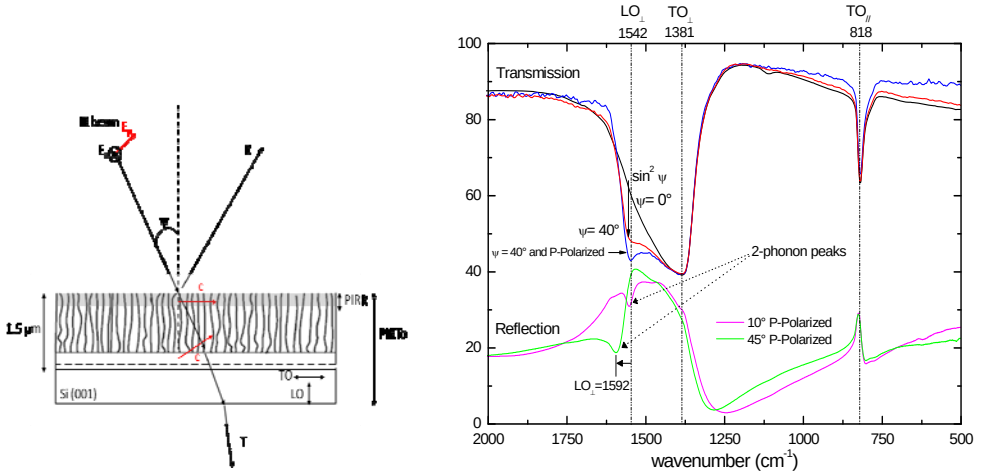

(b)

Figure 4- 16: Sample -166 nm thick-5% H_2- (a) and sample -1.5 µm thick-5% H_2)- (b) corresponding to the case where c is parallel to the Si substrate.

Amongst other, Geick et al.[2] show that the c axis parallel to the substrate is determined by the LO modes at 1595 cm^{-1}. In our case, the LO mode is located between 1542-1550 cm^{-1} depending on the films thicknesses. Here, Polarized

This could be explained as the c axis is lying on the substrate with an angle $\left(\frac{\pi}{2}-\theta\right)$. The value of θ is deduced from the Schubert model[25]. This model describes the offset of the TO and LO modes position versus θ, and allows to determine directly the c-axis orientation as explained below.

4.2.3 The Schubert Model

Schubert et al.[25] were the first to apply the effective dielectric function to h-BN. They used a variable-angle spectroscopic ellipsometry (VASE) to perform their own effective uniaxial thin film model.

For the TO phonon modes, ω_{TO} frequencies were obtained from $\varepsilon_{0,eff}$, excepted for Θ=0°, where only $\omega_{TO\perp}$ can be excited. Two TO resonance frequencies were observed on polarizations **S** and **P** which give frequencies $\omega_{TO\perp}$ in plane and $\omega_{TO//}$ out-of-plane, respectively. TO modes are shifting slightly as follows:

$$\widetilde{\omega}_{TO} = \omega_{TO}\left\{1-\left(\frac{\Gamma}{2\,\omega_{TO}}\right)^2\right\}^{1/2} \qquad (4.\ 10)$$

Where $\widetilde{\omega}_{TO}$ is the apparent frequency, and $\Gamma << \omega_{TO}$ is a damping constant of the TO normal mode. For the LO phonon modes, ω_{LO} frequencies were obtained from $\varepsilon_{e,eff}$. In the h-BN bulk films, linear electromagnetic waves are not coupled to LO phonon modes. Therefore, we are not anymore in the case for bulk films where the film thickness is smaller than the incident wavelength. Under oblique incidence, LO mode absorbs the incident **P** polarization. Only in this case, $\omega_{LO//}$ (ω_-) and $\omega_{LO\perp}$ (ω_+) depend on the cone angle Θ and could be calculated as follows:

$$\widetilde{\omega}=\sqrt{\frac{\alpha^2\sqrt{\alpha^2-4\beta\left(\varepsilon_{0//}\cos^2\theta+\varepsilon_{0\perp}\sin^2\theta\right)\omega_{LO_{//}}^2\omega_{TO_{//}}^2\omega_{LO_\perp}^2\omega_{TO_\perp}^2}}{2\beta}} \qquad (4.\ 11)$$

Where,

$$\alpha=\varepsilon_{0//}\omega_{TO_{//}}^2\omega_{LO_\perp}^2\left(\omega_{TO_\perp}^2+\omega_{LO_{//}}^2\right)\cos^2\theta+\varepsilon_{0\perp}\omega_{TO_\perp}^2\omega_{LO_{//}}^2\left(\omega_{LO_\perp}^2+\omega_{TO_{//}}^2\right)\sin^2\theta$$

$$\beta=\varepsilon_{0//}\omega_{TO_{//}}^2\omega_{LO_\perp}^2\cos^2\theta+\varepsilon_{0\perp}\omega_{TO_\perp}^2\omega_{LO_{//}}^2\sin^2\theta$$

$$\varepsilon_{0//}=5.09\ ;\varepsilon_{0\perp}=7.04$$

$$\omega_{LO_\perp}=1610\ cm^{-1}\ ;\ \omega_{TO_\perp}=1367\ cm^{-1}\ ;\ \omega_{LO_{//}}=828\ cm^{-1}\ ;\ \omega_{TO_{//}}=783\ cm^{-1}.$$

Figure 4- 17 shows the ω_- and ω_+ functions calculated from the previous equation (4. 11) with parameters of bulk h-BN oscillators determined by Geick et al.[2] (Table 4-2). That allows to deduce the corresponding value of Θ by the observation of the LO modes frequencies.

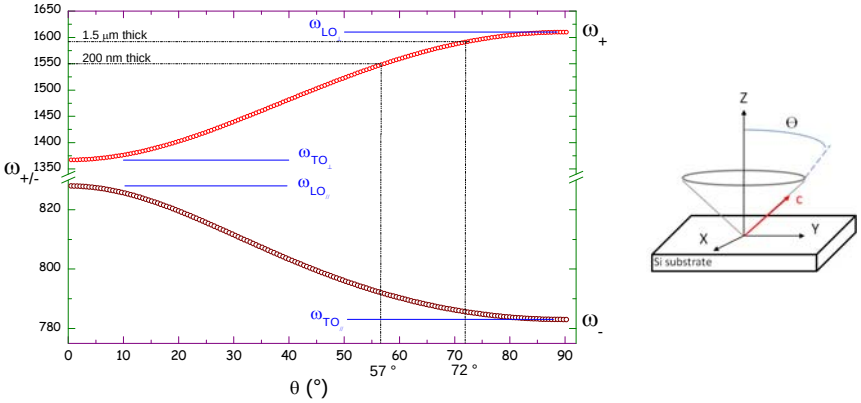

Figure 4- 17: Variation of the optical modes frequencies with respect to the c-axis orientation[2,6].

Schubert et al.[25] have quantified the variations of the frequency optical mode regarding the c axis orientation. When Θ varies between 0 and 90°:

$$\omega_{TO_{//}} < \tilde{\omega}_{LO_{//}} \leq \omega_{LO_{//}}$$
$$\omega_{TO_{\perp}} < \tilde{\omega}_{LO_{\perp}} \leq \omega_{LO_{\perp}}$$

We can notice that for Θ=0° (90°) the second LO mode disappears and only $\tilde{\omega}_{LO_{//}}$ ($\tilde{\omega}_{LO_{\perp}}$) can be excited [21].

The infrared ellipsometry measurements are shown in Figure 4- 17 and could be used together with the FTIR results. The value of θ deduced from $LO_{\perp}$ at 1550 cm^{-1} and at 1592 cm^{-1} for sample@5%H_2 (200nm thick) and sample@ 5%H_2 (1.5 µm thick) is 57° and 72° respectively. These results constitute an average angle value of the c-axis orientation. Indeed, the c-axis angle is tilted when the layers start to be deposited on the Si substrate. Then, c-axis is parallel to the substrate surface when the layers have tended to be deposited before the formation of nanowalls.

The Schubert model[25] constitutes a fast and efficient way to estimate with a good accuracy the c-axis orientation of our h-BN films.

4.2.4 h-BN thin films characterization in IR reflection (IRRS)

The polarized Infrared Reflection Spectroscopy (p-IRRS) of films has been measured throughout the IR spectral region from 400 to 2000 cm^{-1}. All these measurements were performed under P and S polarized light. They were carried out with Θ=10°, quasi-normal with the Si surface substrate. Note that, here the s-polarization (E$\perp$c) and unpolarized light reveal only the TO mode. Wherefore, for clarity the p-polarization (E//c) was only shown in this study because it reveals the TO-LO peak positions.

4.2.4.1 Determination of TO-LO modes

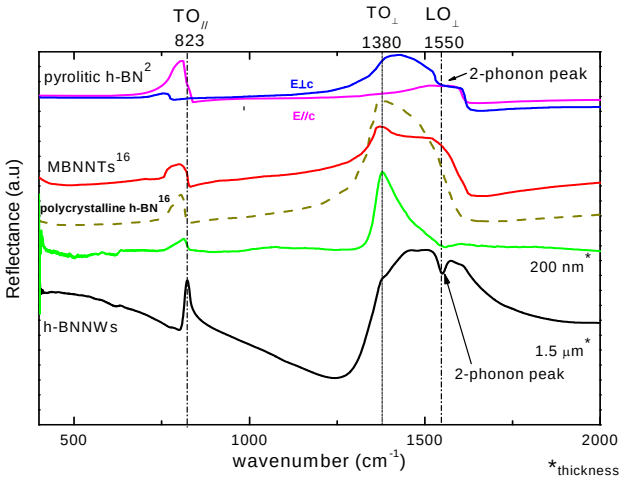

(a)

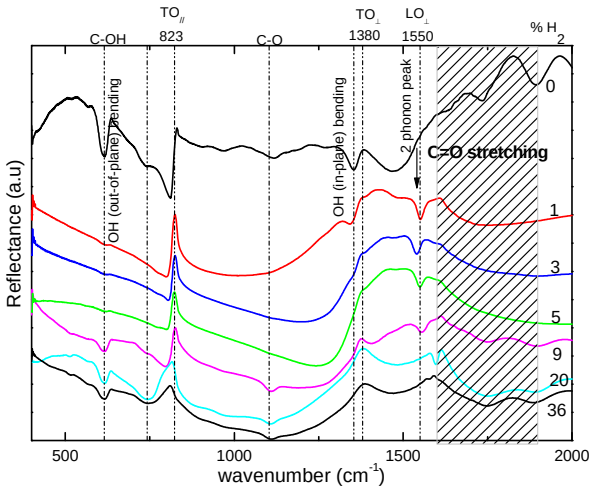

(b)

Figure 4- 18: p-IRRS spectra of h-BN (NWs) for 200 nm and 1.5 μm thicknesses compared to different h-BN structures (Geick et al.2 and Borowiak-Palen et al.[16]) (a).p-IRRS spectra of h-BN nanowalls with different % H_2 gas flow (b).

Figure 4- 18a shows the p-IRRS response of the as grown h-BN/h-BNNWs are compared to a bulk polycrystalline h-BN, pyrolitic h-BN and multiwalled BN nanotubes (MWBNNT). The spectrum of the h-BN/h-BN nanowalls is dominated by the vibrations with a strong dipole moment at 823 cm^{-1} (B-N vibration perpendicular to the nanowalls) and at 1380 cm^{-1} with a pronounced shoulder at 1550 cm^{-1} (B-N vibration along the nanowalls). In the case of polycrystalline h-BN[2,16] and MWBNNT[16,18,19], the corresponding modes are observed at 811 cm^{-1} and 800 cm^{-1} (out-of-plane B-N vibration) and at 1377 cm^{-1} (with a weak shoulder at 1514 cm^{-1}) and 1372 cm^{-1} (in plan B-N vibration) with a pronounced shoulder at 1540 cm^{-1}. In pyrolitic h-BN[2], two characteristics TO modes are observed at 767 (783) cm^{-1} and 1367 (1510) cm^{-1} for the perpendicular (parallel) electric field to the c-axis, respectively.

The corresponding LO modes are observed at 778 (828) cm^{-1} and 1610 (1595) cm^{-1} for the perpendicular (parallel) electric field to the c-axis, respectively. For a polycrystalline h-BN structure, shown in Figure 4- 18a (dotted line), the observed TO-LO splitting is reduced resulting in only one out-of-plane vibration at 811 cm^{-1} and a TO in-plane vibration at 1377 cm^{-1} with a weak LO in-plane component at 1514 cm^{-1}. The TO-LO split between the two components and the relative spectral weight are related to the mixture of the oscillator strength of the modes perpendicular and parallel to the c-axes. It is used as a measure of the orientation of h-BN/h-BN nanowalls (h-BNNWs). This means that a three-dimensional disorder in a polycrystalline h-BN sample results in a very small TO-LO splitting.

In comparison, for MWBNNT[16]/ h-BNNWs, the low frequency $TO_{//}$ phonon is also degenerated and shifted by about -11 cm^{-1}/+12 cm^{-1} to lower and higher wavenumber, respectively. This leads to a decrease/increase of the interaction perpendicular to the nanowalls and consequently to a decrease/increase of the out-of-plane phonon strength, respectively. The high frequency mode of the h-BNNWs is strongly dependent on the c-axis orientation and on the polarization of the light. The observed strong component at 1380 cm^{-1} might be assigned to the TO mode polarized along the nanowalls. The position of the TO mode compared to h-BN is higher than for in-plane pyrolitic h-BN (1367 cm^{-1}), MWBNNT (1372 cm^{-1}) and polycrystalline h-BN (1377 cm^{-1}). This enhancement of IR-response can be explained by the hardening of the TO mode (E_{1u}) along the nanowalls corresponding to the covalent bonds. On the other hand, the LO component is much lower in intensity and therefore softened to 1550 cm^{-1} as compared to pyrolitic h-BN (1610 cm^{-1}) but more intense than in the polycrystalline h-BN (1514 cm^{-1}) and MWBNNT (1540 cm^{-1}).The difference between the out-of-plane mode at 817 cm^{-1} (FTIR-transmission) and 823 cm^{-1} (p-IRRS-reflection) can be explained by the fact that the nanowalls are inclined (around 10°) to the normal (PIRR) of the Si substrate, resulting in a two-dimensional orientation of the

nanowalls and therefore to an increase of the IR-response and a hardening of the TO mode.

The existence of spectral shifts in E_{1u} optical phonon resonance frequencies was observed between $TO_{\perp}$ and $LO_{\perp}$ as a function of the BN thin-film microstructure. There exist a few reports on theoretical and experimental studies of anisotropic lattice vibration phenomena in non-cubic solids. The occurrence of Berreman-polariton[21] resonance in polarized IR spectroscopy (p-IRRS) data acquired from thin films reveal the polar longitudinal optical (LO) thin-film lattice vibration properties centered at 1550 cm^{-1}. According to Geick et al.[2], the deviation of the data of the E_{1u} phonon at the high energy side from the line shape is due to the presence of additional two-phonon absorption and was confirmed by Hoffman et al.[26]. However, amongst certain authors such as Hassan et al.[27] , these features can be attributed to the surface plasmon polariton (SPP) mode of the thin AlN wurtzite film. The SPP mode which is a transverse magnetic (TM) mode vibration resulting from the coupling of an infrared (IR) photon TM mode with a TO phonon is located in between the TO (1380 cm^{-1}) and the LO (1610 cm^{-1}) frequencies of the BN bulk film. In addition, the discrepancy can also be attributed to the quality of the sample (e.g. surface roughness, amount of impurities, carrier concentrations, and so on). The measured IR responses of other samples grown with different % H_2 are compared to h-BN (NWs) with 5% H_2 with same thickness (i.e. ~1.5 µm). Figure 4- 18b shows the evolution of the 2 phonon peaks[2] i.e. the summation to in-plane motion and one optical phonons with lower frequency as a function of the % H_2. So far, samples grown with 1% H_2 to 5% H_2 that shed light on 2 phonons peaks have revealed to the nanowalls their own optical fingerprint. Whereas,2 phonons peaks are completely destroyed for samples containing 0, 9, 20 and 36% H_2 due to possible contamination observed at 611 and 1104 cm^{-1} (C-O band) and at 1700-1900 cm^{-1} (C=O stretching band).

4.3. Raman spectroscopy

Whereas FTIR spectra are generated in transmission and reflection, Raman spectroscopy is only generated in reflection. Using the 266 nm line of an UV laser, it has been extensively used to identify the structure of BN materials.

Intense peaks appear at 1367 cm^{-1}, attributed to the high frequency intra-layer E_{2g} vibration mode of h-BN[28] (Figure 4- 19). The high frequency mode is due to B and N atoms moving against each other within a plane. In this study, the low frequency mode (around 49-52.5 cm^{-1}) characterized by the whole planes sliding against each other[17,26 ,28] could not be detected due to the detection limit of the set up.

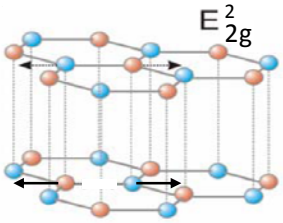

Figure 4- 19: Representation of the high frequency intra-layer E_{2g} vibration mode of h-BN at 1367 cm^{-1}

In Figure 4- 20a, for the stoichiometric sample (5% H_2), the sp^2 band appears at 1367 cm^{-1} with a narrow full width at half maximum (FWHM=22 cm^{-1}). This implies crystal regions with low impurities concentrations i.e. a higher degree of crystallinity[29,30,31]. Nemanich et al.[17] have shown that the FWHM for the high frequency E_{2g} mode is inversely proportional to the crystallite sizes which are considered to be related to the thickness of the nanowalls as follows:

$$\Gamma_{1/2} = 9cm^{-1} + 1420cm^{-1} / L_a(\text{Å}) \qquad (4.\ 12)$$

$\Gamma_{1/2}$ is the FWHM Lorentzian fit at the E_{2g} position which is 1367 cm^{-1}, while L_a is the average crystallite size.

This indicates that the h-BN/h-BN nanowalls are relatively well-crystallized and the crystallite size could be roughly estimated to 11 nm. By the way, the FWHM is slightly larger than for BN nanosheets deposited at high temperature (~800°C) using microwave plasma CVD (BNNSs-19 cm^{-1})[7], high temperature (~1900°C) CVD synthesized pyrolytic BN (16 cm^{-1})[26,32] and high temperature (1600°C-1700°C) synthesized BNNTs (13 cm^{-1})[15,28], but smaller than that of the

pyrolytic BN measured by Geick et al. (~30 cm^{-1})[2] and the BNNTs (27 cm^{-1})[33] synthesized at 1200°C.

According to Kobayashi et al.[31] the difference in average crystallite size measured via the dark field TEM images (thickness of nanowalls = 50 nm) and deduced from the Raman spectra (crystal size = 11 nm) could be explained by the formation of numerous nanocrystalline domains forming many "domain boundaries" in the h-BN nanowalls.

Figure 4- 20b shows the evolution of grain sizes as a function of the % H_2 gas flow. For granular structured films i.e. films grown with 0%, 36% of H_2, more H_2 is added to the Ar/N_2 plasma, smaller are grains and their E_{2g}^2 peak position shifts are constant at around 1367 cm^{-1}. Except for h-BN nanowalls which grain sizes are independent to the %H_2 and their E_{2g}^2 peak position shifts have lower value varying from 1363.5 to 1365 cm^{-1}.

Furthermore, the sharp boric acid (B $(OH)_3$) defect peak at 500 and 879 cm^{-1} is completely removed in spectra taken on the stoichiometric samples (5% H_2), whereas these appear clearly from other samples grown with different %H_2 as shown in Figure 4- 20a. Indeed, B $(OH)_3$ is known to form very easily from the spontaneous reaction of boron and boron oxide (B_2O_3) with moisture and oxygen.

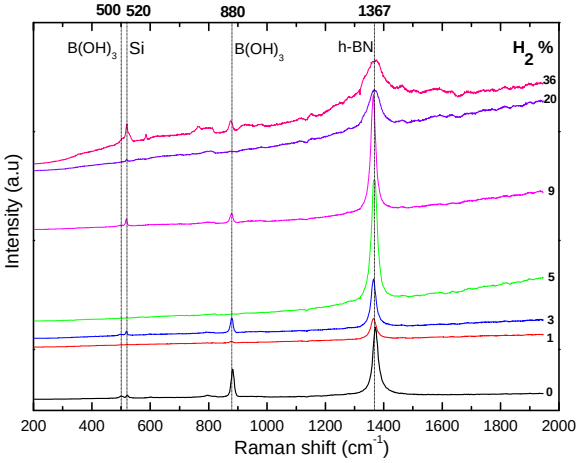

(a)

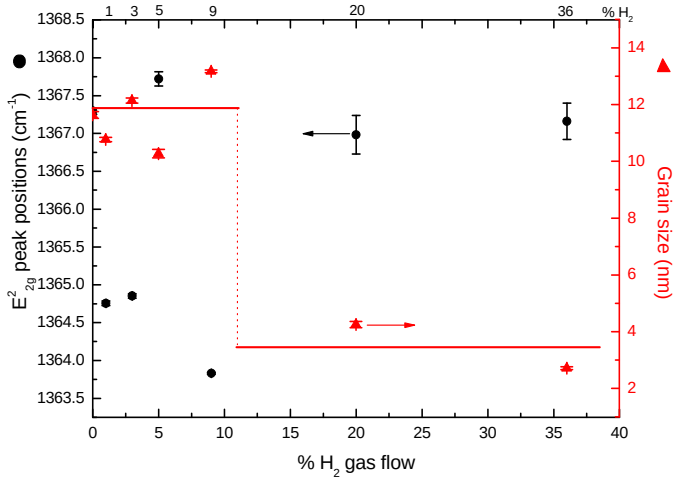

(b)

Figure 4- 20: UV-Raman spectrum (266nm) of 1.5 µm thick BN(NWs) samples at the laser power of 30 µW (a) and the shift of the E_{2g}^2 peak positions and grain size related to % H_2 gas flow (b).

Its formation in the reactor can possibly be explained as follows: Upon sputtering by the RF magnetron plasma, the h-BN crystallites of the target decompose above a certain plasma temperature (around 2700K) into nitrogen gas and liquid boron which becomes finally gaseous[34]. Boron oxide contained in the binder of the target also decomposes above 2133 K to give rise to gaseous boron[34]. This boron gas phase is then quenched in the synthesis chamber and condenses into small liquid droplets that either react with nitrogen to produce BN nanowalls or simply solidify. In the latter case, the resulting boron particles transform progressively into boric acid by contact with air after opening the reaction chamber. Boric acid could be also coming from the heating of the analyzed surface (BN films) by the UV laser power source (diameter of the spot, d=1.6 µm) during measurement. In Figure 4- 21a, h-BN peak is more intense and boric acid peak disappears completely for sample@0%H_2 using a power of laser beam at 9 nanowatts (Flux= 6x10^{21} photons.m^{-2}.s^{-1}). Whereas, for the same laser power applied on sample@5%H_2, the spectrum reveal the weakness of the signal at 1367 cm^{-1} with no trace of boric acid (Figure 4- 21b). When the power reached 30 µW (Flux= 2x10^{25} photons.m^{-2}.s^{-1}), the higher h-BN intensity peak (E_{2g}^2) is clearly seen without the presence of B $(OH)_3$ (Figure 4- 20a).

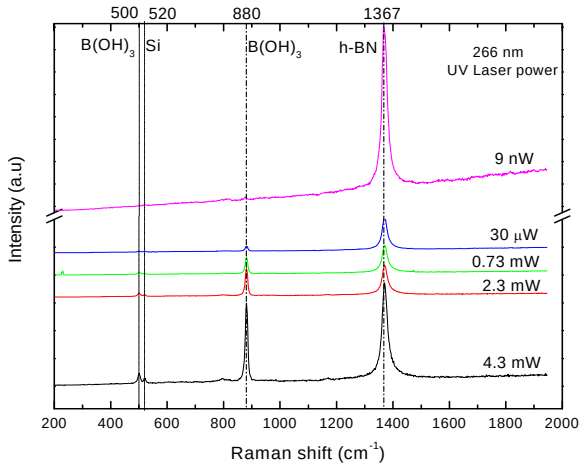

(a)

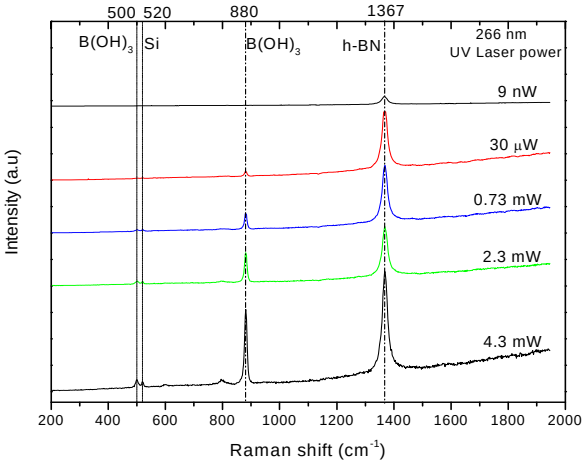

(b)

Figure 4- 21: UV-Raman spectrum (266nm) of 1.5 µm thick sample@0% H_2 (a) and sample@5%H_2 (b) at different power of the UV laser source.

4.3.1 Substrate dependence

Thin h-BN films grown with 5 % H_2 were deposited also on quartz (0001) substrates. To analyze the influence of the substrate on the quality of h-BN film, micro-Raman spectra excited with photons of 266 nm are shown in Figure 4-22a. Figure 4- 22b shows the 473 nm, 532 nm, 633 nm and 785 nm laser lines which confirm a good crystalline structure (FWHM=22 cm^{-1}) of h-BN materials with a narrow peak at 1368 cm^{-1}.

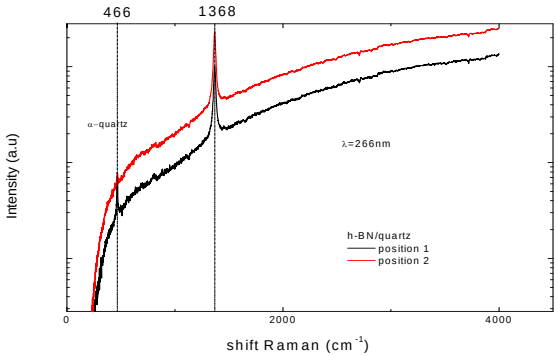

(a)

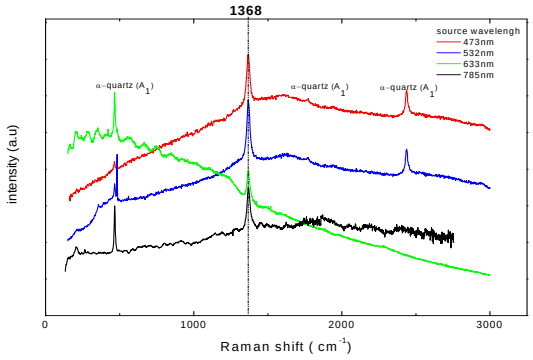

(b)

Figure 4- 22: UV (a) and visible Raman spectra (b) of h-BN films deposited on quartz substrates. The α-quartz peaks are located at 465, 1772, 2437 cm^{-1}.

With the same growth conditions i.e. 5% H_2 and according to equation (4. 12), the grain size is slightly different when deposited on quartz (0001) substrates

(thickness=12.5 nm) than, deposited on Si (100) substrates (thickness=11.7 nm), but the difference when falls within the expected error.

4.4. Summary Table

Table 4- 3 summarizes results reported in literature. Obviously, h-BN nanowalls can be assigned to their own IR and Raman features located between the polycrystalline h-BN, h-BN and BN nanosheets (deposited at 800°C).

	Microstructure	Growth temperat-ure	FTIR "TO (LO)"		RAMAN		Ref
			A_{2u} (cm^{-1})	E_{1u} (cm^{-1})	E_{2g} (cm^{-1})	FWHM (cm^{-1})	
CVD	Turbostratic BN (t-BN)	800-950°C	795-810 800	1396 _	1368 1367	_ _	35,37
	Pyrolitic BN	>1600°C 1200°C	760-790 767(783) 783(828)	1367 1367(1510) 1367(1610)	1366-1367 _ 1366-1370	16 30 _	17,26,32,35 2,16,18 2,18,36
	Polycrystalline (h-BN) h-BN	_ _	811 817	1377 1370	1367-1374 1366-1370	_ _	7,14,16,17 2,17
	h-BN nanoribbons	_	818	1367	1366-1370	_	7,14
	BN nanotubes	1600-1700°C 1500°C	820 800 794	1366 1372 1380	1370 _ _	13 _ 27	7,14,15,17,20,29 18 18,33
	BN nanosheets	800°C	811	1350-1520	1366	19	7
PVD	BN nanowalls	*<600°C	818	1381(1542)	1367-1368	21	This work

*: RF plasma temperature measured with a pyrometer gun on MS-PVD system.

Table 4- 3: Comparison of FTIR and Raman results reported in literature.

4.5. UV-Vis-NIR Spectroscopy

4.5.1 Introduction

The refractive indices (n and k) and absorption coefficient (α) were analyzed by transmission spectra using the Lyashenko and Miloslavski[38] method. This method was simplified by the procedure suggested by Swanepoel[39,40], which takes into account the profile of the layers. This procedure allows the accurate determination of the average thickness, thickness variation and the refractive indices of the film[41].

The data reported so far for the anisotropic thin BN film refractive indices vary from 1.6 to 2.2[42-45]. According to Schubert et al.[25], this variation is generally regarded as being due to the film porosity or the existence of both phases i.e. amorphous-BN (a-BN) and h-BN grains in the same layer. Moreover, the same authors describe BN as a material intrinsically anisotropic with an averaged isotropic h-BN refractive index n~ 1.88[42], depending on the microstructure i.e the film can appear isotropic or anisotropic. The isotropic hypothesis on 3 different categories of h-BN samples was defined in accordance with SEM and RBS studies i.e. the granular structure (samples A and B with 0% and 36% H_2), the unknown structure (sample C with 20% H_2) and the nanowall structures (samples D to G with 1, 3, 5, 9% H_2).

All thin films were deposited on fused silica substrates. Measurements were made in normal incidence transmission. All samples labeled A, B, C, D, E, F, G were duplicated with thicknesses of around 1.5 µm and 200 nm leading to 2 respective groups noted as (A_1, B_1, C_1, D_1, E_1, F_1, G_1) and (A_2, B_2, C_2, D_2, E_2, F_2, G_2) in order to check their optical constants during the growth.

Moreover, the ordinary refractive index (n_0) for bulk h-BN is assigned to n_0=1.65[46,47] (linear polarization parallel to *c* axis //c) and extraordinary refractive index (n_e) is n_e=2.13-2.17[44,46] (linear polarization perpendicular to *c* axis $\perp$ c). Depending on the intrinsic *h*-BN refractive indices n_o and n_e and the solid angle spread Θ (see equation 4.8), the thin film appears optically positive ($n_{e,\ eff} > n_{o,eff}$) or negative ($n_{e,eff} < n_{o,eff}$) with $n_{0,eff}^2 = \varepsilon_{x,eff} = \varepsilon_{y,eff}$ and $n_{e,eff}^2 = \varepsilon_{z,eff}$ ($n_{e,\ eff}$: extraordinary effective refractive index; n_0: ordinary effective refractive index).

4.5.2 Determination of optical constants and optical gap of granular structured films (samples A and B)

4.5.2.1 Conditions

- Films grown with addition of 0% H_2 (A) are considered almost stoichiometric (N/B~1), and 36% H_2 (B) considered as under-stoichiometry with both carbon and oxygen non negligible according to RBS spectra.
- Films thickness: A_1=1.8 µm, B_1=1.1 µm, A_2=200 nm, and B_2=181 nm.

Figure 4- 23a and Figure 4- 23b show the transmission curve in the normal incidence of A_1 film and B_1 film respectively. Due to multiple reflections inside the layer, the interference fringes are observed in the UV-Vis-NIR frequency range allowing to estimate the T_{min} and T_{max} envelopes needed to calculate the optical constant and their film thicknesses.

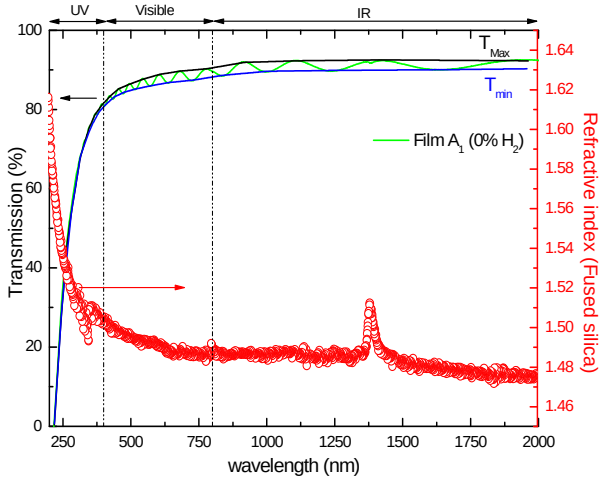

(a)

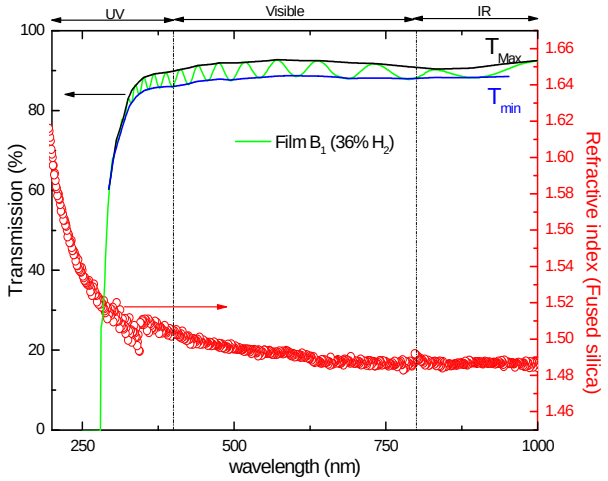

(b)

Figure 4- 23: Transmission spectrum and derived refractive index (fused silica) of 1.8 µm thick film A_1 (0% H_2) and 1.1 µm thick film B_1 (36% H_2) on fused silica (a) and (b), respectively.

The refractive index of fused silica (s) was determined using transmission spectrum of fused silica substrate (T_s) as follows:

$$T_s = \frac{2s}{s^2 + 1} \qquad (4.\ 13)$$

4.5.2.2 Results and discussion

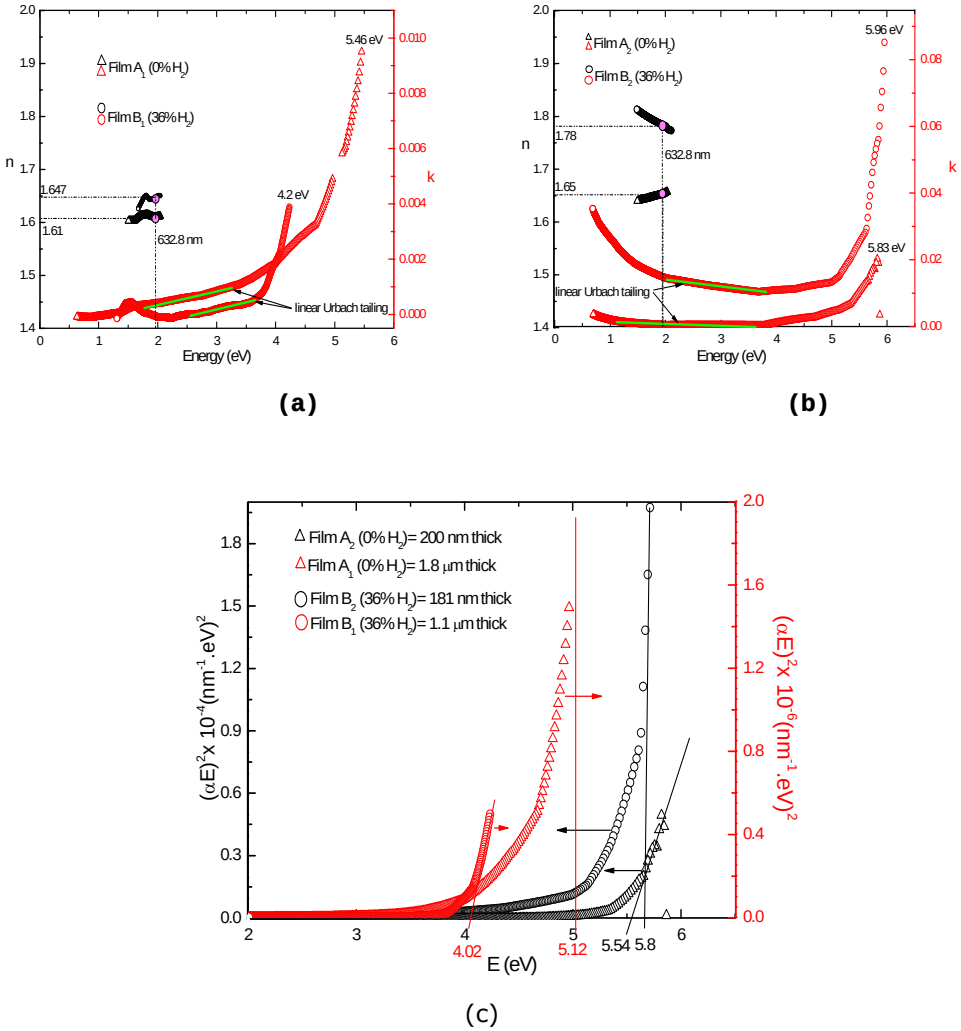

Figure 4- 24: Variation of the refractive index n and the extinction coefficient k as a function of photon energy for samples A_1 ($0\%H_2$-1.8 μm thick) and B_1 ($36\%H_2$-1.1 μm thick) (a) A_2 ($0\%H_2$-200 nm thick) and B_2 ($36\%H_2$-181 nm thick) (b). Their optical band gap (c).

In Figure 4- 24a and Figure 4- 24b, the refractive indices of A and B films at λ=632.8 nm are as follows:

- n_{A1}=1.61; n_{B1}=1.647; n_{A2}=1.65; n_{B2}=1.78.
- k_{A1}=3.74x10^{-4}; k_{B1}=0,k_{A2}=4.53x10^{-4}, k_{B2}=0.015.

The averaged isotropic h-BN refractive index is n_{B2}=1.78, and is very close to the $n_{h\text{-}BN}$ =1.88 reported by Mckenzie et al.[42] Some values could be related to the ordinary refractive index n_0= n_{A1}=n_{B1}=n_{A2}=1.65 of the h-BN bulk material confirming that the c-axis is lying to the substrate surface as confirmed by the FTIR spectra (see in Figure 4- 17) and TEM (chapter 3,section 3.3.3). The analysis of the spectrum depending on the energy of incident photons reveal that the thinner the film is higher is, the higher the refractive index is. Films grown with 36% H_2 (compared to 0% H_2) show a higher refractive index (n) and a lower extinction coefficient (k) which is not yet understood.

A narrow absorption line with its peak centered at 242 nm (A_1), 224 nm (A_2), 308 nm (B_1) and 214 nm (B_2) are deduced from the relationship between the absorption coefficient (α) and the extinction coefficient (k) as follows:

$$\alpha = \frac{4\pi k}{\lambda} \qquad (4.\ 14)$$

This corresponds to the optical gap (Tauc gap)[48] of 5.12 , 5.54, 4.02 and 5,8 eV respectively (see in Figure 4- 24c). These energies are smaller than the reported one for h-BN micro-sized crystals[14], which is centered at 6.15 eV. Such a shift in the granular h-BN samples is attributed to the saddle point transition in the band structure of the h-BN[49]. It is well-known that the relationship between the absorption coefficient (α) near the absorption edge and the optical band gap (E_g) for "direct" interband transitions obeys to the following relation[50]:

$$(\alpha E)^2 = A(h\nu - E_g) \qquad (4.\ 15)$$

Where A is a parameter associated with valence and conduction bands, and $h\nu$ is the photon energy. The direct band gap for the absorption edge can be obtained by extrapolating the linear portion of the plot $(\alpha h\nu)^2 - h\nu$ to α=0 (Tauc plot). This gives Eg approximately between 4 and 6 eV as the composition changes due to impurities with different thicknesses (see in Figure 4- 24c).This can be also influenced by porosity because thicker films have a smaller gap. The optical band gaps fit well with the extinction coefficient $\left(k = \frac{\alpha\lambda}{4\pi}\right)$ values leading to the consistency of the Swanepoel calculation model[39,40].

As shown in Figure 4- 24, a broad continuum is observed from 1.5 eV to 4 eV. According to Hoffman et al.[26], the 1-4 eV continuums are assigned to the transitions involving impurity and defect states distributed throughout the gap.

This continuum (Urbach tail) reported by Ong et al.[51] , and represented in Figure 4- 24a and Figure 4- 24b, brings information about the type of the possible transitions within the band gap. If the Urbach tail determined from log α is linear, that means the transition is indirect otherwise the transition is considered as direct[6]. This should be taken into account in the optical gap calculation (cf. chap4, 4.6.6). Above 4 eV the absorption rises abruptly due to intrinsic interband transitions ($\pi \rightarrow \pi$) across the insulating band gap[26,49,52,53]. Note that, from Figure 4- 24a and Figure 4- 24b, we display n and k on a linear energy scale to show clearly the separation of the impurity absorption and the $\pi \rightarrow \pi$ threshold[26].

4.5.3 Determination of the optical constants and the optical gap of the unknown structure films (sample C)

Figure 4- 25 shows the UV-Vis-NIR absorption spectrum of the unknown structure films i.e. films of BN under stoichiometry grown with 20% H_2. Figure 4- 25a and Figure 4- 25b show optical absorption spectra for the 1.4 µm film thick (C_1) and the 222 nm film thick (C_2), respectively.

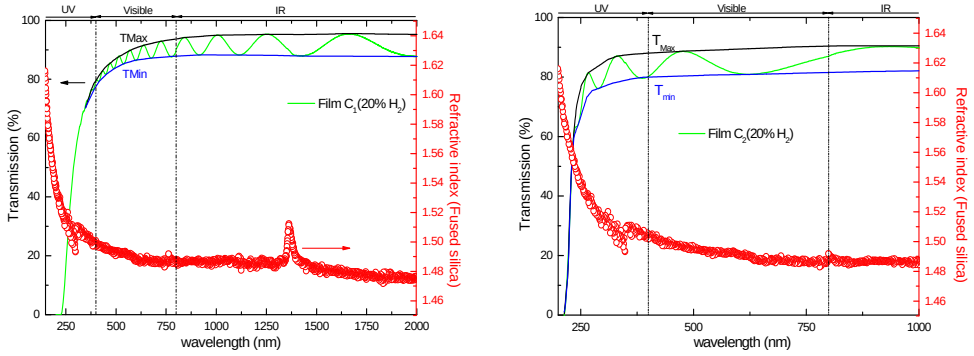

Figure 4- 25: Transmission spectrum of 1.4 µm thick film C_1 (20% H_2) and 222 nm thick film C_2 (20% H_2) on fused silica (a) and (b), respectively.

In these figures, the UV-Vis-NIR spectrum responses are illustrated by their extremum T_{max} and T_{min}. Thicknesses and optical constant of films will be deduced together with the refractive index of the fused silica substrate.

Figure 4- 26a shows the value of refractive indices at λ=632.8 nm, which range from n=1.68 (k=10^{-4}) close to the fundamental ordinary refractive index n_0=1.65 for film C_1 to n=1.81 (k=0.0025) for film C_2 (averaged isotropic h-BN

refractive index). Those results are confirmed by the Figure 4- 26b, with the determination of the threshold band gap value. Unlike the granular structure optical absorption behavior, the thicker the films, the larger the values for n and k become.

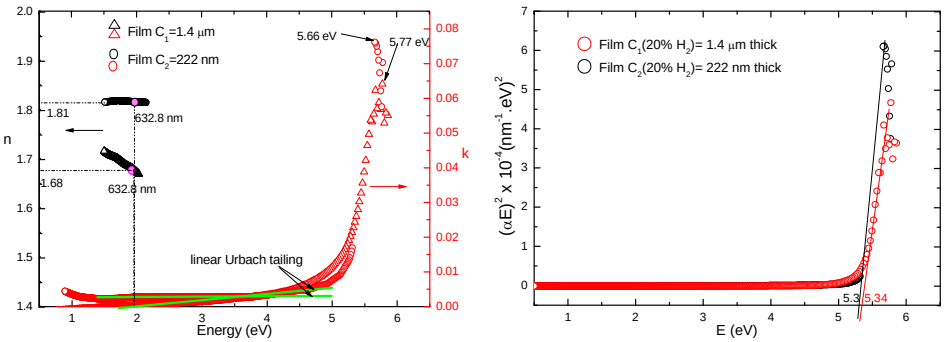

(a) (b)

Figure 4- 26: Variation of the refractive index n and the extinction coefficient k as a function of photon energy for samples C_1 (20%H_2-1.4 µm thick) and C_2 (20%H_2-222 nm thick) (a). Their optical band gap (b).

4.5.4 Determination of optical constants and optical gap of nanowall structure films (samples D, E, F and G)

Optical investigations of the h-BN nanowalls films have not been exhaustive and further studies are still needed.

As discussed in chap 3.3, nanowalls start to grow from 0.5 %H_2 to <20%H_2 added to the plasma of Ar/N_2. D_1 (D_2), E_1 (E_2), F_1 (F_2) and G_1 (G_2) are marked as BN films with 1, 3, 5, 9 %H_2 with around 1.5 µm (200nm) film thickness respectively.

From Figure 4- 27a, the refractive index at 632.8 nm is estimated at 2.17 (D_1), 1.84 (E_1), 1.59 (F_1) and 1.62 (G_1), respectively. The analysis of spectra at the edge of the absorption level reveals that the optical gap (D) is lower than the average of all samples studied with its shoulder at around 2.5 eV, 3.15 eV and 4.2 eV related to impurities or structural defects[26]. RBS analysis has shown that the D_1, E_1 films are sub stoichiometric with respect to boron with N/B=1.23, N/B=1.08 respectively. Whereas F_1 (5%H_2, 1.4 µm thick) with a stoichiometry N/B=1 corresponds to the minimum n (1.59) and maximum k (0.08) at 5.71 eV. It is regarded as being due to the film porosity or to the existence of both

phases i.e. the mixture of amorphous BN (a-BN) and h-BN grains in the same layer. Note that G_1 film is sub stoichiometric with respect to nitrogen with N/B=0.94. D_2, E_2, G_2 have better optical quality films than D_1, E_1, F_1, G_1 due to their higher energy level reached at a maximum k as shown in Figure 4- 27b. Thus revealing again that the impurities or structural defects depend on the film thicknesses. Also, the fact that they are more porous than samples A,B and C could justify that the values are lower and worse.

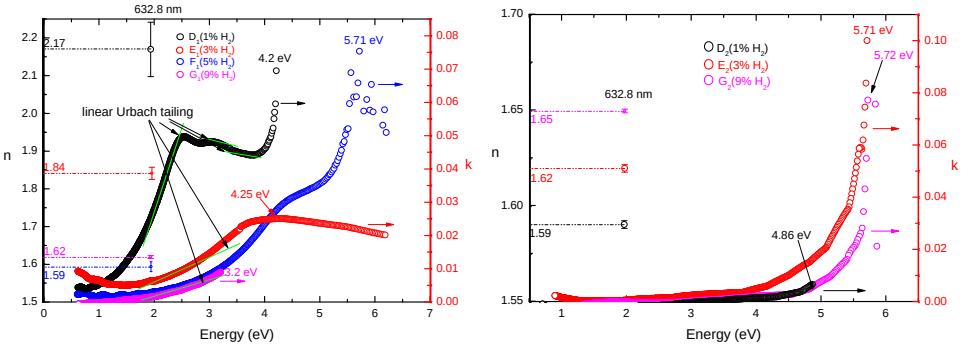

Figure 4- 27: Variation of the refractive index n and the extinction coefficient k as a function of photon energy for samples D_1 (1%H_2-1.5 µm thick), E_1(3%H_2-1.6 µm thick), F_1(5%H_2-1.4 µm thick) and G_1(9%H_2-1.5 µm thick) (a). D_2 (1%H_2-156 nm thick), E_2 (3%H_2-185 nm thick)and G_2 (9%H_2-174 nm thick)(b).

For clarity,

Table 4- 4 summarizes the results for these 3 different categories of h-BN samples.

Structure	Samples		%H_2	Thickness (nm)	n (633 nm)	k (633 nm)
Granular	A	A_1	0	1800	1.61	$3.74x10^{-4}$
		A_2		200	1.65	$4.53x10^{-4}$
	B	B_1	36	1100	1.647	0
		B_2		181	1.78	0.015
Unknown	C	C_1	20	1400	1.68	$1.1x10^{-4}$
		C_2		222	1.81	0.0025
Nanowall	D	D_1	1	1500	2.17	0.02
		D_2		156	1.59	0
	E	E_1	3	1600	1.84	0.006
		E_2		185	1.62	$4.19x10^{-4}$
	F	F_1	5	1400	1.59	0.003
		F_2		-	-	-
	G	G_1	9	1500	1.62	0.002
		G_2		174	1.65	0.08

Table 4- 4: Summary of the optical constant from different h-BN films structure.

Note that, for h-BN nanowalls the uncertainties of the refractive index are not negligible. That leads to difficult physical interpretation of the films. In order to reduce these disparities at λ=633 nm, the quality of films was improved by heating the substrate holder in the MS-PVD system. For that, the influence of the Si substrate temperature on the growth of the 5%H_2-200 nm thick h-BN/h-BN nanowalls films has been studied.

4.5.5 Influence of the Si substrate temperature to the quality of the h-BN/h-BN nanowalls films

4.5.5.1 Condition

The h-BN films are grown with 5% H_2 added to the Ar/N_2 plasma. The substrate holder is biased to reach temperatures from 200°C to 600°C. The thicknesses of all these films are around 200 nm.

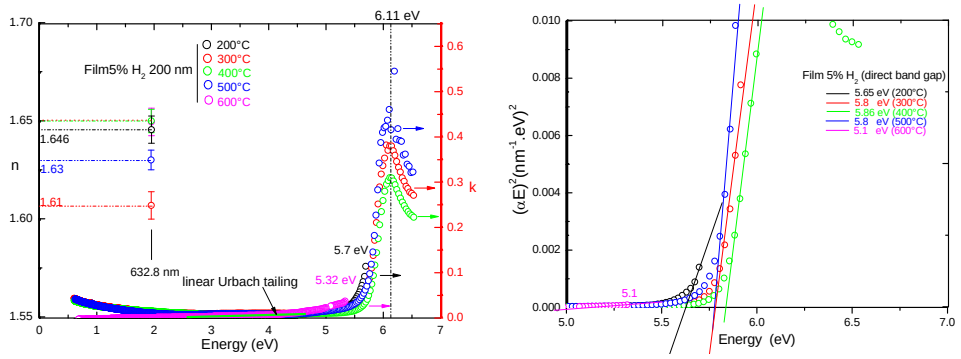

(a) (b)

Figure 4- 28: Variation of the refractive index n and the extinction coefficient k as a function of photon energy for 200 nm thick films grown with 5% H_2 at different substrate temperatures (a). Their optical band gap (b).

The role of the substrate heating during the growth process exhibits a constant refractive index as shown in Figure 4- 28a with a better optical gap and less impurities of the h-BN/h-BN nanowalls film when deposited between 400°C-500°C (Figure 4- 28b). For clarity, the results obtained from Figure 4- 28a and Figure 4- 28b were summarized in Table 4- 5.

Structure	Temperature (°C)	Thickness (nm)	n (633 nm)	k (633 nm)	Direct band gap (eV)
5% H_2 h-BNNWs F_2 series	200	d≤ 200	1.646	0	5.65
	300		1.61	0.011	5.8
	400		1.65	0.013	5.86
	500		1.63	0.010	5.8
	600		1.65	0	5.1

Table 4- 5: Summary of the optical constants and direct band gap from h-BN/h-BN nanowalls films grown at 5% H_2 with different substrate temperature.

Note that the refractive index at 633 nm from each samples (films 5% H_2 – 200 nm) are independent of the fused silica substrate temperature. However, the value of h-BN bulk material is achieved (n=1.65)[46,47].Moreover, their uncertainties at 633 nm are lower when the substrate temperature is fixed at 400°C. Note that the extinction coefficient (k) at 633 nm is relatively higher than samples at 300°C and 500°C. It gives the higher direct band gap (5.86 eV). Whereas the lower k values measured from samples at 200°C and 600°C give the lower direct band gap.

4.5.6 Optical gaps of h-BN nanowalls vs stoichiometry

In order to compare the optical band gap of the h-BN (NWs) films as a function of the % H_2 and their chemical composition, the results obtained by UV-Vis-NIR absorption spectroscopy and RBS are summarized in Table 4-6.

Samples	**D_2** <200°C	**E_2** <200°C	**F_2**=400°C	**G_2**<200°C
% H_2	1	3	5	9
Thickness	156	185	198	174
N/B	1.23	1.08	1	0.95
Eg (eV) direct	4.6	5.71	> 5.86	5.65
Eg (eV)	4	5.41	5.6	5.47
n (633 nm)	1.59	1.62	1.65	1.65

Table 4-6: Summary of several parameters for 4 h-BN nanowalls samples. N/B ratio was determined by RBS.

Figure 4- 29 shows the optical band gap energy as a function of the stoichiometry of the h-BN thin films from 3 samples studied (D_2, E_2, G_2). We can notice that more the films are sub stoichiometric, the more the value of the optical gap decreases. For thin films studied where we did not observe impurities by optical techniques, a maximum optical gap was deduced by the Tauc plot method either as direct transition[48] i.e. $E_g = \frac{(\alpha h\nu)^2}{h\nu}$ or as an indirect transition $E_g = \frac{\sqrt{\alpha h\nu}}{h\nu}$.

As shown in Figure 4- 29, F_2 sample, grown at 400°C, shows a good stoichiometry.

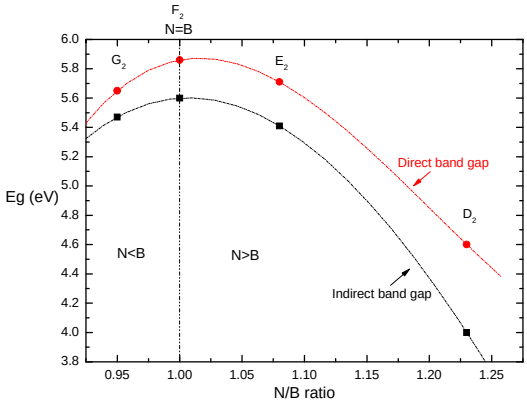

Figure 4- 29: Evolution of the (direct and indirect) optical gap of the films based on the chemical composition (stoichiometry)

4.5.7 Interpretation and conclusion

The variation of the optical gap as a function of the N/B ratio is discussed. First, one should describe how the density of electron states (DOS) was obtained by fitting the optical absorption spectra of amorphous B-rich boron nitride (BN_x). The proposed DOS model[51,54-56] is presented schematically in Figure 4- 30.

It shows two possible localizations of impurities in the band gap of h-BN[51]:

- Concentration of impurities gives deep energy levels inside the band gap. That leads to the formation of a Gaussian-shaped energy band. These G-band localized states are analogous to the case encountered for graphite. Here, this configuration is allowed only in the case where films are rich in nitrogen (BN_x, $x>1$), which correspond to the films excepted for G_2 film (BN_x , $x<1$),
- Concentration of impurities is near the conduction band (CB) and the valence band (VB) forming a continuum of energy states. These continuums are superimposed on the CB and VB bands so as to extend and form the "Urbach" tail states. This narrowing of the band gap leads to a decrease of the optical gap. Hypothesis: the crystal disorder could also lead to the tails but not yet proved.

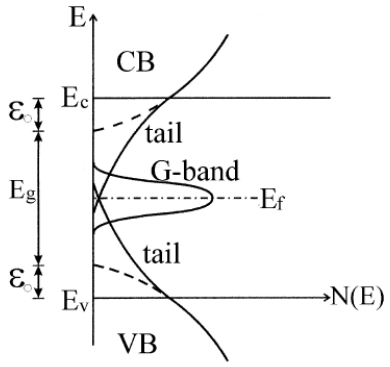

Figure 4- 30: DOS model used for analyzing the optical absorption spectra of the BN_x films with different N contents[51] .ε_0 is a parameter

As shown in Figure 4- 30, because of the lack of long-range order in the materials, tail states of the conduction and valence bands are expected to appear between the energy level E_v and E_c. The dashed lines represent the extensions of the valence band and conduction band. The separation between the intercepts of the two curves at the E-axis defines the optical band gap Eg.

More details about different possible transitions within h-BN can be found in refs[26,51,57].

4.6. Cathodoluminescence measurements (CL)

4.6.1 Theory – CL in h-BN

h-BN is considered as a promising candidate for wide range of applications, e.g. ultraviolet (UV) light emitters. The recent work by Watanabe *et al.*[58,59] have pointed out an exceptional radiative efficiency leading to a strong luminescence at 215 nm (5.76 eV). It was concluded that a lasering effect with a yield of luminescence is higher than its cubic counterpart.

On a theoretical level, recent calculations show that the h-BN is an indirect wide band gap semiconductor (6 eV) with significant excitonic effects[60-64]. Excitons are defined as pseudo-particles which are the source of many well-defined electronic levels (excitonic levels). There exist two types of excitons[65] as shown in Figure 4- 31:

- Wannier excitons: where the orbital has a large radius, extending over several interatomic distances. The electron and the hole can move freely throughout the crystal. These are delocalized excitons.
- Frenkel excitons: the radius of excitons is of order of the interatomic distance, i.e. the electron and the hole can be localized around an atom. This type of exciton is formed in wide bandgap semiconductors with low dielectric constant.

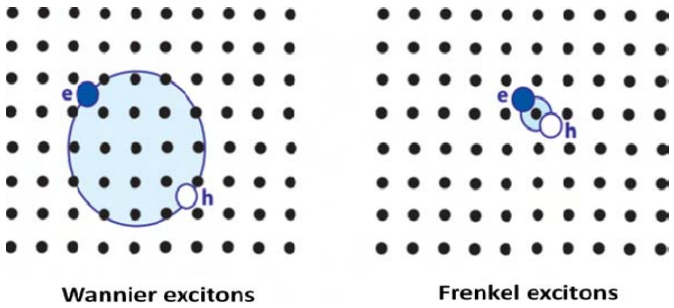

Figure 4- 31: Representative diagram of the Wannier and Frenkel excitons in a crystal[65].

Recently, theoreticians[60,61,62] and experimentalists[66] agreed on the Frenkel nature of exciton in the h-BN films.

4.6.2 Results and discussions

To further understand the opto-electronic properties of the h-BN nanowalls, films prepared with 5% H_2 were investigated by CL spectroscopy at 10K. For both the 200 nm and the 1.5 µm thick films, the CL spectra (see in Figure 4- 32a2) are dominated by a broad band around ~ 4 eV. As observed on bulk h-BN[67], this band is structured with α, β, γ peaks superimposed on the top of a continuous broadband emission centered at 3.9 eV (i.e. 318 nm). These observations have been attributed to the superimposed deep defect emission and donor acceptor pair (DAP) recombination by the presence of carbon or oxygen impurities[68]. The excitonic recombination in the near band gap region are less intense, and not even detectable in the 200 nm film thick, which indicates the lower degree of h-BN nanowall crystallization during the first stage of their growth. This lower radiative efficiency of the first hundreds of nanometer of the h-BN nanowall films is further confirmed on the thicker sample where CL images show overall lower luminescence intensity close to the silicon substrate (Figure 4- 32a1 and Figure 4- 32b1).

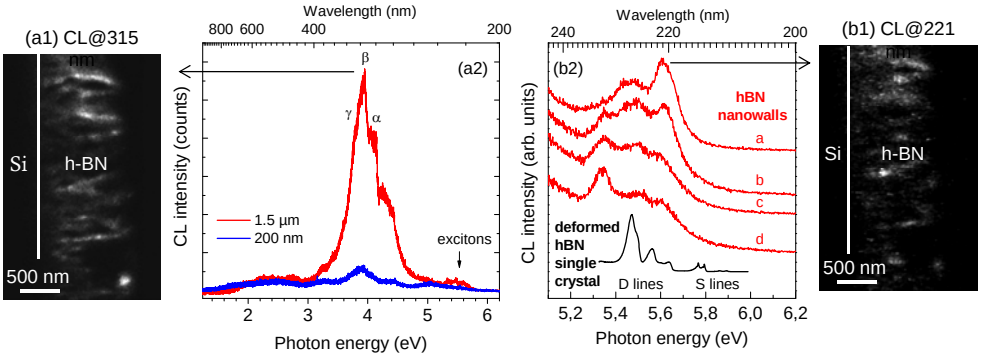

Figure 4- 32: Monochromatic CL image at 318 nm taken on a 1.5 µm thick h-BN nanowall film deposited with 5 % H_2 (a1). CL spectra taken on 200 nm thick (blue color, bottom curve) and 1.5 µm thick (red color, top curve) h-BN nanowall films deposited with 5 % H_2 (a2). The free excitonic emission region from 1.5 µm thick h-BN nanowalls film is compared to a h-BN single crystal (b2). Monochromatic CL image at 221 nm taken on a 1.5 µm thick h-BN nanowall film deposited with 5 % H_2 (b1)

The small electron beam size of the nano CL (~4 nm for this study) allows to record spectra from different areas of the nanowall films with a good spatial resolution, as illustrated on the monochromatic CL images where individual h-BN nanowalls can be observed (Figure 4- 32a1 and Figure 4- 32b1). Figure 4- 32b2 shows four spectra taken from different nanowalls randomly localized. Their near

band edge luminescence consists of three main components at 5.33, 5.47 and 5.61 eV, with variable intensities from one nanowall to another. From the excitonic point of view, 50 nm thick h-BN nanowalls may be seen as the bulk because of the high spatial localization of the Frenkel excitons. As a consequence, the h-BN nanowalls are compared with a high quality HPHT bulk h-BN crystal. As shown in ref.[66], excitons in h-BN are either self-trapped (S-lines) or trapped on structural defects (D-lines). In case of low structural defect content, the S-line group dominates, while after defect-induced generation by plastic deformation the D-line group dominates the excitonic spectrum[69-71]. In the h-BN nanowalls, one can observe that the excitonic emissions are much broader, indicating a lower degree of crystalline order. Following the comparison with bulk h-BN the 5.47 eV and the 5.61 eV lines are tentatively attributed to h-BN excitons trapped on structural defects (D-lines), in good agreement with the TEM-CL cross analysis by Jaffrennou *et al.*[72]. The 5.33 eV emission may be related to the DAP transitions as proposed by Museur *et al.*[73].

To sum-up, the luminescence properties of h-BN nanowalls are dominated by a broad impurity band near 4 eV, which is also observed in the bulk h-BN, and is possibly related to the C and O impurities. The recombination of excitons from h-BN nanowalls is consistent with the features of the bulk h-BN in the presence of structural defects, grain boundaries or impurities.

Making use of nano CL, h-BN excitonic luminescence at 5.61 eV (221 nm) and defect band luminescence related to impurities at ~ 3.9 eV (318 nm) are observed. Even if the nature of these excitonic recombinations in the h-BN nanowalls is not completely clear yet, it could be due to the excitons trapped at structural defects on the h-BN film.

4.7. Porosity of h-BN/h-BN nanowalls

In order to determine the porosity of the thin h-BN films in function of the refractive index and thickness, two different techniques were proposed. In parallel, films were studied using the specular reflectance technique and so-called m-lines technique at the FOTON UMR-CNRS laboratory (Lannion-France) under the supervision of Dr. Joël Charrier.

4.7.1 Results and discussion (specular reflection technique)

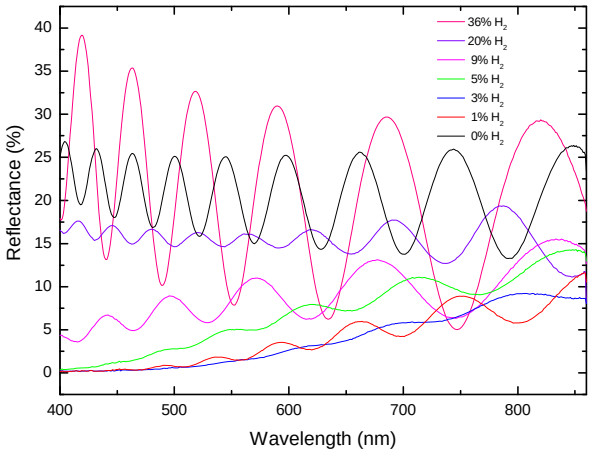

Figure 4- 33: Reflectance spectra of h-BN layers on Si substrates at different H_2 gas flow from 0% to 36%.

As shown in Figure 4- 33, the collapse of the reflectance for higher H_2 flows is probably due to the layer roughness. The roughness is measured with a Dektak3ST surface profiler and its thickness with the cross-sectional SEM. The results of different samples are summarized in Table 4-7.

% H_2	Thickness (nm)	Density ($g.cm^{-3}$)	Roughness-RMS (nm)
0	1.5	1.16	138
1	1.5	1.06	205
3	2.0	0.75	278
5	**1.5**	**0.96**	**318**
9	1.7	0.78	200
20	1.4	1.96	102
36	1.1	2.09	51

Table 4-7: Thickness, roughness and mass density of h-BN/Si layers.

This table shows the density and roughness of different films from 0% to 36 % H_2 addition. The density (per cm^3) and roughness of matters inform about the property of nanowalls which is related to their densities (per cm^2). Films present the lowest densities and the highest roughnesses are deposited with 3-5% H_2 addition (nanowalls). Further informations to discuss these results should be related to the porous nature of the films (see chapter 3, Figure 3-15) and the refractive index.

Figure 4- 34 shows some examples of good agreement between the experimental and theoretical reflectance spectra. This model is used to calculate the effective index of refraction of the mixture medium composed by air and BN, then deducing the thickness of the h-BN thin film layer.

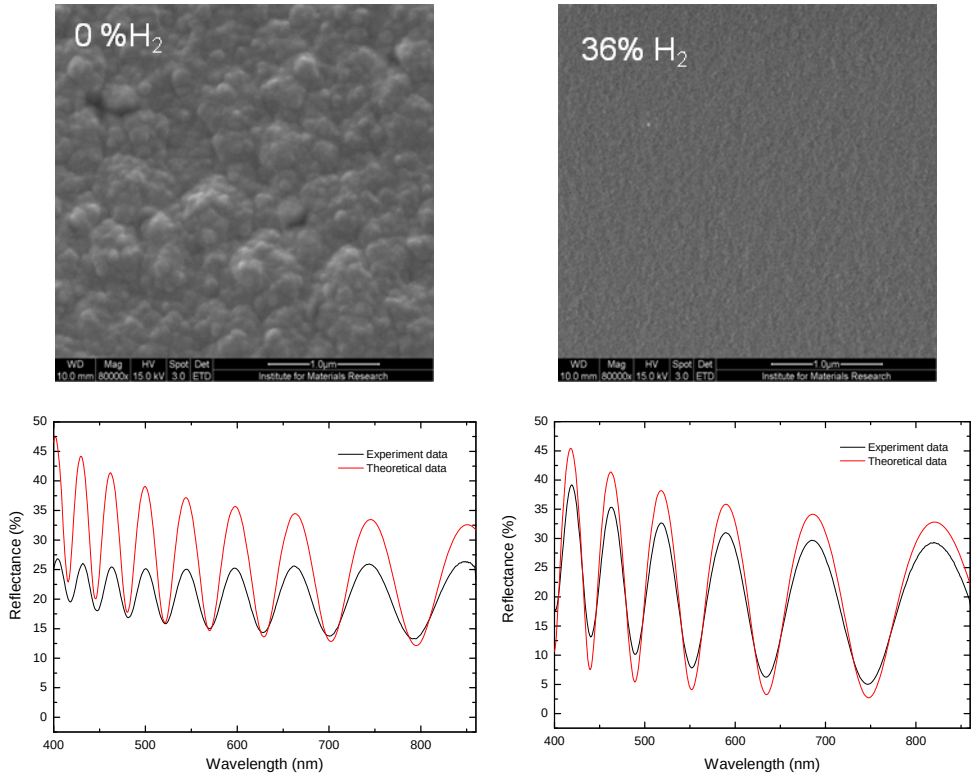

Figure 4- 34: Theoretical and experiment spectra of h-BN granular structures grown with 0% H_2 (a) and 36% H_2 (b) with their corresponding SEM images.

The fitting to the experimental spectrum allows the determination of the dispersion curves. Based on this method, the evolution of the refractive index of the porous h-BN sample as a function of the wavelength can be determined, as shown in Figure 4- 35. The films with 5% H_2 addition have the lowest refractive index and the highest porosity for films with nanowall structure. Their longer and their more spaced nanowalls have the highest N/B height ratio (see chapter 3, table 3.3) and therefore have the lowest impurities compared to other samples.

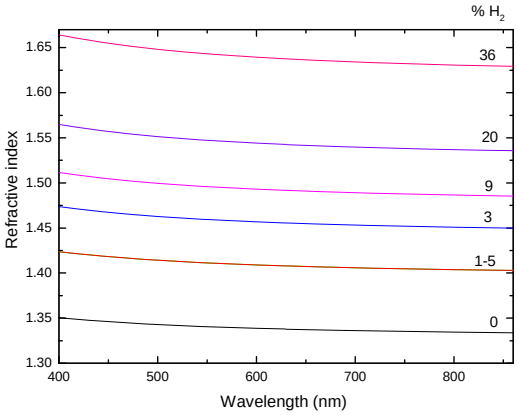

Figure 4- 35: Refractive index of h-BN samples deduced by the theoretical model in function of %H_2 gas flow. Note that no difference in the graph between films grown with 1%H_2 and 5%H_2.

A new set of deposited h-BN/Si (100) films were performed to confirm the roughness measurement and film thicknesses are measured with Fourier transform infrared (FTIR) spectroscopy using the E_{1u} stretching mode area at 1380 cm^{-1}.The air-volume fraction, the thickness of the samples and the refractive index at 633 nm are reported in Table 4- 8.

%H_2	**thickness (nm)**	**Porosity (%)**	**Refractive index at 633 nm from Bruggeman model[74,75]**	**Indice at 633 nm (m-lines)**
0	2.2	66	1.338	1.320 (thickness = 2258 nm)
1	1.9	60	1.408	-
3	1.9	56	1.455	-
5	1.5	60	1.408	-
9	1.3	53	1.491	-
20	2.0	48.8	1.542	-
36	1.2	41	1.637	-

Table 4- 8: Characteristics of the layers deduced from the experimental reflectance data.

The deduced thicknesses (between 1.3 to 2.2 µm) are well confirmed by the FESEM measurements. Table 4-7 and Table 4- 8 are combined to check the uncertainty upon the ρ_{BN} determination. The ρ_{BN} /porosity ratio is compared to the density of ρ_{BN} powder without pores (2.1 g.cm^{-3}). The accuracy is estimated between 10%-20%.

The refractive index profile analysis reveals a behavior indicating an optical inhomogeneity of the deposited films with % H_2 (see in Figure 4- 36a). As noticed in literature[76], the refractive index at 633 nm is evaluated to be between (n~ 1.65)[77] and (n~ 1.88)[76,78]. A refractive index lower than 1.65 could be assigned to the presence of water (H_2O) within the film leading to the porosity[76].

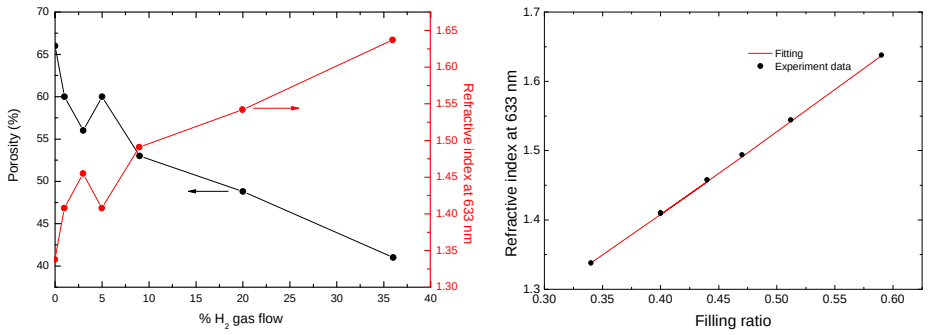

(a) (b)

Figure 4- 36: Porosity and refractive index of the h-BN films at 633 nm at different % H_2 (a) Refractive index at 633 nm in function of filling ratio =1-(0.01 x Porosity (%)) via experimental data (black sphere) and the subsequent fitting (red straight) (b).

The deposition starts for polycrystalline films (granular structure) of few nanometer thicknesses (see TEM, FTIR) with c-axis oriented with an angle Θ (see Figure 4.13a). When films become thicker and thicker, c-axis tend to be oriented in the substrate plane (// c). H_2 acts efficiently on sites in order to break the weak bonding (van der waals) and to build nanowalls. The sp^2 hybridization being slightly attack by H atoms. The remaining matter is not depending on the c-axis orientation but it depends on the porosity as observed in Figure 4- 36b where the refractive index is proportional to the filling ratio.

The mirror symmetry observed in Figure 4- 36a for the refractive index (at 633 nm) and the porosity, lead us to investigate the relationship between both and especially the filling ratio defined as 1-(0.01 x Porosity(%)).

As shown in Figure 4- 36b, a linear function is found between these two parameters as follows (see equation 4.16):

$$n_{633nm} = \left(1.2 \times filling \quad ratio\right) + 0.93 = \begin{cases} n_{air} \longrightarrow \ filling \quad ratio = 0 \\ n_o = 2.13 \longrightarrow \ filling \quad ratio = 1 \end{cases} \qquad (4.\ 16)$$

The refractive index of the h-BN films varied from n=1.34 to n=1.64 which corresponds to the ordinary refractive index of h-BN bulk material when c is normal to the Si (100) substrate surface[79]. Based on the model, one could note that the c-axis orientation depends on the filling ratio i.e. the porosity. Indeed, more films are filled of matter (less porosity), more the value of refractive index at 633 nm is approaching the ordinary refractive index as a consequence the c-axis is lying to the substrate surface. The thickness dependence on the c-axis orientation is described in the previous chapter 4. Moreover, in order to confirm the refractive index obtained from the specular reflectance, we used the complementary m-line technique which can also be applied for anisotropic layers.

4.7.2 Results and discussion (m-line technique)

The acquisition[80] and analysis of the data are performed by a Metricon-2010 prism coupler instrument at 633 nm and 1550 nm as shown in Figure 4- 37a and Figure 4- 37b, respectively.

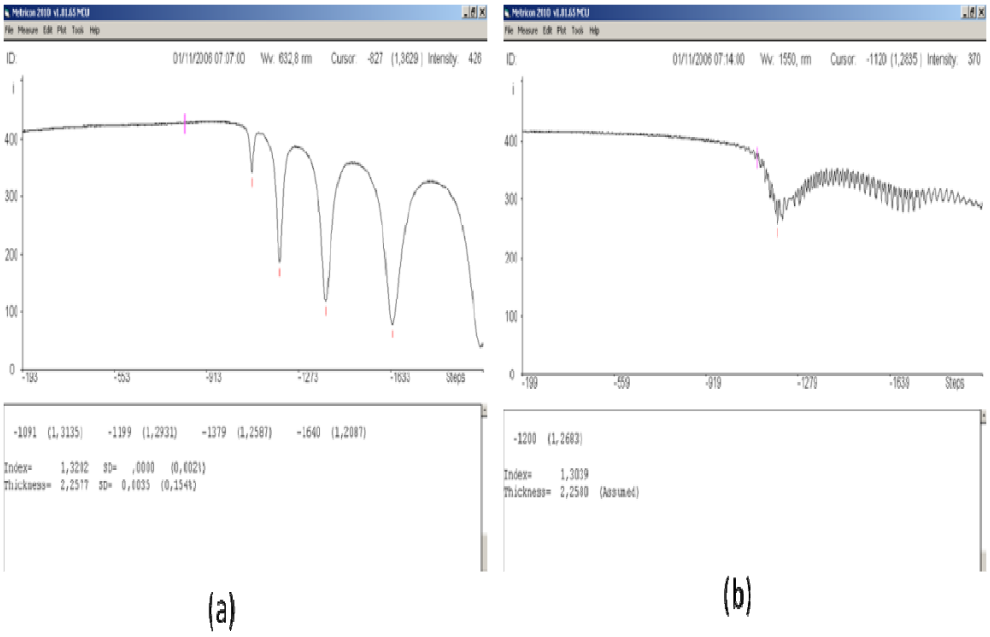

Figure 4- 37: Example of acquisition data from Metricon-2010 for sample 0% H_2 at 633 nm (a) at 1550 nm (b). The angular location of the first mode (dip) determines the film refractive index, while the angular difference between the modes determines the thickness.

The TE modes allow to obtain the ordinary refractive index (n_o) and the film thickness (d). Using the general dispersive equation, the extraordinary refractive index (n_e) is deduced by the TM modes. This technique is useful for films thicker than 633 nm at least, so that the waveguiding is possible given the incident laser beam wavelength.

An example is given for the TE polarization where refractive index is 1.32 and 1.30 at 633nm and 1553 nm respectively for 2.35 µm film thickness (Figure 4-37). For other samples, it was difficult to get results due to the scattering effect caused by roughness surface. These films didn't correspond to the planar waveguiding.

4.8. References

1. P.J. Gielisse, S.S. Mitra, J.N. Plendl, R.D. Griffis, L.C. Mansur, R. Marshall, E.A. Pascoe, Phys. Rev. **1967**, 155, 1039.

2. R. Geick, C. H. Perry, G. Rupprecht, Phys. Rev. **1966**, 146, 543-547.

3. G.L. Doll, "The Properties of Group III Nitrides" edited by JH Edgar INSPEC, IEE, London **1994**, 241-248.

4. T. Sato, Proc. Japan Acad. **1985**, 61B, 459.

5. J. Liu, Y.K. Vohra, T.J.T., S.S. Vagarali, Phys. Rev. B **1995**, 51 ,8591.

6. A. Soltani, PhD thesis « Croissance de films minces de nitrure de bore hexagonal et cubique par depot chimique en phase vapeur assisté par plasma :Caracterisations optiques et électriques » Université de Metz (**2001**).

7. J. Yu, L. Qin, Y. Hao, S. Kuang, X. Bai, Y.-M. Chong, W. Zhang and E. Wang, ACS Nano **2010**, 4 (1), 414-422.

8. R. T. Paine and C. K. Narula, Chem. Rev. **1990**, 90, 73-91.

9. M. A. Djouadi, Phd thesis **1993**, Université d' Orsay.

10. V. Mortet, PhD thesis « Croissance et caractérisation de couches minces de nitrure d'aluminium et de nitrure de bore cubique obtenues par pulvérisation triode » Université de Valenciennes et du Hainaut Cambrésis (**2001**).

11. S. Jäger, K. Bewilogua ,C. P. Klages, Thin Solid Films **1994**, 245, 50.

12. O. Madelung, "*Semiconductor: group IV elements and III-V compound"*. Series "Data in science and technology", ed. R. Poerschke, Springer - Verlag, Berlin **1991**, 164.

13. S. L. Rumyantsev, M. E. Levinshtein, A. D. Jackson, S.N. Mohammmad, G. L. Harris, M. G. Spencer, M. S. Shur "*Properties of Advanced Semiconductor Materials GaN, AlN, InN, BN, SiC, SiGe"* Eds. Levinshtein

M.E., Rumyantsev S. L., Shur M.S., John Wiley & Sons, Inc., New York **2001**, 67-92.

14. Z. G. Chen, J. Zou, G. Liu, F. Li, Y. Wang, L. Z. Wang, X. L. Yuan, T. Sekiguchi, H. M. Cheng and G. Q. Lu, ACS Nano **2008**, 2, 2183-2191.

15. C. Y. Zhi, Y. Bando, C. C. Tang, D. Golberg, R. G. Xie and T. Sekigushi, *Appl. Phys. Lett.* **2005**, 86, 213110.

16. E. Borowiak-Palen, T. Pichler, G. G. Fuentes, B. Bendjemil, X. Liu, A. Graff, G. Behr, R.J. Kalenczuk, M. Knupfer and J. Fink, Chem. Commun. **2003**, 1,82-83.

17. R. J. Nemanich, S. A.Solin, R. M. Martin, *Phys. Rev.B* **1981**, 23, 6348–6356.

18. Z. Dong, Y. Song**,** *J. Phys. Chem. C* **2010**, 114, 1782–1788.

19. W.A. de Heer, A. Chatelain, D. Ugarrte, *Science* **1995**, 270, 1179**.**

20. A. G. Rinzler, J. H. Hafner, P. Nikolaev, L. Lou, S. G. Kim, D. Tomanek, P. Nordlander, D. T. Cobert and R.E. Smalley, *Science* **1995**, 269, 1550.

21. M. Schubert, E. Franke, H. Neumann, T.E. Tiwald, D.W. Thompson, J.A. Woollam, J. Hahn, *Thin Solid Films* **1998**, 313-314, 692-696.

22. R. H. Lyddane, R.G. Sachs, E. Teller, *Phys.Rev*.**1951**, 59,673.

23. B. Harbecke,B. Heinz,P.Grosse, *Appl.Phys.A* **1985**,38,263-267.

24. D. W. Berreman, *Phys. Rev.* **1963**, 130, 2193.

25. M. Schubert, B. Rheinländer, E. Franke, H. Neumann, J. Hahn, M. Röder, F. Richter, *Appl. Phys. Lett.* **1997**, 70**(**14), 1819-1821.

26. D. M.Hoffman, G. L.Doll, P. C. Eklund, *Phys. Rev. B* **1984**, 30,6051–6056.

27. S. S. Ng, Z. Hassan, H. Abu Hassan, *Appl. Phys. Lett.* **2007**, 90, 081902.

[28] J. Wu, W. Q. Han, W. Walukiewicz, J. W. Ager, W. Shan, E. E. Haller, A. Zettl, *Nano Lett.* **2004**, 4, 647–650.

[29] K. Teii, S. Shimada, M. Nakashima and A.T.H. Chuang, *J. Appl. Phys.* **2009**, 106, 084303.

[30] M. Hamamatsu, K. Shiji, H. Amano and M. Hori, *Appl. Phys. Lett.* **2004**, 84, 4708-4710.

[31] K. Kobayashi, M. Tanimura, H. Nakai, A. Yoshimura, H. Yoshimura, K. Kojima and M. Tachibana, *J. Appl. Phys.* **2007**, 101, 094306.

[32] A. W. Moore, *Nature* **1969**, *221*, 1133–1134.

[33] S. Saha, D. V. S. Muthu, D. Golberg, C. Tang, C. Zhi, Y. Bando, A. K. Sood, *Chem. Phys. Lett.* **2006**, *421*, 86–90.

[34] R.Arenal, A. C. Ferrari, S. Reich, L. Wirtz, J. Y. Mevellec, S. Lefrant, A. Rubio, A. Loiseau, *Nano. Lett.* **2006**, *6*, 1812–1816.

[35] A. S. Rozenberg, Yu. A. Sinenko, N. V. Chukanov, *J. Mater. Sci.* **1993**, *28*, 5675-5678.

[36] T. Kuzuba, K. Eraa, T. Ishii, T.Sato, *Solid State Commun.* **1978**, *25*, 863–865

[37] H. Strakov, G. Hackl, N. Popovska, H.Gerhard, *Chem. Vap. Deposition* **2004**, *10*, 6.

[38] S.P. Lyashenko, V.K. Miloslavskii, *Opt. Spectrosc.* **1964**, 16,80-1.

[39] R. Swanepoel*; J. Phys. E: Sci. Instrum.*, **1983**, 16, 1214.

[40] R. Swanepoel; *J. Phys. E: Sci. Instrum.*, **1984**, 17, 896.

[41] J.B. Ramirez-Malo, E. Marquez, C. Corrales, J. Fernandez-Pefia, J. Reyes, P. Villares, R. Jimenez-Garay, *Mater. Chem. Phys.* **1996**, 44,186-189.

[42] D. R. McKenzie, W. D. McFall, H. Smith, B. Higgins, R. W. Boswell, A. Durandet, B. W. James, and J. S. Falconer, *Phys. Res. B* **1995**, 106, 90.

[43] S. L. Ren, A. M. Rao, P. C. Eklund, and G. L. Doll, Appl. Phys. Lett. **1993,** 62, 1760.

44. R. Poerschke and O. Madelung, "*Semiconductors Group IV Elements and III–V Compounds"* Berlin, Springer, **1991**.

45. M. J. Eremets, M. Gauthier, A. Polian, J. C. Chervin, J. M. Besson, G. A. Dubitskii, and Ye. Ye. Semenova, *Phys. Rev. B* **1995**, 52, 8854.

46. T. Ishii , T. *J.* Sato, *Cryst. Growth* **1983**, 61, 689.

47. T. Takahashi, H. Itoh, , M. Kuroda, *J. Cryst. Growth* **1981**, 53**,** 418.

48. J. Tauc, R. Grigorovici, A. Vancu, *Phys. Stat. Solidi* **1966**, *15*, 627-637.

49. A. Zunger, A. Katzir, A. Halperin, *Phys. Rev. B* **1976**, *13*, 5560–5573.

50. X. S. Peng, G. W. Meng, J. Zhang, L. X. Zhao, X. F. Wang, Y. W. Wang, L. D. Zhang, *J. Phys. D: Appl. Phys.* **2001**, *34*, 3224–3228.

51. C.W. Ong, K.F. Chan, C.L. Choy, *Thin Solid Films* **2001**, 388, 217-225.

52. E. Doni, G. P. Parravicini, *Nuovo Cimento* **1969**, 64B, 117.

53. R. Mamy, J. Thomas, G. Jezequel, J.C. Lemonnier, *J. Phys. Lett.* **1981**, 42, 473.

54. E. Pascual, J. L. Andu´jar, S. Gimeno, A. Lousa, A. Bosch, M. El Kasmi, E. Bertran, *Diam. Relat. Mater.* **1996**, 5, 539.

55. O. Stenzel, J. Hahn, M. Röder, A. Ehrlich, S. Prause, F. Richter, *Phys.Status Solidi A* **1996**, 158, 281.

56. H. Curtins, M. Favre, *Amorphous Silicon and Related Materials* (Singapore) **1988**, 329.

57. M.S. Nakhmanson, V.P. Smirnov, *Fiz. Tverd. Tela* (Leningrad) **1971**, 13, 905 (Soviet Phys.-Solid State **1971**, 13, 752 ; **1971**, 13, 3288; **1972**,13, 2763).

58. K. Watanabe, T. Taniguchi, H. Kanda, *Nat. Mater.* **2004**, *3*, 404.

59. K. Watanabe, T. Taniguchi, T. Niiyama, K. Miya, M. Taniguchi, *Nat. Photonics* **2009**, *3*, 591.

[60] B. Arnaud, S. Lebègue , P. Rabiller , M. Alouani, *Phys.Rev. Lett.* **2006**, 96, 026402.

[61] L. Wirtz , A. Marini , M. Gruning , C. Attaccalite , G. Kresse , A. Rubio, *Phys. Rev. Lett.* **2008**, 100 189701.

[62] B. Arnaud, S. Lebègue , P. Rabiller , M. Alouani, *Phys. Rev. Lett.* **2008**, 100, 189702.

[63] L. Wirtz , A. Martini , A. Rubio, *Phys. Rev. Lett.* **2006**, 96, 126104.

[64] C.-H. Park , C. D. Spataru , S. G. Louie, *Phys. Rev. Lett.* **2006**, 96, 126105.

[65] P. Jaffrennou, PhD thesis Ecole Normal Superieur (E.N.S) Cachan (**2008**).

[66] K. Watanabe, T. Taniguchi, *Phys. Rev. B* **2009**, *79*, 193104.

[67] L. Museur, E. Feldbach, A. Kanaev, *Phys. Rev. B* **2008**, *78*, 155204.

[68] T. Taniguchi, K. Watanabe, *J. Cryst. Growth* **2007**, *303*, 525.

[69] K. Watanabe, T. Taniguchi, T. Kuroda, H. Kanda, *Appl. Phys. Lett.* **2006**, *89*, 141902.

[70] K. Watanabe, T. Taniguchi, T. Kuroda, H. Kanda, *Diamond Relat. Mater*. **2006**, *15*, 1891.

[71] L. Museur, G. Brasse, A. Pierret, S. Maine, B. Attal-Tretout, F. Ducastelle, A. Loiseau, J. Barjon, K. Watanabe, T. Taniguchi, A. Kanaev, Phys. Stat. Solidi **2011**, 5, 214.

[72] P. Jaffrennou, J. Barjon, J. S. Lauret, B. Attal-Trétout, F. Ducastelle, A. Loiseau, *J. Appl. Phys.* **2007**, *102*, 116102.

[73] L. Museur, A. Kanaev, *J. Appl.Phys.* **2008**, *103*, 103520.

[74] D. E. Aspnes, *Thin Solid Films* **1982**, 89, 249.

[75] W. Theiss, *Surf. Sci. Reports* **1997**, 29, 91.

76. M. Schubert, B. Rheinländer, E. Franke, H. Neumann, J. Hahn, M. Röder, F. Richter, *Appl. Phys. Lett.* **1997**, 70(14), 1819-1821.

77. T. Takahashi, H. Itoh, M. Kuroda , *J. Cryst. Growth* **1981**, 53, 418.

78. S.L. Rumyantsev, M.E. Levinshtein, A.D. Jackson, S.N. Mohammmad, G.L. Harris, M.G. Spencer, M.S. Shur in *Properties of Advanced Semiconductor Materials GaN, AlN, InN, BN, SiC, SiGe* . Eds. M.E. Levinshtein, S.L. Rumyantsev, M.S. Shur, *John Wiley & Sons*, Inc., New York, **2001**, 67-92.

79. T. Ishii, T. Sato, *J. Cryst. Growth* **1983**, 61, 689.

80. http://www.metricon.com/basic.html

Chap 5 Study of possible applications

The importance of 2D nanomaterials with high porosity and super-repellent behaviors resides in different possible applications such as supports for functional moisture detector and gas storage. The gas storage application is fashionably since we treated seriously the pollution issue as a priority problem of ecosystem.

First steps towards mechanical exfoliation were taken in order to use h-BN nanowalls flakes as a substrate for graphene[14]. This idea is one of great interest for instance to the opto-electronic domains, electric applications (conductivity, mobility) and so on. To go further, first attempt was achieved successfully to isolate completely h-BN layer to their substrate using acid acetic and water.

The role of h-BN as a biosensor material could be deeply exploited by their insulating features (capacitive effect). We will show that the h-BN (NWs) could be used as well as a substrate for DNA attached (e.g. biosensors applications)

In the last part of this chapter, a magneto-transport property of the nanowalls is investigated and a promising result for future applications is reported and discussed.

5.1 Wetting behavior of the h-BN/h-BN nanowalls

5.1.1 Results

The mean contact angle (CA) is measured for different h-BN films with the same thickness, but with different $\%H_2$ as shown in Figure 5- 1. Elliptic fitting is used to determine graphically the contact angle (CA). For this measurement, a 0.4 µl DI water droplet volume was put on the h-BN/h-BN nanowalls surface.

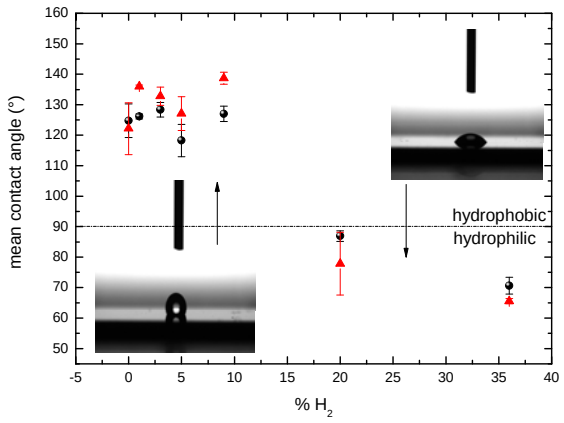

Figure 5- 1: Mean contact angle (CA) versus H_2 % content for 200 nm thin BN films (black sphere) and for 1.5 µm thin BN films (red triangle). Inset: the shape of a DI water droplet on a h-BN/h-BN nanowalls layer is shown in both hydrophobic and hydrophilic conditions.

5.1.2 Discussion

Note that the repellent (hydrophobicity) behavior of the h-BN (NWs) seems to decrease for films deposited with more than 9% H_2 in the Ar /N_2 plasma. It seems that porosity is the main factor (chap 4 Table 4- 8). If a small liquid drop is deposited on a rough surface, in most cases it will spread, engulfing surface asperities (rough projection on an atomic scale). As shown in Figure 5- 2a, this corresponds to the hydrophilic case where the contact liquid has penetrated the spaces between the asperities. Hydrophilic behavior is observed for the h-BN films grown with 20% and 36% H_2 (the smoother granular films), independently of the film thicknesses. Here, the interaction of the liquid with the film surface can lead to low values (<70°) of the contact angle measurement[1-5] and, consequently, substantial forces may be required to initiate drop movement[6]. Less frequently, drops are suspended atop inherently lyophobic asperities[7-12] leaving air (or vapor) between them. This suspension, depicted in Figure 5- 2b, corresponds to the hydrophobic case and was observed with our h-BN films grown with 0% to 9% H_2, again independently of the film thicknesses. This leads to a very poor liquid-solid adhesion and large apparent contact angles (between 140 to 180°) that are characteristic of super-repellent[13] or ultralyophobic surfaces i.e. very rough surfaces.

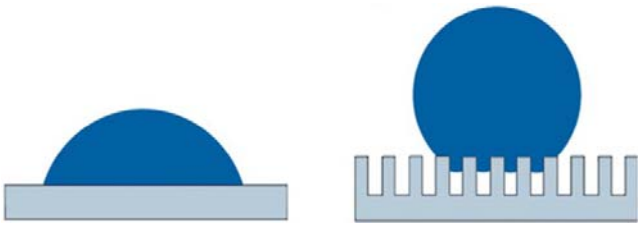

Figure 5- 2: Small sessile drops on rough surfaces. (a) a collapsed drop on rough surface; (b) a suspended drop on an ultralyophobic surface.

5.2 Fabrication and characterization of h-BN flakes

H-BN flakes are defined as pieces of multi-layered h-BN nanowall films. To obtain this result, we tried first successfully to isolate some h-BN nanowalls using a simple but effective mechanical exfoliation technique with scotch tape, similar to the graphene extraction technique[14], followed by a transfer to a SiO_2 (300 nm)/Si substrate. Noteworthy is that the method to obtain some h-BN flakes from h-BN nanowall should be carefully performed in order to prevent extrinsic defects.

5.2.1 Methods

According to Dean et al.[14], h-BN flakes have very exciting application as they can be used as a substrate for graphene. A good candidate for this application could be h-BN nanowalls (5% H_2) deposited on quartz (0001) with 10 µm film thickness, low contamination according to RBS measurements (less than 5% carbon and oxygen) and crystallized in its preferential (002) orientation structure.

The SiO_2/Si substrate has some markers and grooves made by a photolithographic mask to easily locate the h-BN nanowall flakes using optical microscopy. Observed with optical microscopy (Axiovert 40 MAT (ZWEISS)), five h-BN flakes (labeled a to e) were selected, with an area higher than 5 µm² as shown in Figure 5- 3. Note that, for clarity, pictures show only h-BN flakes except in Figure 5- 3e, where flake and marker are represented.

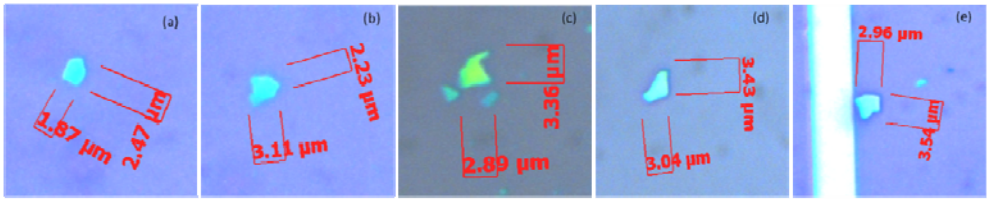

Figure 5- 3: Optical images of representative h-BN flakes exfoliated onto a SiO_2/Si substrate and localized via markers and grooves. These markers and grooves are suppressed from pictures (for clarity) except in (e) with its white band at the left of the h-BNNWs flake.

Those h-BN (NWs) flakes could also be measured with atomic force microscopy (AFM).

5.2.2 AFM characterization

In Figure 5- 4, the thickness of each corresponding h-BN flake was measured (thickness and roughness) using AFM. This technique reveals the flatness from few (142, 53 and 29) monolayers of the h-BN flakes as illustrated in Figure 5- 4 (a, b and c), respectively.

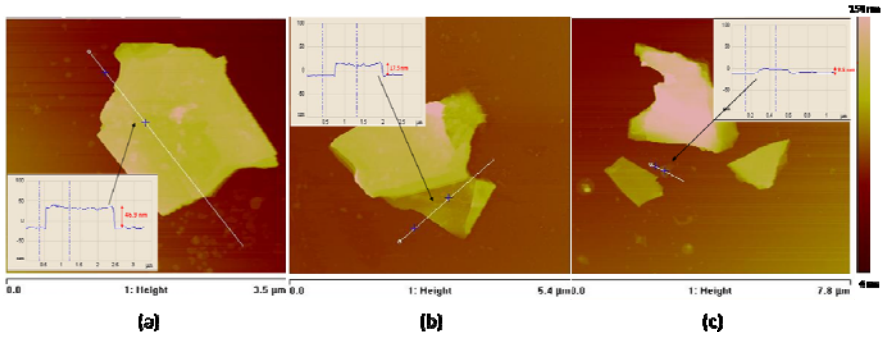

Figure 5- 4: AFM images of representative h-BN flakes exfoliated onto a SiO_2/Si substrate corresponding to the optical images 5.9a (a) 5.9b (b) and 5.9c (c), respectively. Inset: Profile with flake thicknesses of 46.9 nm (a); 17.5 nm (b); 9.5 nm (c).

Among these five large h-BN flakes, two of them (sample d and e) have an interesting layered structure as shown in more detail in Figure 5- 5 and Figure 5- 6, respectively.

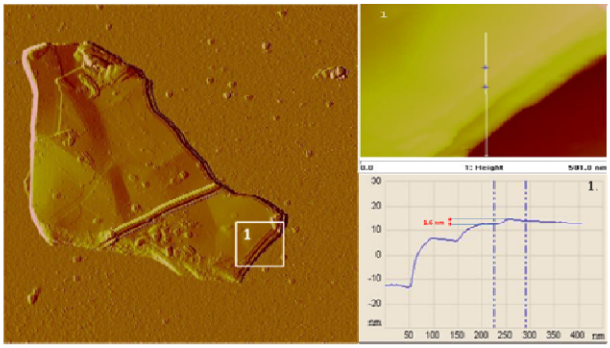

Figure 5- 5: AFM images of a representative h-BN flake (sample d) exfoliated onto a SiO_2/Si substrate. Inset: zoom position 1 with a 1.6 nm layered film (corresponding approx. to 5 h-BN monolayers).

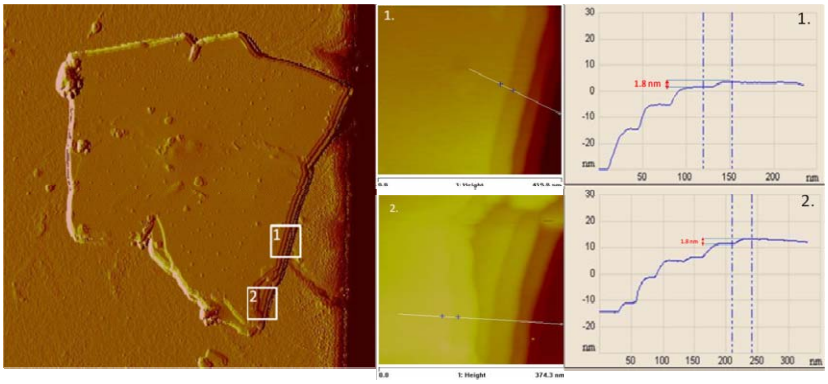

Figure 5- 6: AFM images of a representative h-BN flake (sample e) exfoliated onto a SiO_2/Si substrate. Inset: zoom position 1 and position 2, with 1.8 nm layered film (corresponding to approx. 6 h-BN monolayers).

Each step height was measured from h-BN multi-layers flakes samples (d and e). The least common multiple (LCM) of the 2 smallest steps of samples d and e i.e. experimental value were compared to the theoretical value corresponding to the interlayer distance of the h-BN bulk material (c/2=3.33 Å). As shown in

Figure 5- 7, the idea is to verify if the measured step heights (0.1 nm accuracy) are a multiple of interlayer distance. The layered structures of samples d and e are lying perfectly flat along the basal plane for h-BN bulk material.

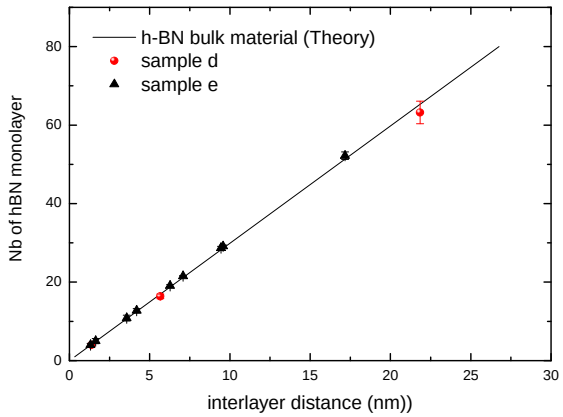

Figure 5- 7: Number of h-BN monolayer vs. interlayer distance (c/2=3.33 Å) (black line), and experimental data from 2 different flakes (black triangle sample e and red sphere sample d)

5.3 h-BN (NWs) as templates for DNA attachment

This work was done in collaboration with the BIOS group from IMO and particularly with Lars Grieten and Prof. dr. Patrick Wagner.

5.3.1 Methods

The surface of the h-BN nanowalls/Si(100) samples (5% H_2) were covered with a pure solution of 10-undecenoic acid and subsequently illuminated in a N_2 glove box for 20h with a 254 nm light source (Philips TUV G4T4 4W lamp). After the UV photo-attachment, the samples were 20 min boiled in acetic acid at 120°C and afterwards thoroughly rinsed in Milli-Q water.

Two types of DNA are coupled to the carboxyl (COOH) groups on the h-BN nanowalls surface. The first is a short 8 base pairs (bp) sequence corresponding to circa 27 Å of length along the DNA strand with an Alexa-488 fluorophore at the 3' terminated and a -NH_2 group at the 5' terminated .

In order to couple 1.2 µg Alexa labeled NH_2 modified DNA to the carboxyl groups, an intermediary reaction is carried out using 50 mg/ml ethyl-3-[3-

dimethylaminopropyl]-carbodiimide (EDC) in a 25 millimoles (mM) MES solution, pH 6, for 2 h at 4°C. By using EDC a nucleophylic substitution occurs that result in a net amide bond between the fatty acid (undecenoic acid) and the DNA strand. Negative-EDC controls i.e. no biological coupling possible have all the components as described above except the presence of the EDC coupling agent.

5.3.2 Results (confocal imaging)

In Figure 5- 8, all images were recorded at 10% of the AOTF transmission (~33 μW at the sample position) to avoid bleaching during the acquisition of the fluorescence. For bleaching, a rectangular region of interest (ROI) was defined to prove the presence of fluorescent attached bio-molecular particles. The bleaching was performed by applying 10 scans of the ROI with the AOTF transmission set to 100%.

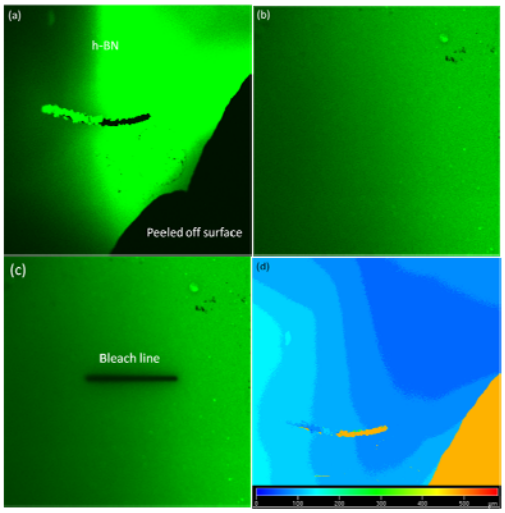

Figure 5- 8: Confocal imaging of different areas of the DNA attached on h-BN, 512x512x1 μm^3 (a) ; 225 x 225μm^2 (b) with a bleach line (c); surface profile peeled off layer (d). All images were performed with confocal microscope (objective x10) and data acquisition at 25.6 μs integration time.

5.4 Magneto transport properties of h-BN (NWs)

5.4.1 Results and discussion (SQUID characterization)

Dean et al.[14] have observed that mobility (electrons and holes) in graphene–on–h-BN resulting from a reduction of charged impurities enhance by a factor of 3 to 7 times relative to graphene–on–SiO_2. From the encouraging result, h-BN could be interesting substrates to substitute to SiO_2 substrates. In order to explore the potential of h-BN, their magnetic properties were investigated.

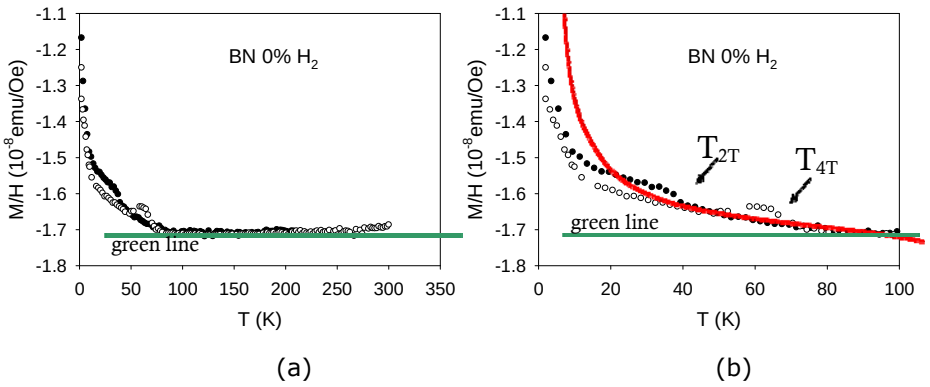

Figure 5- 9: Measurements of the magnetization on h-BN/Si grown with 0%H_2 between 0-300K (a) and between 0-100K (b).

As shown in Figure 5- 9, a large diamagnetic contribution of the Si substrate by means of its negative M/H ratio (susceptibility) is marked by a green line, which is temperature independent.

At temperatures T_{2T} ~30 K, T_{4T} ~ 60 K (see in Figure 5- 9b), we can see a dependence relative to the magnetic-field, which is tentatively attributed to some probable anomalies due to possible disordering of the h-BN structure or structural defects. Usually, contamination by air could be seen at around 60 K, but it is not field-dependent.

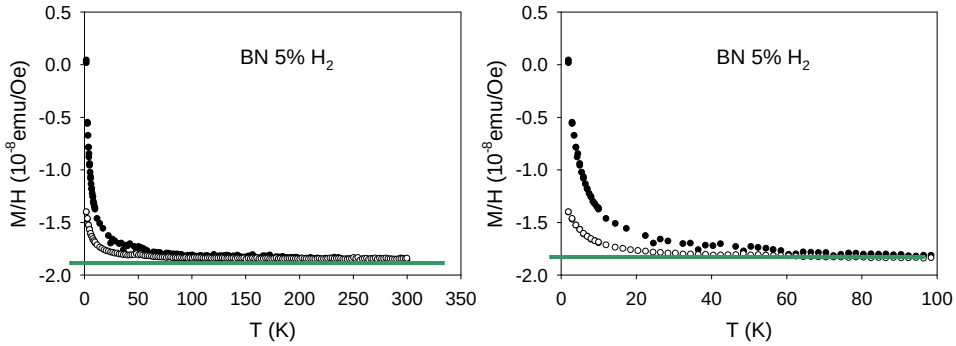

Figure 5- 10: Measurements of the magnetization on h-BN/Si grown with 5%H_2 between 0-300K (a) and between 0-100K (b).

Similar to the sample grown with 0% H_2, a large diamagnetic contribution of the Si substrate is marked with a green line in Figure 5- 10.

The field-dependency at low-temperature reveals a higher paramagnetic-like behavior of the 5% H_2 h-BN film relative to the granular h-BN structure (0% H_2). Below 2 K, saturation or maximum could occur. This is probably due to onsets of ordering or electron correlations.

The influence of the Si substrate is also checked with a separate an extra SQUID measurement (Figure 5- 11).

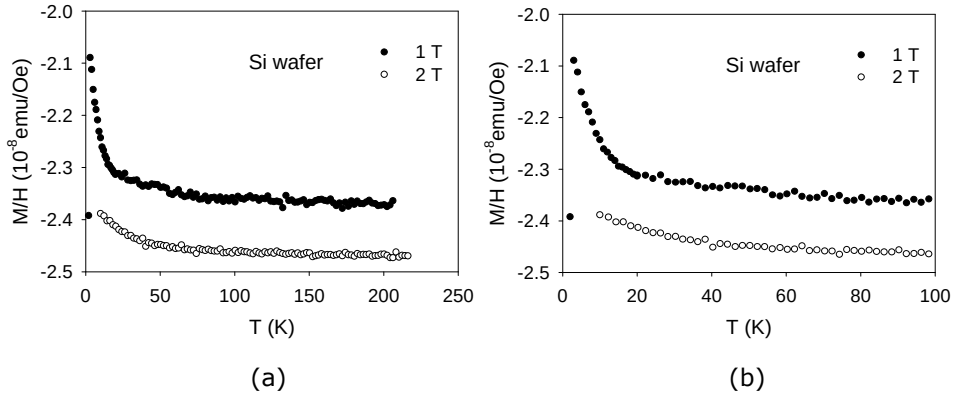

Figure 5- 11: Measurements of the magnetization on Si (100) between 0-300K (a) and between 0-100K (b).

In order to have an overview of measurement, a comparison of all three samples i.e. h-BN/Si grown with 0% H_2 and 5%H_2 and Si substrate with corrected to mass and centering offset were summarized in Figure 5- 12 .

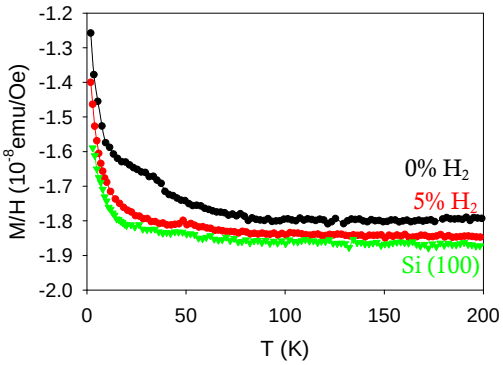

Figure 5- 12: Measurements of the magnetization of all three samples

5.5 Conclusions

In the framework of the possible applications, the porosity and the super-repellent properties of h-BN films were investigated by different series of measurements.

We found a linear relationship between the refractive index and the large porosity rate (or the lower filling ratio) allowing us to measure for instance the refractive index of an unknown h-BN film compositions and deducing directly its own porosity rate or filling ratio.

The super-repellent characteristic is revealed to be dependent on the roughness of the surface and not of the structures itself (granular or nanowall). The method to obtain some h-BN flakes from h-BN nanowall should be carefully performed in order to prevent extrinsic defects coming from Scotch tape for instance. This might be harmful for our h-BN films.

However, it is the first time that h-BN nanowalls were used as DNA attachment substrate devices confirmed by the presence of fluorescent attached bio-molecular particle during the bleaching. First series of measurement are really promising for further investigations.

Concerning the magnetic features of h-BN (NWs), the magnetoconductivity and the magnetoresistance should be more investigated as future possible topics of study.

5.6 References

1. X. J. Feng, L. Jiang, *Adv. Mater.* **2006**, 18, 3063–3078.
2. M. Tanaguchi , G. Belfort, *Langmuir* **2001**, 17,6465.
3. D. Oner, T. M. McCarthy, *Langmuir* **2000**, 16, 7777 .
4. J. D. Miller, S. Veeramasuneni, J. Drelich, M. R. Yalamanchili, G. Yamauchi, *Polym. Eng. Sci.* **1996**, 36, 1849.
5. C. W. Extrand , A. N. Gent, *J. Colloid* ***Interface*** *Sci.* **1990**, 138, 431 .
6. G. MacDougall , C. Okrent, *Proc. Roy.* Soc. *(London)* **1942**, 180A, 151 .
7. C.W.Extrand in Contact Angle, Wettability and Adhesion, K.L. Mittal Ed. **2006**, 4, 295-305 .
8. R. H. Dettre and R. E. Johnson Jr., in Contact Angle, Wettability and Adhesion, Adv. Chem. Ser. **1964**, 43, 136.
9. A. Hozumi, 0. Takai, *Thin Solid Films* **1997**, 303, 222 1.
10. K. Tadanaga, N. Katata, T. Minami, *J. Am. Ceram. Soc.* **1997**, 80, 1040.
11. J. Bico, C. Marzolin , D. Qukre, *Europhys. Lett.* **1999**, 47, 220.
12. Z. Yoshimitsu, A. Nakajima, T. Watanabe, K. Hashimoto, *Langmuir* **2002**, 18, 5818 .
13. J. Yu, L. Qin, Y. Hao, S. Kuang, X. Bai, Y-M. Chong, W. Zhang, E. Wang, *ACS Nano.* **2010**, 4, 1.
14. C. R. Dean, A. F. Young, I. Meric, C. Lee, L. Wang, S. Sorgenfrei, K.Watanabe, T. Taniguchi, P. Kim, K. L. Shepard ,Hone, *Nature Mater***. 2010**, 5, 722-726.

Chap 6 General Conclusion

Some parameters which control the mechanism of h-BN growth are the same for PVD or CVD techniques. In fact, they are both dominated by ionic bombardment and substrate temperature. Into the mechanism of h-BN growth, we should add some secondary chemical effects coming from the stoichiometry controlled by N_2 gas flow, impurities (carbon and oxygen) and the introduction of hydrogen in the Ar/N_2 plasma mixture. These contributions participate actively to the h-BN phase formation and, explaining the quality of the film formation.

In this work, we have synthesized porous films of hexagonal boron nitride by using the easy to handle, scalable and cost effective reactive radio-frequency magnetron sputtering technique. Several films deposited on Si (100) are characterized in a qualitative way with EDS to investigate C and O contaminations, and also, in a quantitative way with RBS to confirm the structure and stoichiometry of the h-BN films. The addition of H_2 as a reactive gas in the N_2/Ar mixture during RF sputtering leads to h-BN nanowall layers with a reduced amount of oxygen and carbon impurities, independent of the substrate material. While fluorine is ruled out as a crucial constituent in the formation of carbon nanowalls, the role of hydrogen is effective and primordial for the well-controlled growth of these 2D/3D structures. An optimum of 5% H_2 leads to stoichiometric h-BN nanowalls independently of the substrate temperature. The evidence of the hexagonal phase and polycrystallinity of the BN layers was pointed out by FTIR and cross-sectional TEM images. Indeed, typical h-BN platelets have a thickness below 50 nm, and their (002) planes tilt over maximum 20° relatively to the normal direction of the used substrate material. But more experiments should be done to confirm these results.

A rotative homemade substrate holder adapted to the FTIR measurement was built in order to decouple the different infrared active modes of the samples. The infrared measurements at oblique incidence were modeled by an effective dielectric function to estimate the orientation of the c-axis. Indeed, this well-known h-BN bulk material model was applied on stable, FTIR and XRD spectra, and well crystallized films in agreement with the Raman spectra.

Polarized infrared reflectance spectra (PIRR) were taken for the first time on h-BN nanowalls. The occurrence of the Berreman resonance or the 2 phonon peaks in polarized IRS data acquired from thin h-BN nanowalls films, reveal their own optical fingerprint.

Further, the mass density, roughness and stress are additional results to add to the physical properties of h-BN.

We note that, the band gap deduced from UV-Vis spectra is exceeding 5.6 eV (indirect) for films grown with 5% H_2. These films are deposited on fused silica substrate heated at 400°C and these thicknesses are lower than 200 nm. These UV-Vis spectra give an estimation of the band gap that is confirmed later by the cathodoluminescence spectra.

The luminescent properties of h-BN nanowalls are dominated by a broad impurity band near 4 eV, which is also observed in the bulk h-BN, and is possibly related to the C and O impurities. The recombination of excitons from h-BN nanowalls is consistent with the features of the bulk h-BN in the presence of structural defects, grain boundaries or impurities.

Making use of nano CL, h-BN excitonic luminescence at 5.61 eV (221 nm) and defect band luminescence related to impurities at ~ 3.9 eV (318 nm) are observed. Even if the nature of these excitonic recombinations in the h-BN nanowalls is not completely clear yet, it could be due to the excitons trapped at structural defects on the h-BN film.

The evolution of density (refractive indices) when the thickness of the films increases, was explained by the structural properties of the h-BN films, i.e. their roughness.

Publications

Journals

B. BenMoussa, A. Soltani, J. Charrier, J. D'Haen, V. Mortet, M. D'Olieslaeger, H.-G. Boyen, K. Haenen, "Optical properties of hexagonal boron nitride nanowall thin films", to be submitted (2012).

B. BenMoussa, J. D'Haen, J. Barjon, A. Soltani, V. Mortet, M. D'Olieslaeger, H.-G. Boyen, K. Haenen, "Hexagonal boron nitride nanowalls: synthesis, 2D/3D morphology, and spectroscopic analysis", in revision for Journal of Physics D-Applied Physics (2011).

A. BenMoussa, A. Soltani, U. Schühle, K. Haenen, Y.M. Chong, W.J. Zhang, R. Dahal, J.Y. Lin, H.X. Jiang, H.A. Barkad, B. BenMoussa, D. Bolsee, C. Hermans, U. Kroth, C. Laubis, V. Mortet, J.C. De Jaeger, B. Giordanengo, M. Richter, F. Scholze, J.F. Hochedez, "Recent developments of wide-bandgap semiconductor based UV sensors", Diamond and Related Materials **18**/5-8 (2009), 860-864.

Proceedings

B. BenMoussa, J. D'Haen, C. Borschel, M. Saitner, A. Soltani, V. Mortet, C. Ronning, M. D'Olieslaeger, H.-G. Boyen, K. Haenen, "Hexagonal boron nitride nanowalls synthesised by unbalanced RF magnetron sputtering", MRS Online Proceedings Library **1307** (2011), MRSF10-1307-CC6-9, DOI: 10.1557/opl.2011.505.

Orals

B. BenMoussa, C. Borschel, J. Barjon, J. D'Haen, A. Soltani, V. Mortet, C. Ronning, M. D'Olieslaeger, H.-G. Boyen, K. Haenen, "Hexagonal boron nitride nanowalls: physical vapour deposition, structural and opto-electronic properties", 5th International Conference on New Diamond and Nano Carbons (NDNC2011), Kunibiki Messe, Matsue City, Japan, May 16-20, 2011.

B. BenMoussa, C. Borschel, J. D'Haen, J. Barjon, M. Saitner, A. Soltani, V. Mortet, C. Ronning, M. D'Olieslaeger, H.-G. Boyen, K. Haenen, "Influence of hydrogen gas on the synthesis and properties of hexagonal boron nitride nanowalls prepared by unbalanced RF magnetron sputtering", MRS 2011 Spring Meeting, Symposium S: Plasma-Assisted Materials Processing and Synthesis,

Moscone West & San Francisco Marriott, San Francisco, CA, USA, April 25-29, 2011.

B. BenMoussa, J. D'Haen, C. Borschel, M. Saitner, A. Soltani, V. Mortet, C. Ronning,
M. D'Olieslaeger, H.-G. Boyen, K. Haenen, "Hexagonal boron nitride nanowalls synthesised by unbalanced RF magnetron sputtering", MRS 2010 Fall Meeting, Symposium CC: Boron and Boron Compounds--From Fundamentals to Applications, Hynes Convention Center & Sheraton Boston Hotel, Boston, MA, USA, November 29-December 3, 2010.

Posters

B. BenMoussa, J. D'Haen, C. Borschel, A. Soltani, V. Mortet, C. Ronning, M. D'Olieslaeger, H.G. Boyen, K. Haenen, "Synthesis of hexagonal boron nitride by physical vapour deposition process", 21st European Conference on Diamond, Diamond-like Materials, Carbon Nanotubes, and Nitrides, Kempinski Hotel Corvinus Budapest, Budapest, Hungary, September 5-9, 2010.

B. BenMoussa, J. D'Haen, C. Borschel, M. Saitner, A. Soltani, V. Mortet, C. Ronning, M. D'Olieslaeger, H.-G. Boyen, K. Haenen, "Unbalanced RF magnetron sputtering of thin hexagonal boron nitride films", 4th International Conference on New Diamond and Nano Carbons (NDNC2010), Garden Hotel, Suzhou, China, May 16-20, 2010.

B. BenMoussa, J. D'Haen, C. Borschel, L. Goris, A. Soltani, V. Mortet, C. Ronning, M. D'Olieslaeger, H.G. Boyen, K. Haenen, "Growth and characterization of hexagonal boron nitride by unbalanced RF magnetron sputtering", Hasselt Diamond Workshop 2010 – SBDD XV, cultuurcentrum Hasselt, Hasselt, Belgium, February 22-24, 2010.